FAA-74-27
REPORT NO. FAA-RD-74-215

IMPACT OF SATELLITE AERONAUTICAL CHANNEL ON MODEM SPECIFICATIONS

Phase II: Oceanic Multipath Measurements and Modem Concepts

Phillip A. Bello
David Chase
Joseph K. DeRosa
Lih-Jyh Weng
Martin G. Bello

JANUARY 1975

FINAL REPORT

Prepared for
U.S. DEPARTMENT OF TRANSPORTATION
FEDERAL AVIATION ADMINISTRATION
Systems Research and Development Service
Washington DC 20591

Technical Report Documentation Page

1. Report No.	2. Government Accession No.	3. Recipient's Catalog No.
FAA-RD-74-215		

4. Title and Subtitle	5. Report Date
IMPACT OF SATELLITE AERONAUTICAL CHANNEL ON MODEM SPECIFICATIONS. Phase II: Oceanic Multipath Measurements and Modem Concepts	January 1975
	6. Performing Organization Code
7. Author(s) Phillip A. Bello, David Chase, Joseph DeRosa, Lih-Jyh Weng, Martin G. Bello	8. Performing Organization Report No. DOT-TSC-FAA-74-27
9. Performing Organization Name and Address CNR, Inc.* 20 Wells Avenue Newton MA 02159	10. Work Unit No. (TRAIS) FA511/F5110
	11. Contract or Grant No. DOT-TSC-516-2
12. Sponsoring Agency Name and Address U.S. Department of Transportation Federal Aviation Administration Systems Research and Development Service Washington DC 20591	13. Type of Report and Period Covered Final Report - Phase II March 1973 - March 1974
	14. Sponsoring Agency Code

15. Supplementary Notes

*Under Contract to: U.S. Department of Transportation
Transportation Systems Center
Kendall Square
Cambridge MA 02142

16. Abstract

This report completes the analysis initiated in the Phase I report of the effects of oceanic multipath on ranging and data modems for satellite air traffic control systems. The interaction between multipath antenna and apparent measured multipath is determined using a "vector Kirchoff" model of ocean scattering. Procedures for antenna design, sea state sensing, and multipath measurements are detailed, and tone ranging performance is computed for various antenna designs. Consideration is given to the problem of tone probing on a 50 KHz hard limiting AEROSAT channel while data transmission is taking place. The problem of how much measurement time is needed to achieve a reliable measurement of error probability in data transmission over the AEROSAT channel is addressed. It is also shown that with the proper integration of coding and modulation techniques, it is possible to construct a robust signaling scheme which is insensitive to the multipath and which can improve performance when operating in the region of low direct path signal-to-noise ratios.

17. Key Words	18. Distribution Statement
Aircraft-Satellite Channel Characterization, Oceanic Multipath, Multipath Antenna, Sea State Measurement, Tone Probing, Error Probability Measures, Coding and Modulation Techniques	DOCUMENT IS AVAILABLE TO THE PUBLIC THROUGH THE NATIONAL TECHNICAL INFORMATION SERVICE, SPRINGFIELD, VIRGINIA 22161

19. Security Classif. (of this report)	20. Security Classif. (of this page)	21. No. of Pages	22. Price
Unclassified	Unclassified	202	

Form DOT F 1700.7 (8-72) Reproduction of completed page authorized

PREFACE

The work documented in this volume represents the second phase of a three-phase advanced technology task undertaken by the Electromagnetics Division, Communications Branch, of the Technology Directorate at the Transportation Systems Center (TSC) in support of the Department of Transportation's program to investigate satellite-based air traffic control systems. The overall objective of the program is to determine the impact of the aeronautical channel characteristics on the type of ranging and data modems best suited for use on AEROSAT.

The present volume completes the analysis initiated in the Phase I report on the effects of oceanic multipath on ranging and data modems for satellite air traffic control systems. The utilization of channel measurements in modem development is presented in detail in the Phase I report.

The Phase III report is a preliminary CONUS satellite wide-band test plan.

Technical association with Louis A. Frasco of TSC is hereby acknowledged.

Table of Contents

TABLE OF CONTENTS (Continued)

LIST OF ILLUSTRATIONS

LIST OF ILLUSTRATIONS (Continued)

LIST OF ILLUSTRATIONS (Continued)

LIST OF ILLUSTRATIONS (Continued)

LIST OF TABLES

1. INTRODUCTION

This report is Phase II of an effort which supports the Department of Transportation's program to provide a satellite-based air traffic control system. It is a sequel to the Phase I study documented in Report No. DOT-TSC-516-1. The overall objective of the program is to determine the impact of the aeronautical channel characteristics on the type of ranging and data modems best suited for use on AEROSAT. Existing channel models and measurements are used where possible and channel measurement procedures proposed where needed. The utilization of channel measurements in modem development is presented in detail in the Phase I report, and an outline is repeated here in Fig. 1.1 for convenience. The salient features of this approach are listed below:

1. Propagation and system function modeling
2. Propagation and system function measurements
3. Software and hardware modem development
4. Synthetic and playback channel simulation
5. Modem evaluation.

The content of the Phase I report can be summarized as follows:

1. General approach to modem development with the aid of channel measurements
2. Measurement comparisons and recommendations for system and signal design
3. Steepest-descent model for multipath and Doppler spread characteristics
4. Performance of tone ranging modems
5. Performance of PN ranging modems
6. Performance of FSK and DPSK modems
7. Channel probing for analysis and playback simulation

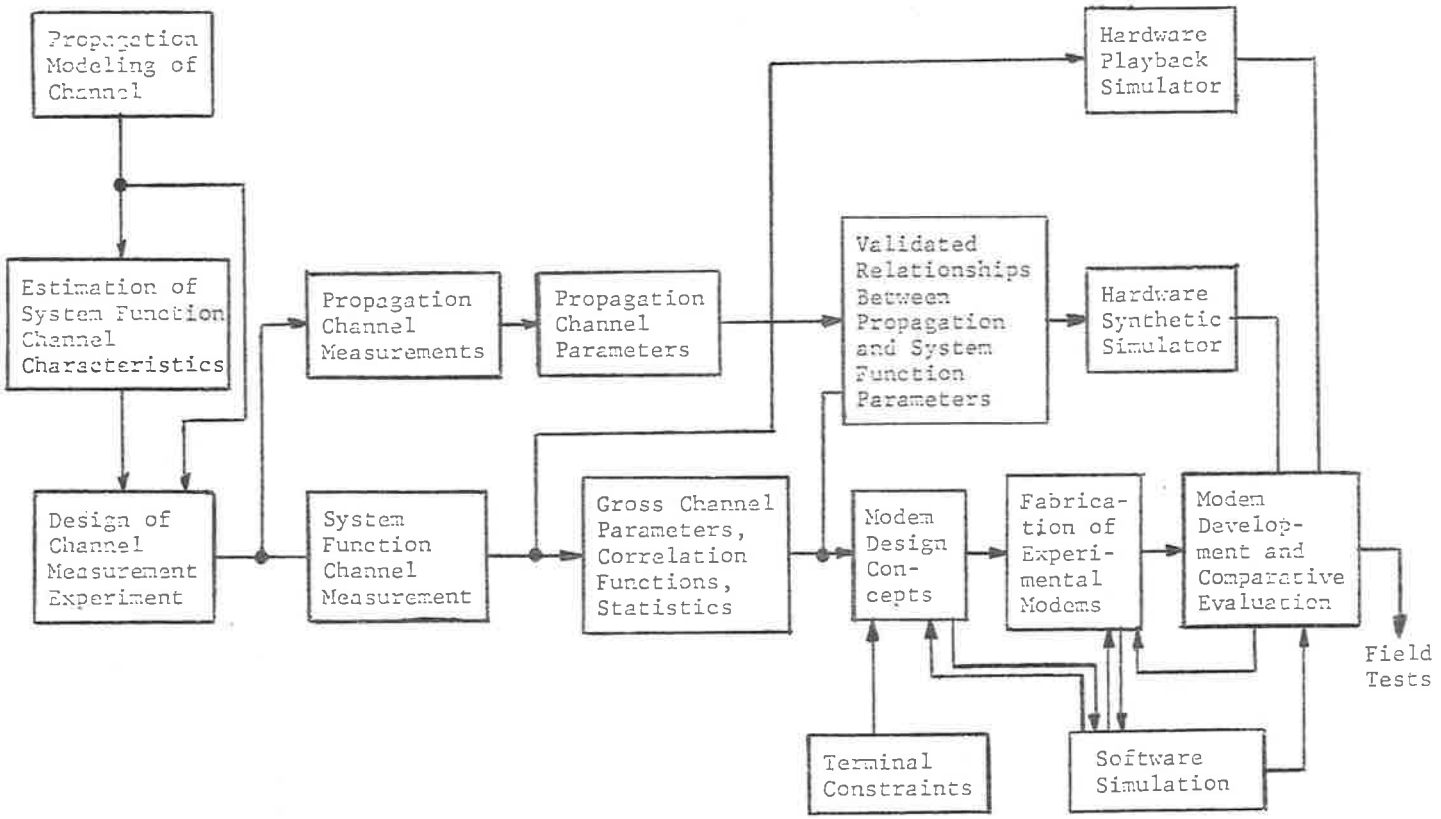

Figure 1.1 Utilization of Channel Measurements in Modem Development

The Phase II report completes the pre-flight-test portion of the overall modem development by presenting details of multipath measurements and modem concepts. The content of the Phase II report can be summarized as follows:

1. Development of "vector Kirchoff" model for multipath and Doppler spread characteristics
2. Calculations of multipath and Doppler spectra
3. Specification of sea-state measurements
4. Design of the multipath antenna
5. Performance of tone ranging modem using multipath antenna
6. Tone probing during data transmission
7. Reliability of error probability measurements
8. Combined coding and modulation techniques.

More specific details of the results of the work done in Phase II are presented below on a section-by-section basis.

Section 2 determines the interaction between multipath antenna characteristics and apparent measured oceanic multipath. Among the topics considered are guidelines for the proper design of multipath antennas, sea state measurement recommendations, oceanic flight scenarios, sensitivity of channel parameter measurements to variations in flight parameters, detailed multipath calculations, and inferred tone ranging performance for different multipath antennas. With the exception of the sensitivity analysis, all of the calculations are performed using the "vector Kirchoff" model of ocean scattering, which is more sophisticated than the "steepest-descent" model used in Phase I. This provides a more realistic oceanic multipath model on which modem development and performance evaluation can be based.

Section 3 considers the problem of tone probing in a 50 Kc hard limiting Aerosat channel while data transmission is taking place. It is shown that the tones may be used to sample the time-variant transfer function of the channel in the vicinity of the data signal. The analysis determines the effect of the selection of frequency locations and relative amplitudes of the tones and data signal on signal suppression and signal/intermodulation power ratios. The data signals considered are 1200 bits/sec FSK and/or PSK.

Section 4 addresses the problem of how much measurement time is needed to achieve a reliable measurement of error probability in data transmission over the Aerosat channel. It is found that the variance of the error rate estimate is increased only a small amount percentage-wise over that computed on the basis of independent bit errors.

Section 5 addresses the problem of transmitting digital data reliably over the Aerosat channel. By proper integration of coding and modulation techniques it is shown that it is quite possible to achieve a robust signaling technique which is fairly insensitive to the channel's surface scatter parameters, such as scatter path energy and Doppler spreads. These results illustrate that the scatter energy need not limit the effectiveness of transmitting digital data and, in fact, can improve the performance when operating in the region of low direct path signal-to-noise ratios.

The flight test measurement program (scheduled to begin in September, 1974) will provide the data necessary to complete the modem development as specified in Fig. 1.1. The measured channel parameters together with the resulting (playback and synthetic) channel simulators can then be used to evaluate the performance of the candidate experimental modems presented in this study as well as existing modems and future designs. In addition, the measurement program will result in a validated oceanic multipath model.

2. INTERACTION BETWEEN ANTENNA CHARACTERISTICS AND OCEANIC MULTIPATH

2.1 SUMMARY AND RECOMMENDATIONS

Section 2 determines channel correlation functions and evaluates side-tone ranging performance in terms of the geometry of the satellite-aircraft link, the scattering properties of the surface, and the characteristics of various aircraft antennas. Specifically, the delay power spectral density (psd), frequency correlation function, Doppler psd and delay-Doppler scattering function are expressed in terms of the scattering cross-section of the ocean surface and the (power) gain pattern of the aircraft antenna. The cross-section is computed using a vector Kirchoff theory over the spherical earth, and the several antennas considered were an omni-directional, a Boeing (ATS-5) multipath antenna, and ideal antennas of various beamwidths.

Numerical evaluations of the delay psd, the frequency correlation function, side-tone ranging performance, and the Doppler psd have been made in this study. The calculations were carried out for an aircraft at a 10 km (32,808 ft.) altitude with specular point grazing angles of 5^{o}, 10^{o}, 20^{o}, and 30^{o}.

It is shown that over the range of grazing angles from 10^{o} to 30^{o}, at an altitude of 10 km the Boeing (ATS-5) multipath antenna attenuates the multipath power by more than 4 dB which in turn yields an apparent ranging improvement of greater than 27%. For an ideal antenna with a gain of unity inside and zero outside the illuminating beam, the multipath loss is computed as a function of elevation and azimuth angle beamwidths. The results are summarized in Table 2-1. It should be noted that the multipath power loss was calculated for the indicated azimuth beamwidths when the elevation beamwidth was 180^{o} and was calculated for the indicated elevation beamwidths when the azimuth illumination included delays up to the indicated cut-off delay contour. Since

Table 2-1

A SUMMARY OF MULTIPATH LOSS FOR VARIOUS BEAMWIDTHS AND BEAM CENTER POSITIONS

Multipath Loss Relative to (Omni) dB	Grazing Angle at Which Antenna is to be Used Degrees	Cut-Off Delay μsec	Elevation Angle of Beam Center Degrees	Elevation Beamwidth Degrees	Azimuth Beamwidth Degrees
0.5	10	10.3	117	48	22
	20	11.4	126	60	30
	30	12.5	134	69	40
	10, 20, & 30	12.5	130	75	40
1.0	10	7.5	113	38	16
	20	8.0	126	50	22.5
	30	8.8	132	60	30
	10, 20, & 30	8.8	127	68	30
1.5	10	6.1	110	34	12
	20	6.4	120	44	18.5
	30	6.9	129	53	22.5
	10, 20, & 30	6.9	125	63	22.5

Aircraft altitude = 10 km

Antenna polarization = circular (opposite sense from direct path).

operational candidate antennas will not have the "ideal" characteristics used in generating Table 2-1, beamwidths presented here should be used only to indicate approximate antenna design goals.

As an illustration of the design procedure, the approximate azimuth beamwidth is obtained from Table 2-1, where for example, it is shown that for a 1 dB multipath loss a 30^{o} azimuth beamwidth is required.* Then the elevation angle of the beam center may either be stepped to accommodate the various grazing angles or may be fixed with a larger beamwidth to allow for proper illumination at each grazing angle. For a 1 dB multipath loss, Table 2-1 indicates that the antenna may have an elevation angle beamwidth of 60^{o}* with stepped beam centers at 113^{o}, 126^{o}, and 132^{o} or alternatively the antenna may be fixed at a 127^{o} position with a 68^{o} elevation beamwidth. Various other design possibilities may be determined from Table 2-1 and Section 2.5.1.3. Operational antennas which approximate these design goals can then be evaluated using the analysis developed in this report.

Based on the results of this section, the following recommendations are made pertaining to multipath antennas for oceanic flights:

1) Multipath antennas should be designed with beamwidths and beam center positions which illuminate the region of significant multipath as defined in Table 2-1. (See Section 2.5.1.3.)
2) There should be a "forward-looking" antenna with azimuthal symmetry. Since the two surface points which contribute to the power density $S(\xi,\nu)$ at a given delay-Doppler point have the same scattering cross section σ for "in-plane" flight paths, then by using the forward-looking antenna, σ can be recovered from $S(\xi,\nu)$. This provides a direct verification of the scattering model.
3) The "side-looking" (ATS-5) multipath antenna can be used on cross-plane flights. Accurate knowledge of the antenna gain pattern can be used to correct the distortion in the multipath profiles caused by the antenna.

*Since it is not practical to have the beamwidth change as the grazing angle changes, the largest value of beamwidth becomes the design goal.

Recommendations for oceanic flight scenarios are as follows:

1) Flights should be made at low grazing angles (e.g., 5^{o}, 10^{o}, 20^{o}, 30^{o}). Operational ATC antennas which are directed upward aboard the aircraft should provide sufficient multipath discrimination at higher grazing angles.
2) In-plane flights should be made to provide a direct measure of scattering cross section as well as delay and Doppler spectra.
3) Cross-plane flights can be made using the existing (ATS-5) multipath antenna. As previously stated, distortion introduced into the tails of the resulting spectra can be accounted for by accurate knowledge of the antenna pattern and by the results of in-plane flights.
4) If there is sufficient flight time, it would be useful to verify that there is negligible scatter outside the active scattering region by directing the antenna away from the specular point (e.g., observe back-scattered and side-scattered return).
5) It has been noted that data will be taken using an (upward-directed) operational antenna to assess multipath effects in a given realistic ATC situation. This will of course be useful information, but since the object of the measurement program is to characterize the multipath for any future operational ATC situation, the majority of the available test time should be devoted to (1) - (3) above.

It is also recommended in Section 2.3 that the following methods be used to determine the sea state descriptors necessary for the verification of the scattering model:

1) NRL sea photo analysis
2) Spar buoy tended by local ship
3) Local anemometer measurements
4) Hindcast data
5) Local visual observations (photographed).

A first-order sensitivity analysis relating accuracy of recorded flight parameters (e.g., altitude, heading, speed, etc.) to accuracy of multipath measurements is provided in Section 2.4.

2.2 PROPAGATION MODELING

The propagation of signals between satellite and aircraft via the direct and scatter paths is affected by the satellite-aircraft geometry, the spatial weighting provided by the antennas, and the scattering properties of the ocean surface. The link geometry induces delay and Doppler contours upon the ocean surface, which constitute a receiver coordinate system in which the signal power is processed. It is important to understand that in addition to the antenna weighting and scattering properties of the surface, the relative sizes of delay-Doppler intervals on the surface (manifested by the Jacobian of the coordinate transformation) also determine the delay-Doppler power densities in the receiver.

2.2.1 Geometric Considerations

The geometric relations on the satellite-aircraft link have been previously derived by DeRosa and are summarized here in Fig. 2.1 and Table 2-1. The value of delay ξ at each point along the surface is given by

$$\xi = \frac{r_0}{c} (R_1+R_2) \tag{2.1}$$

where r_0 is the earth's radius, c is the speed of propagation, and R_1 and R_2 are the normalized ranges from satellite S to scattering point P and from P to the aircraft A (see Table 2-2 for evaluation). Assuming level flight, the value of Doppler frequency ν at each point along the surface is given by [2.1]

$$\nu = \frac{f}{c} (1+H_1)[(\cos \theta_A \sin \theta \sin \varphi - \sin \theta_A \cos \theta)v_\theta^A - \sin \theta \cos \varphi \, v_\varphi^A]/R_2 \tag{2.2}$$

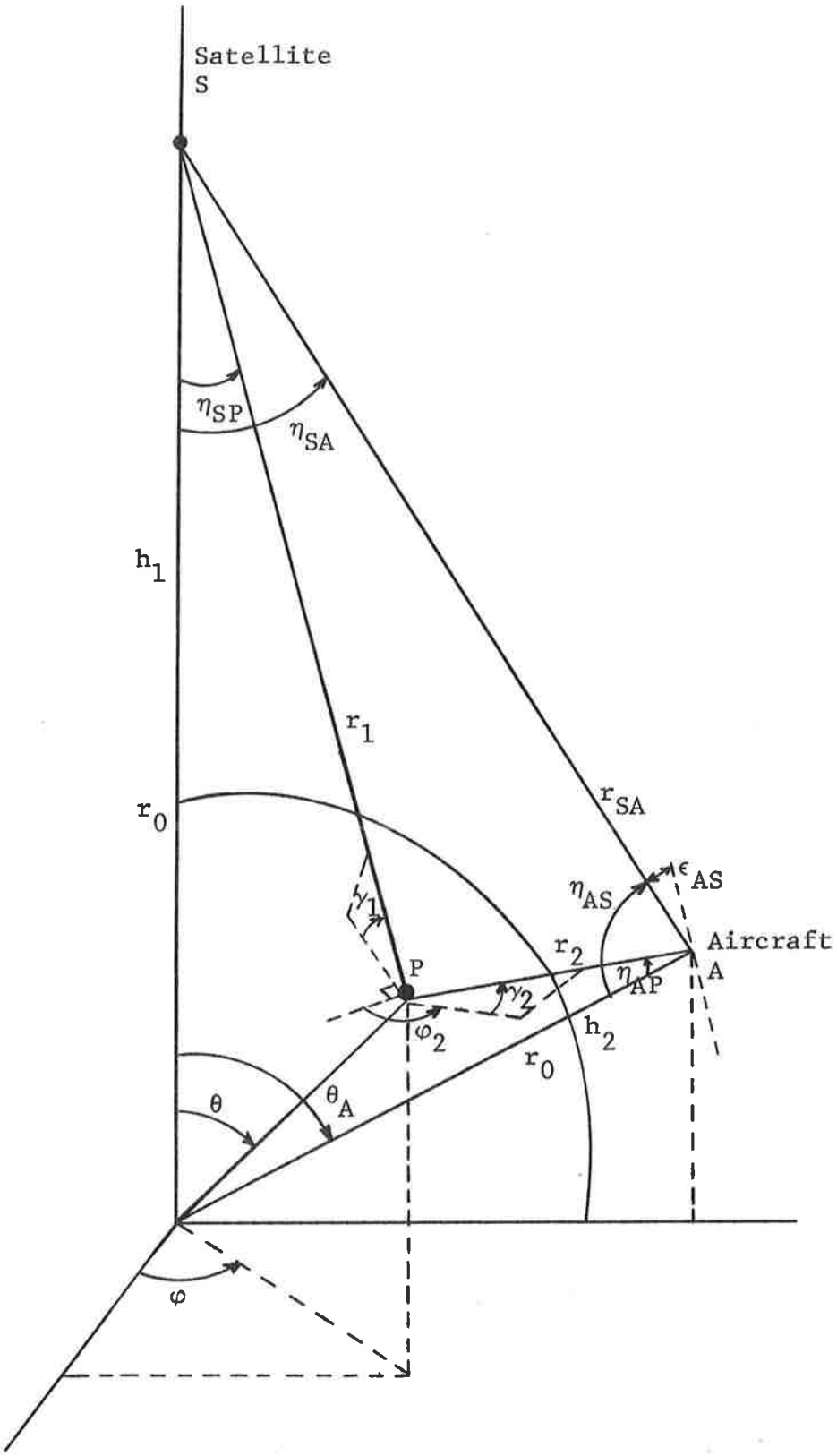

Figure 2.1 Satellite-Aircraft Geometry

Table 2-2

SUMMARY OF GEOMETRIC RELATIONS

Symbol	Definition	Relation
S, P, A	Satellite, Scattering Point, Aircraft	—
λ_a^S λ_0^S λ_a^A λ_0^A	Latitude, longitude of S, A	—
θ, φ	Angular coordinates of P	—
θ_A	Central angle S to A	$\cos \theta_A = \cos \lambda_a^S \cos \lambda_a^A \cos (\lambda_0^S - \lambda_0^A) + \sin \lambda_a^S \sin \lambda_a^A$
r_1	Slant range S to P	$R_1 = \sqrt{1 + P_1^2 - 2P_1 \cos \theta}$
r_2	Slant range P to A	$R_2 = \sqrt{1 + P_2^2 - 2P_2 (\sin \theta_A \sin\theta \sin\varphi + \cos \theta_A \cos \theta)}$
r_{SA}	Slant range S to A	$R_{SA} = \sqrt{P_1^2 + P_2^2 - 2P_1P_2 \cos \theta_A}$
γ_1	Elevation angle of S from P	$\sin \gamma_1 = [P_1 \cos \theta - 1]/R_1$
γ_2	Elevation angle of A from P	$\sin \gamma_2 = [P_2(\sin \theta_A \sin\theta \sin\varphi + \cos \theta_A \cos \theta) - 1]/R_2$
φ_2	Azimuth angle of A from P	$\cos \varphi_2 = -P_2 \sin \theta_A \cos \varphi/R_2 \cos \gamma_2$
η_{SP}	Nadir angle of P at S	$\cos \eta_{SP} = [\cos \theta - P_1]/R_1$
η_{SA}	Nadir angle of A at S	$\cos \eta_{SA} = [P_1 - P_2 \cos \theta_A]/R_{SA}$
η_{AP}	Nadir angle of P at A	$\cos \eta_{AP} = [P_2 - (\sin \theta_A \sin\theta \sin\varphi + \cos \theta_A \cos \theta)]/R_2$
η_{AS}	Nadir angle of S at A	$\cos \eta_{AS} = [P_2 - P_1 \cos \theta_A]/R_{SA}$
ϵ_{AS}	Elevation angle of S at A	$\epsilon_{AS} = \pi/2 - \eta_{AS}$

Note: Normalizations: $R_1 = r_1/r_0$, $R_2 = r_2/r_0$, $R_{SA} = r_{SA}/r_0$, $H_1 = h_1/r_0$, $H_2 = h_2/r_0$

r_0 = radius of earth, h_1 = satellite altitude, h_2 = aircraft altitude

$P_1 = 1 + H_1$, $P_2 = 1 + H_2$

where f is the signal frequency, and v_θ^A and v_φ^A are the θ- and φ-components of the aircraft velocity.

The specular point is at the coordinate $(\theta_{spec}, \pi/2)$ whereas the aircraft is at $(\theta_A, \pi/2)$. Numerical evaluation of θ_{spec} is accomplished as shown in Appendix A. At the specular point the delay is ξ_{spec}. A summary of specular point parameters is given in Table 2-3.

The delay contour defined by $\xi = \xi_{spec} + \Delta\xi$ crosses the $\varphi = \pi/2$ plane at the two points $(\theta_1, \pi/2)$ and $(\theta_2, \pi/2)$, (see Appendix B for numerical evaluation of θ_1 and θ_2). The values of φ along the contour corresponding to values of θ within $[\theta_1, \theta_2]$ are computed numerically using an iterative algorithm. Representative delay contours on the earth's surface are shown in Figs. 2.2 and 2.3 for 10^o, 20^o, and 30^o grazing angles. Note that in each case the delay contours in the vicinity of the specular point tend to be more closely spaced. Although a greater amount of power per unit area may be scattered from this neighborhood, a smaller area exists per unit delay interval. Thus the power per unit delay interval is shaped not only by the scattering cross section, but also by the relative spacing between adjacent delay contours.

When the aircraft velocity vector is perpendicular to the plane of S, A and the specular point, (i.e. cross-plane flight), the Doppler frequency at each (θ,φ) point along the surface is given by (2.2) with $\nu_\theta = 0$, i.e.

$$\nu = -\nu_{max} (1 + H_1) \sin\theta \cos\varphi / R_2 \qquad (2.3)$$

where

$$\nu_{max} = f v_\varphi^A / C \ . \qquad (2.4)$$

Contours of constant normalized Doppler (ν/ν_{max}) are shown in Fig. 2.4 and 2.5 for 10^o, 20^o and 30^o grazing angles. Note that the power observed in each Doppler interval in the receiver is influenced by both the scattered power per unit area and the amount of area between successive contours.

Table 2-3

SUMMARY OF SPECULAR POINT PARAMETERS
(aircraft altitude = 10 km)

Grazing Angle Degrees	θ_A Degrees	θ_{spec} Degrees	ξ_{spec} μsec	$\xi_{spec} - \xi_{dir}$ μsec
5	77.280	76.363446	137500.47	5.30
10	71.938	71.442445	135536.66	11.29
15	66.938	66.608181	133726.73	17.06
20	62.081	61.835971	132009.25	22.67
25	57.320	57.12856	130378.38	28.08
30	52.635	52.479901	128837.58	33.27

θ_A = central angle satellite to aircraft

θ_{spec} = central angle satellite to aircraft

ξ_{spec} = specular point delay

ξ_{dir} = direct path delay

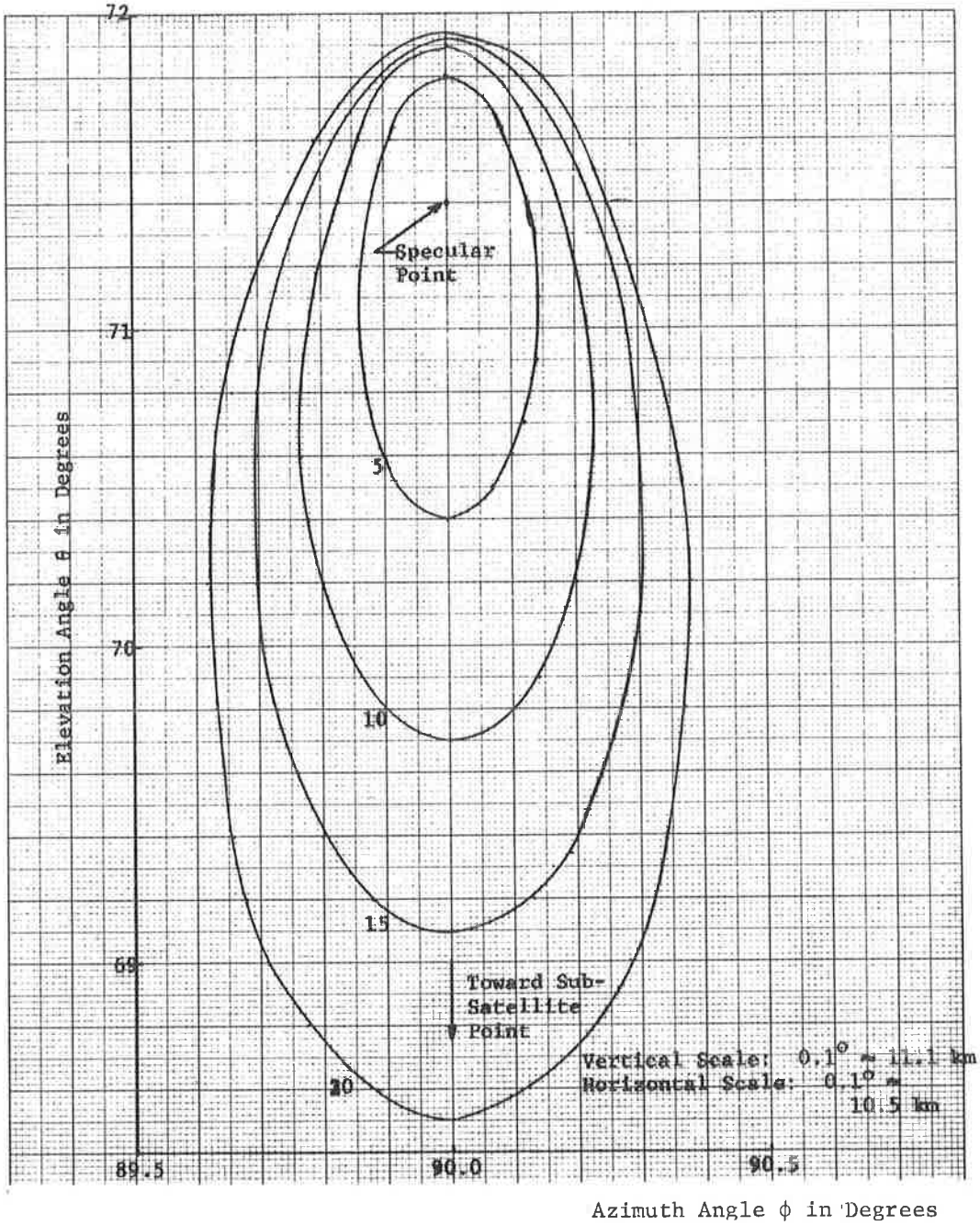

Figure 2.2 Delay Contours on Earth Surface at 10° Grazing Angle (Aircraft Altitude = 10 km)

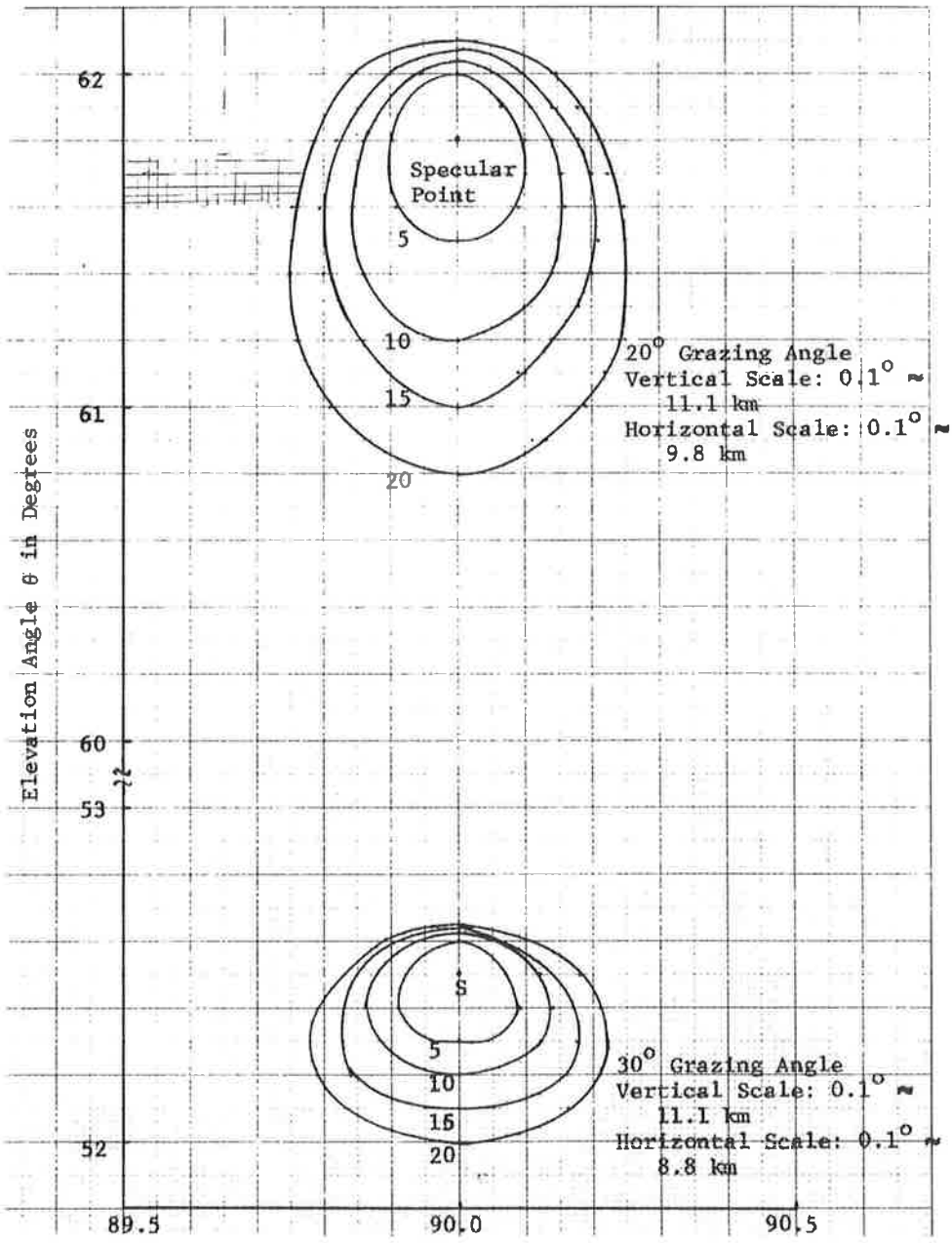

Figure 2.3 Delay Contours on Earth Surface at 20° and 30° Grazing Angles (Aircraft Altitude = 10 Km)

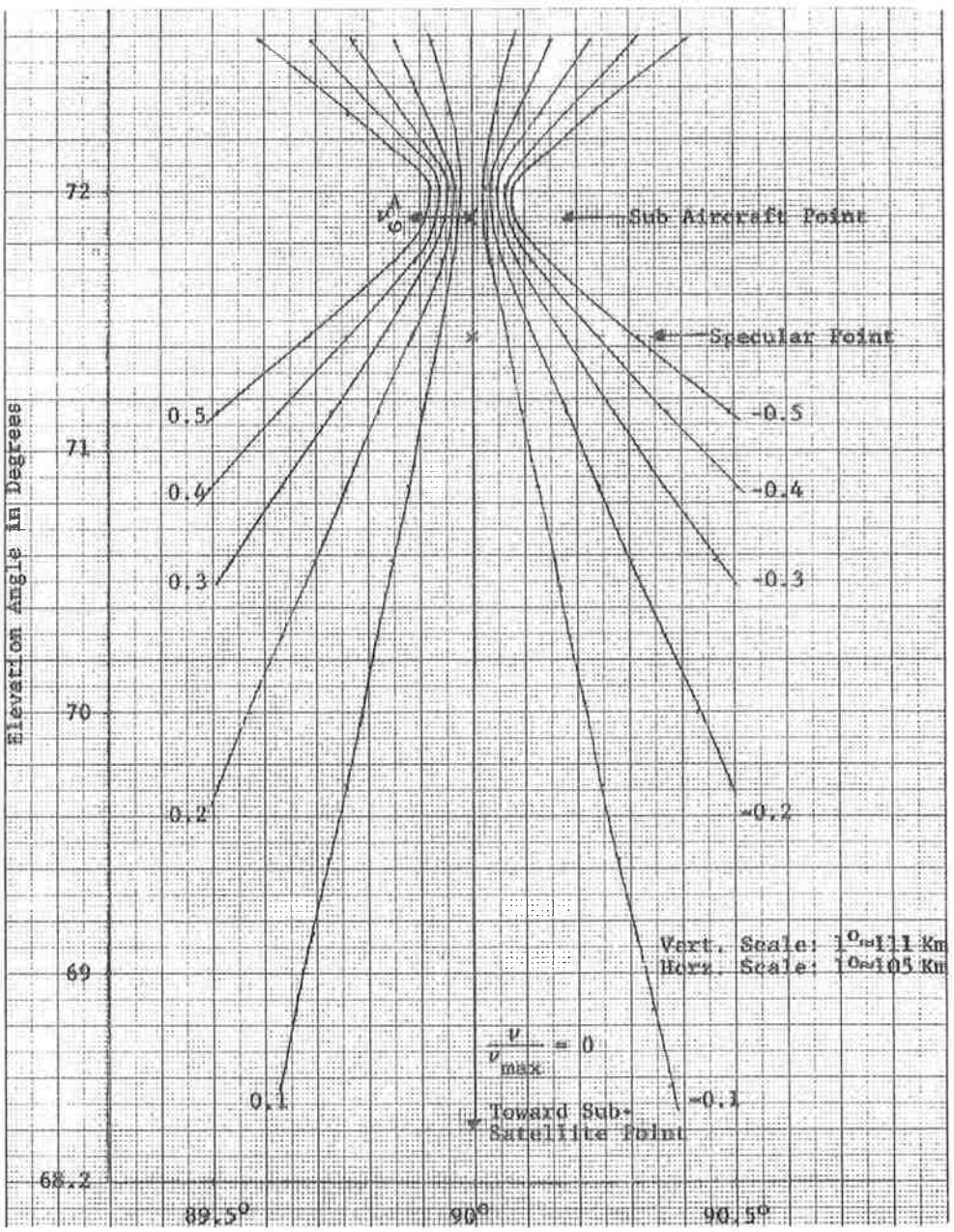

Figure 2.4 Doppler Contours on Earth Surface at 10° Grazing Angle (Aircraft Altitude = 10 Km)

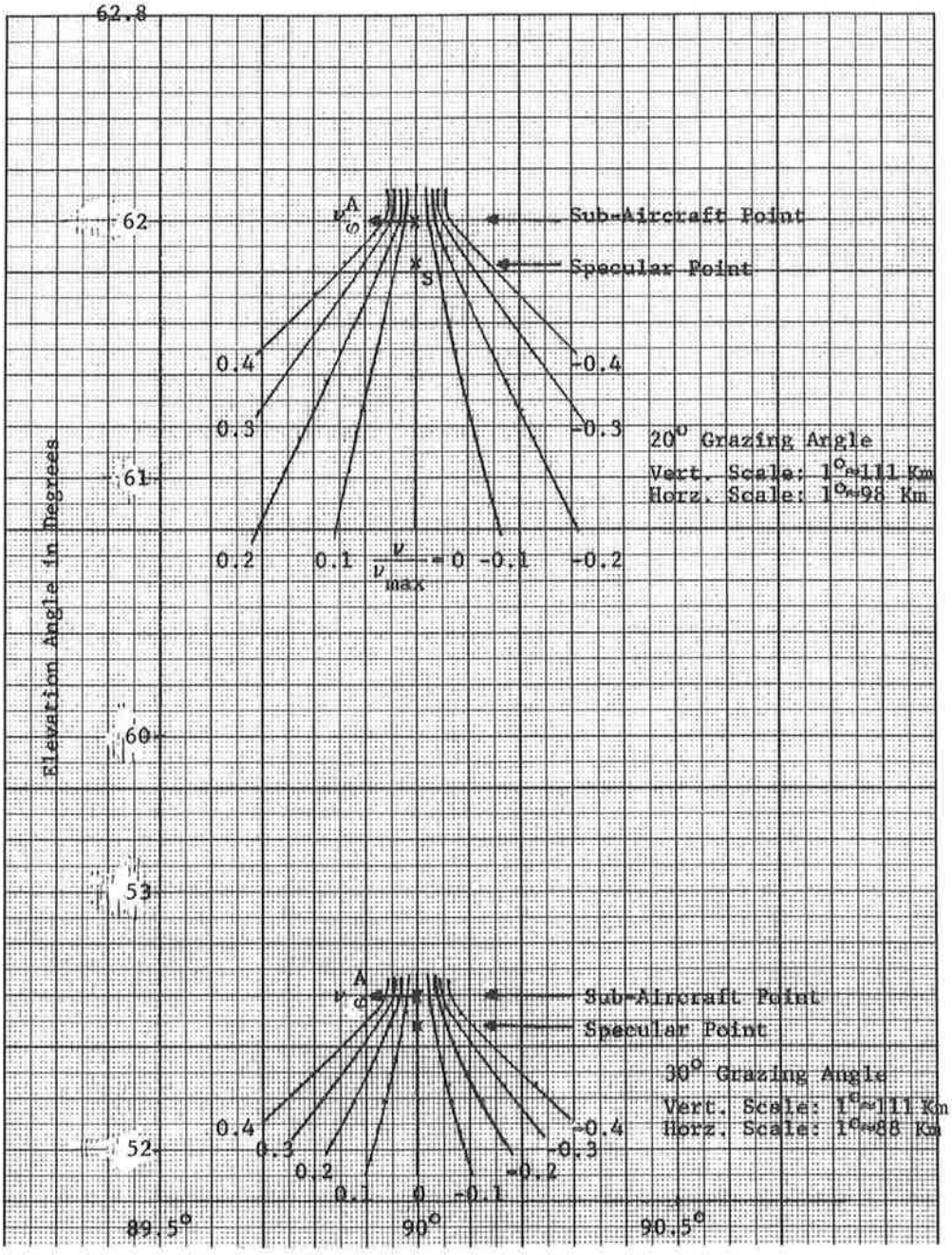

Figure 2.5 Doppler Contours on Earth Surface at 20° and 30° Grazing Angles (Aircraft Altitude = 10 Km)

2.2.2 Antenna Considerations

An antenna with uniform coverage over a lower hemisperical region would weight the scattering cross section by the same amount at each point along the surface, and thus, at each delay-Doppler value along the surface. This would in turn produce an undistorted measurement of the delay and Doppler power spectral densities (psd) in the receiver. Since these power spectral densities affect system performance,* the ideal hemispherical-coverage antenna would also provide realistic performance measures.

In order to provide increased antenna gain it is desirable to use a more directive antenna without seriously distorting the power spectral densities. Specifically, if it is desired to observe the delay psd up to T microseconds without any distortion being introduced by the antenna, then the antenna gain pattern must be uniform over the region of the ocean surface bounded by the T microsecond delay contour. The projection of this region upon a unit sphere at the aircraft gives the angular coordinates over which the illumination from the antenna gain pattern must be uniform (see Fig. 2.6).

It is shown in Appendix D that a point on the ocean surface at the coordinate (θ,φ) projects onto the unit sphere at the elevation angle θ^A and the azimuth angle φ^A, where

$$\cos\theta^A = [(1+H_2) - (\sin\theta_A \sin\theta \sin\varphi - \sin\theta_A \cos\theta)]/R_2 \qquad (2.5)$$

$$\cos\varphi^A = [\sin\alpha(\cos\theta_A \sin\theta \sin\varphi - \sin\theta_A \cos\theta) - \cos\alpha\,(\sin\theta\cos\varphi)]/R_2 \sin\theta^A \qquad (2.6)$$

H_2, R_2 and θ_A are defined in Table 2-2. The antenna coordinate angles θ^A and φ^A are defined in the same way as the Boeing antenna angles, i.e., with $(\theta^A,\varphi^A) = (0,\varphi^A)$ directly above the

*Ranging error is determined by the delay psd or equivalently the frequency correlation function (see [2.2]).

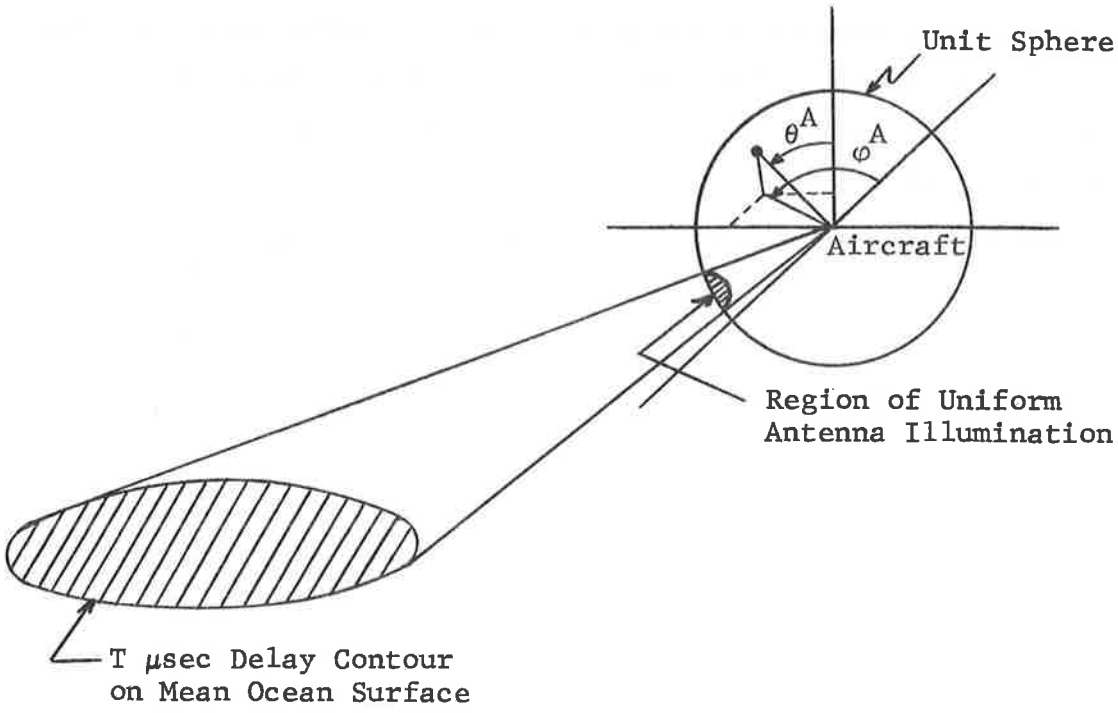

Figure 2.6 Projection of Delay Contours on Unit Sphere at Aircraft

aircraft and $(\theta^A,\varphi^A) = (\pi/2, 0)$ directly ahead of the aircraft. The angle α defines the bearing of the airplane (in level flight) relative to a line perpendicular to the specular point plane of incidence (see Fig. 2.7).

The delay contours shown in Figs. 2.2 and 2.3 are projected on the unit sphere at the aircraft (with α=0) in Figs. 2.6 - 2.8. The azimuth and elevation angle beamwidths necessary to receive power within each of these delay contours can be read directly from these curves. For example, at a 10^o grazing angle, the azimuth and elevation angle beamwidths necessary to receive power within 15 μsec are 74^o and 60^o, respectively.

The unit vectors in the directions of polarization of the satellite and aircraft antennas can be expressed at the local scattering point, in terms of the spherical coordinate unit vectors $\hat{a}_r$, $\hat{a}_\theta$, $\hat{a}_\varphi$. The three separate cases of horizontal, vertical, and circular polarizations are considered. Generally we can write the unit polarization vectors as

$$\hat{p}_S = p_S^H \hat{h}_S + j p_S^V \hat{v}_S \tag{2.7}$$

and

$$\hat{p}_A = p_A^H \hat{h}_A - j p_A^V \hat{v}_A \tag{2.8}$$

where $\hat{h}$ and $\hat{v}$ denote unit vectors in the directions of horizontal and vertical polarizations and the subscripts S and A denote the satellite and aircraft antennas. The constants $p_{S,A}^{H\ V}$ determine the type of polarization according to Table 2-4. The complex polarization vectors account for circular polarization, and $\hat{p}_A$ is the complex conjugate of $\hat{p}_S$ due to the fact that one antenna is used for sending and the other for receiving. Thus the phasing

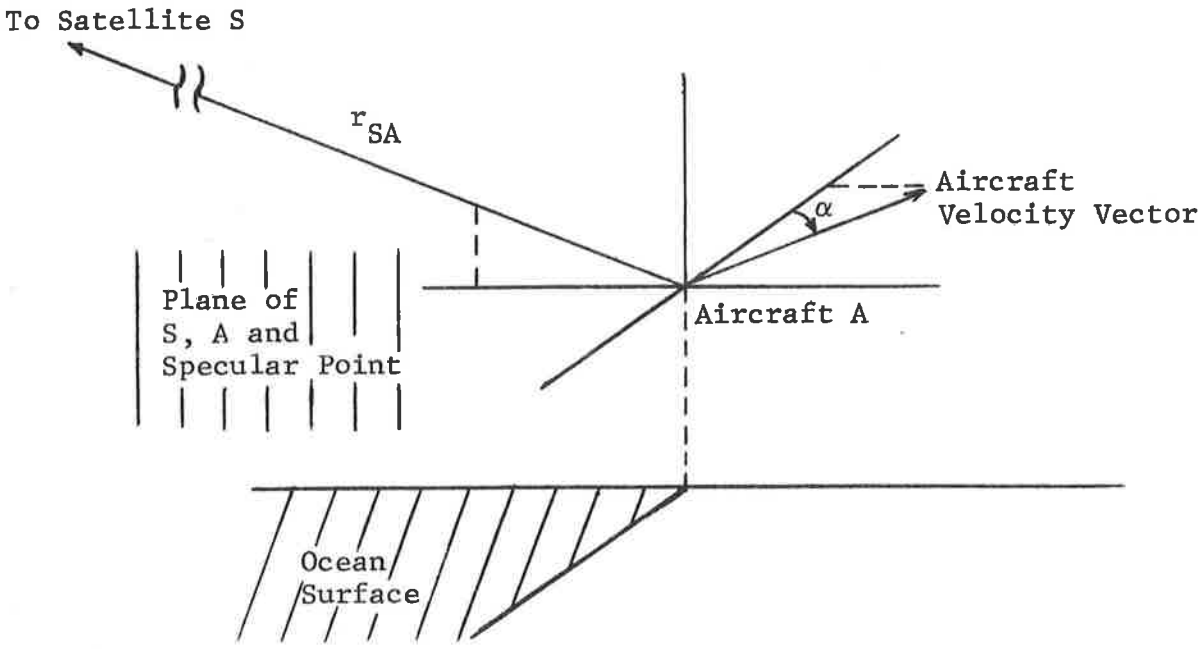

Figure 2.7 Aircraft Heading

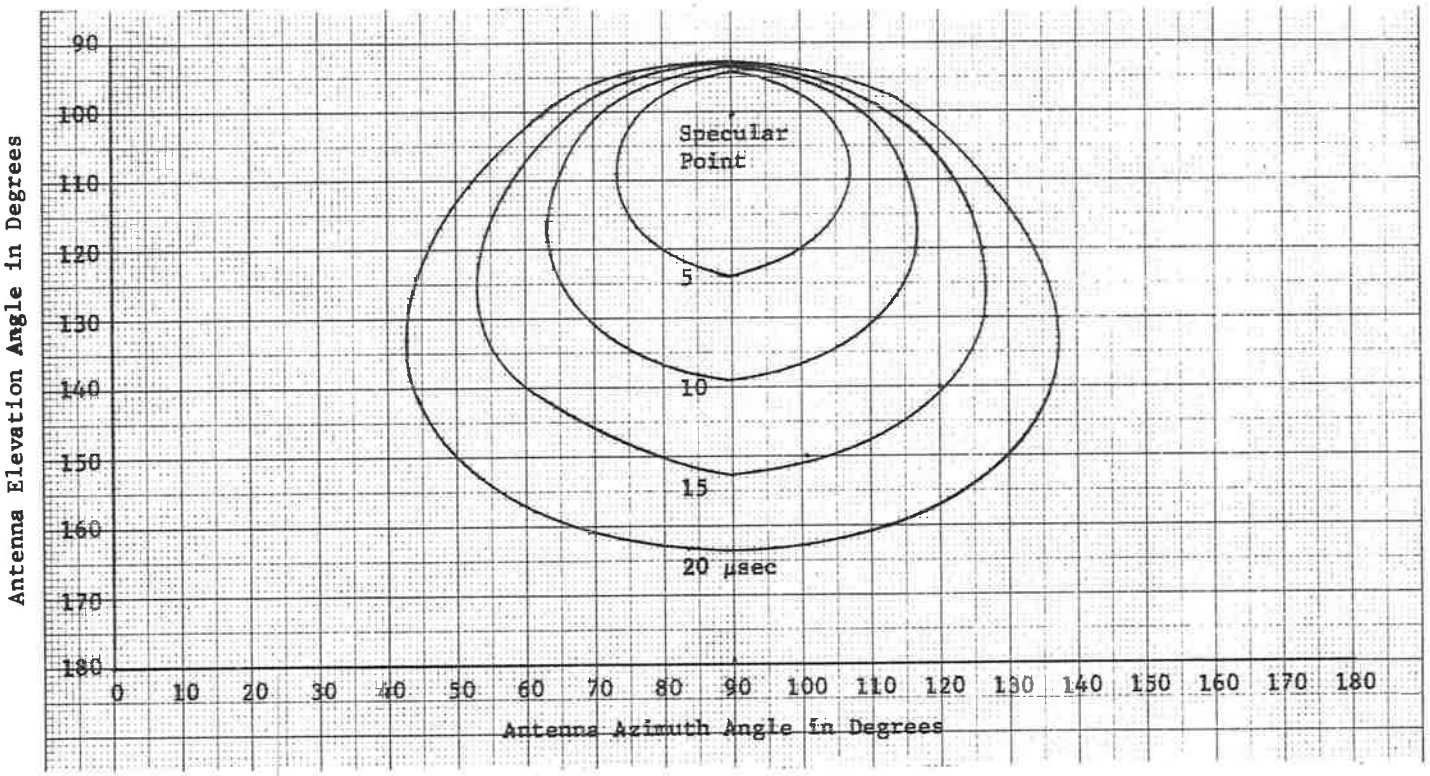

Figure 2.8 Projection of Delay Contours on Unit Sphere at Aircraft for a 10° Grazing Angle (Aircraft Altitude = 10 Km)

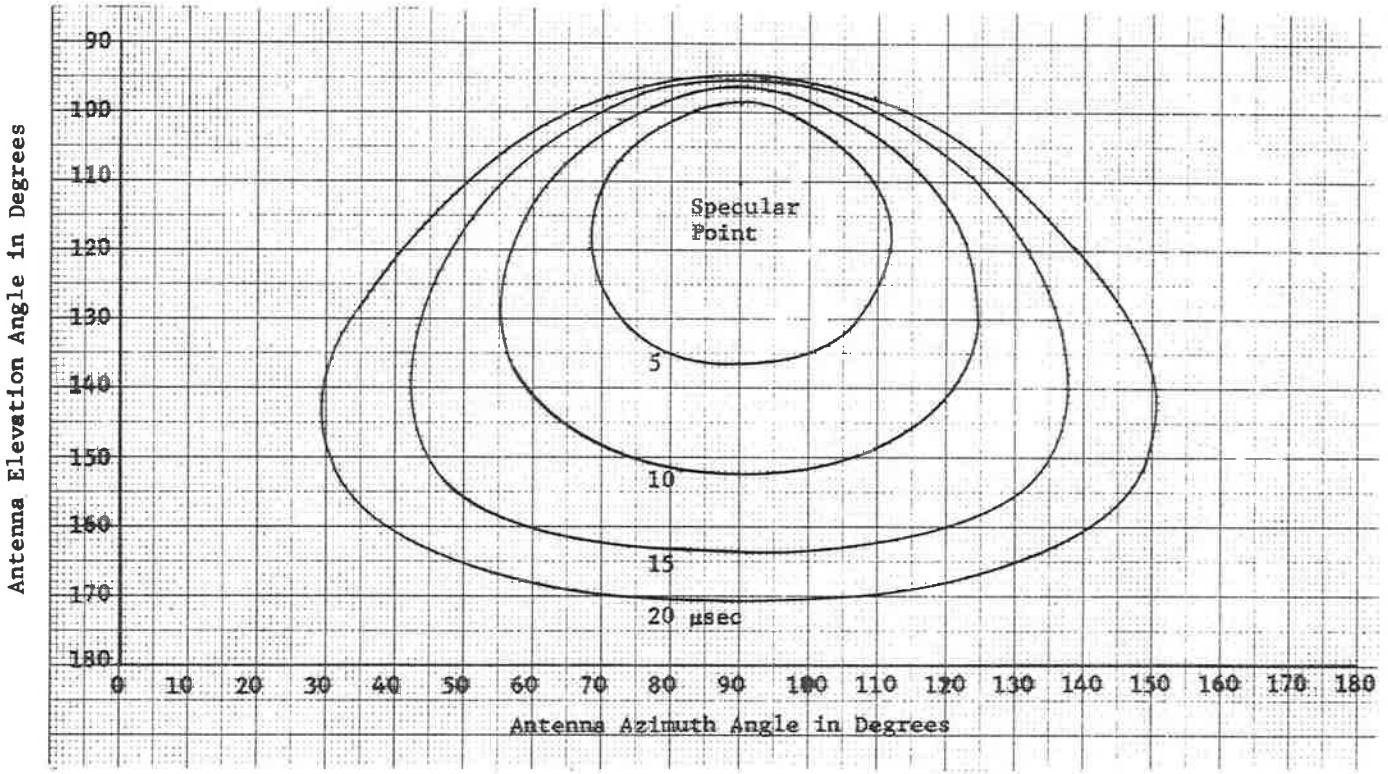

Figure 2.9. Projection of Delay Contours on Unit Sphere at Aircraft for a 20° Grazing Angle (Aircraft Altitude = 10 Km)

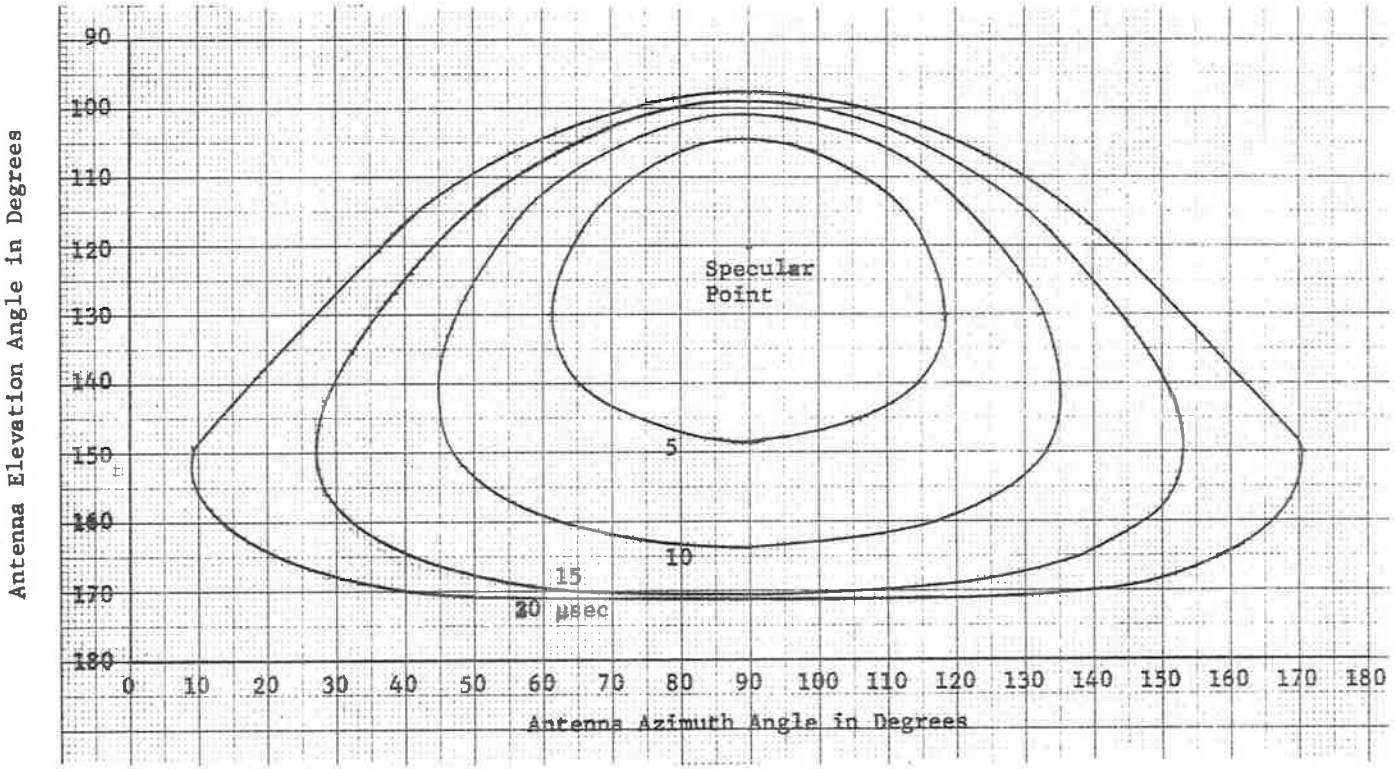

Figure 2.10 Projection of Delay Contours on Unit Sphere at Aircraft for a 30° Grazing Angle (Aircraft Altitude = 10 Km)

Table 2-4

PARAMETER VALUES TO DETERMINE POLARIZATION MODE

Polarization	P_S^H	P_A^H	P_S^V	P_A^V
Horizontal	1	1	0	0
Vertical	0	0	1	1
Circular (same sense)	$1/\sqrt{2}$	$1/\sqrt{2}$	$1/\sqrt{2}$	$1/\sqrt{2}$
Circular (opposite sense)	$1/\sqrt{2}$	$1/\sqrt{2}$	$-1/\sqrt{2}$	$1/\sqrt{2}$

of the receiving antenna is opposite to that of the transmitting so that $\hat{p}_A$ will have the same sense of rotation (for reception) as $\hat{p}_S$ has (for transmission). In all cases, it can be easily verified that on the direct path $\hat{p}_S \cdot \hat{p}_A = 1$.

In order to make specific the definitions of $\hat{h}$ and $\hat{v}$, the plane of incidence is defined as that plane containing the unit vector in the incident direction $\hat{\alpha}$ and $\hat{a}_r$, and the plane of scattering as that containing the unit vector in the scattered direction $\hat{\beta}$ and $\hat{a}_r$. Then the horizontal vectors are defined as perpendicular to the planes of incidence and scattering, such that

$$\hat{h}_S = \hat{\alpha} x \hat{a}_r \tag{2.9}$$

$$\hat{h}_A = \hat{\beta} x \hat{a}_r \tag{2.10}$$

The vertical vectors are defined to lie in the plane of incidence, such that $(\hat{\alpha}, \hat{v}_S, \hat{h}_S)$ and $(\hat{\beta}, \hat{v}_A, \hat{h}_A)$ form orthogonal right-handed sets, i.e.,

$$\hat{v}_S = \hat{h}_S x \hat{\alpha} \tag{2.11}$$

and

$$\hat{v}_A = \hat{h}_A x \hat{\beta} \tag{2.12}$$

Evaluating the indicated vector products, gives

$$\hat{h}_S = -\hat{a}_\varphi \tag{2.13}$$

$$\hat{h}_A = \beta_\varphi \hat{a}_\theta - \beta_\theta \hat{a}_\varphi \tag{2.14}$$

$$\hat{v}_S = \alpha_\theta^2 \hat{a}_r - \alpha_r \alpha_\theta \hat{a}_\theta \tag{2.15}$$

$$\hat{v}_A = (\beta_\theta^2 + \beta_\varphi^2)\hat{a}_r - \beta_r \beta_\theta \hat{a}_\theta + \beta_r \beta_\varphi \hat{a}_\varphi \tag{2.16}$$

where

$$\hat{\alpha} = \alpha_r \hat{a}_r + \alpha_\theta \hat{a}_\theta + \alpha_\varphi \hat{a}_\varphi \tag{2.17}$$

$$\hat{\beta} = \beta_r \hat{a}_r + \beta_\theta \hat{a}_\theta + \beta_\varphi \hat{a}_\varphi \tag{2.18}$$

A detailed evaluation of the various components is given by DeRosa.

2.2.3 The Scattered Power

The bistatic scattering cross-section of the earth's surface is defined as the normalized ratio of δP_S, the differential average power received over the scatter path, to P_d, the power received over the direct path, i.e.,

$$\sigma = \frac{4\pi r_1^2 r_2^2}{r_{SA}^2 \delta A_{mean}} \frac{\delta P_S}{P_d} \tag{2.19}$$

where δA_{mean} is a differential area element on the mean surface.

$$\delta A_{mean} = r_0^2 \sin\theta \delta\theta \delta\varphi \tag{2.20}$$

Substituting (2.20) into (2.19) and solving for $P = P_S/P_d$ gives the total normalized multipath power

$$P = \frac{r_{SA}^2}{4\pi} \iint_{surface} \frac{\sigma(\theta,\varphi)}{r_1^2 r_2^2} r_0^2 \sin\theta \, d\theta d\varphi \tag{2.21}$$

The scattering cross-section is shown by DeRosa [2.1] to be given by

$$\sigma = G_S G_A \sigma^0 \tag{2.22}$$

where G_S amd G_A are the normalized gain patterns of the satellite and aircraft, and σ^0 is the scattering cross-section when omni-directional antennas are used.

$$\sigma^0 = \frac{\pi}{q_r^2} |A_S|^2 GP\left(\frac{q_\varphi}{q_r}, \frac{q_\theta}{q_r}\right) \tag{2.23}$$

where

$$\vec{q} = q_r \hat{a}_r + q_\theta \hat{a}_\theta + q_\varphi \hat{a}_\varphi = \hat{\alpha} - \hat{\beta} \tag{2.24}$$

The unit vectors $\hat{\alpha}$ and $\hat{\beta}$ are in the incident and scattered directions, respectively, and A_S is given by

$$A_S = \frac{2}{\hat{n}\cdot\hat{a}_r} \left\{ -(\hat{n}\cdot\hat{\alpha})(\hat{p}_A\cdot\hat{p}_S) + \frac{\hat{n}\cdot\hat{p}_A}{\sqrt{\epsilon_r - 1 + (\hat{n}\cdot\hat{\alpha})^2}} \left[-(\hat{n}\cdot\hat{\alpha})(\hat{\beta}\cdot\hat{p}_S) \right.\right.$$

$$\left.\left. + (\hat{n}\cdot\hat{p}_S)(\hat{\alpha}\cdot\hat{\beta}) \right] + (\hat{n}\cdot\hat{p}_S)(\hat{\alpha}\cdot\hat{p}_A) \right\} \tag{2.25}$$

where $\hat{p}_S$ and $\hat{p}_A$ are the unit polarization vectors of the satellite and aircraft, respectively, and the unit normal $\hat{n}$ has the stationary phase value

$$\hat{n} = (\hat{\alpha} - \hat{\beta}) / |\hat{\alpha} - \hat{\beta}| \tag{2.26}$$

The relative complex dielectric coefficient of the ocean is given by

$$\epsilon_r = \frac{\epsilon}{\epsilon_0}\,(1 - j\sigma/\omega\epsilon) \tag{2.27}$$

For sea water ϵ is approximately $80\epsilon_0$ and σ is approximately 4 mhos/meter [2.3], so that at L-band (f = 1.6 GHz), the relative complex dielectric constant becomes

$$\epsilon_r = 80(1 - j0.56) \tag{2.28}$$

G is the antenna gain pattern evaluated at the scattering point, and P is the two-dimensional probability density function of the surface slopes, which is assumed to be Gaussian, i.e.,

$$P(Z_\varphi, Z_\theta) = \frac{1}{2\pi(\sigma/L)^2} \exp\,[-(Z_\varphi^2 + Z_\theta^2)/2(\sigma/L)^2] \tag{2.29}$$

The rms height is σ and the correlation length along the surface is L. The rms slope for a Gaussian surface with a Gaussian correlation function is then σ/L [2.4].

2.3 SEA STATE MEASUREMENTS

The purpose of this section is to define the specific sea state descriptors which should be measured and the various methods available for performing such measurements. It is shown in Section 2.3.1 that these descriptors are the power spectral density (psd) of the small-scale sea surface fluctuations and the rms slope of the large-scale fluctuations. At L-band the small-scale psd need be measured only over the range of spatial frequencies less than 5.3 cycles/meter. The recommendations for usage of the various measurement techniques are summarized in Table 2-5.

2.3.1 Sea State Descriptors

Ocean waves are classified according to the period (or frequency) of a vertical oscillation at a single point along the surface. A chart of these classifications as given in [2.8] is shown in Table 2-6. The period T of the wave is related to the wavelength L by [2.8]

$$L = \frac{g}{2\pi} T^2 \tag{2.30}$$

where g is the acceleration due to gravity (980 cm/sec^2). A summary of the temporal and spatial relationships used to describe ocean surface waves is given in Table 2-7. A schematic representation of the surface wave psd, similar to that presented in [2.8], is given in Fig. 2.11.

Table 2-5

SUMMARY OF SEA STATE MEASUREMENT RECOMMENDATIONS

Measurement Technique	Recommended For Use
Sea Photo Analysis	Yes
Spar Buoy	Yes
Laser Profilometer	No
Radar Altimeter	No
Anemometer	Yes
Hindcast Data	Yes
Visual Observations	Yes

Table 2-6

OCEAN WAVE CLASSIFICATION

Classification	Period Band in Seconds		
Capillary	0	to	0.1
Ultragravity	0.1	to	1.0
Gravity	1.0	to	3.0
Infragravity	30	to	300
Long Period	300	to	24 (hours)
Transtidal	24 (hours)	to	∞

Table 2-7

SUMMARY OF SPACE AND TIME VARIABLES FOR OCEAN SURFACE WAVES

Time (Frequency) Variable	Relationship	Space (Wavenumber) Variable
Radian Frequency ω $(\frac{\text{rad}}{\text{sec}})$	*$k = \frac{\omega}{v}$	Wavenumber k $(\frac{\text{rad}}{\text{meter}})$
Frequency $f = \frac{\omega}{2\pi}$ $(\frac{\text{cycles}}{\text{sec}})$	$S = \frac{f}{v}$	Spatial Frequency $S = \frac{k}{2\pi}$ $(\frac{\text{cycles}}{\text{meter}})$
Period $T = \frac{1}{f}$ $(\frac{\text{sec}}{\text{cycle}})$	$L = vT$	Wavelength $L = \frac{1}{S}$ $(\frac{\text{meters}}{\text{cycle}})$

*v = wave velocity

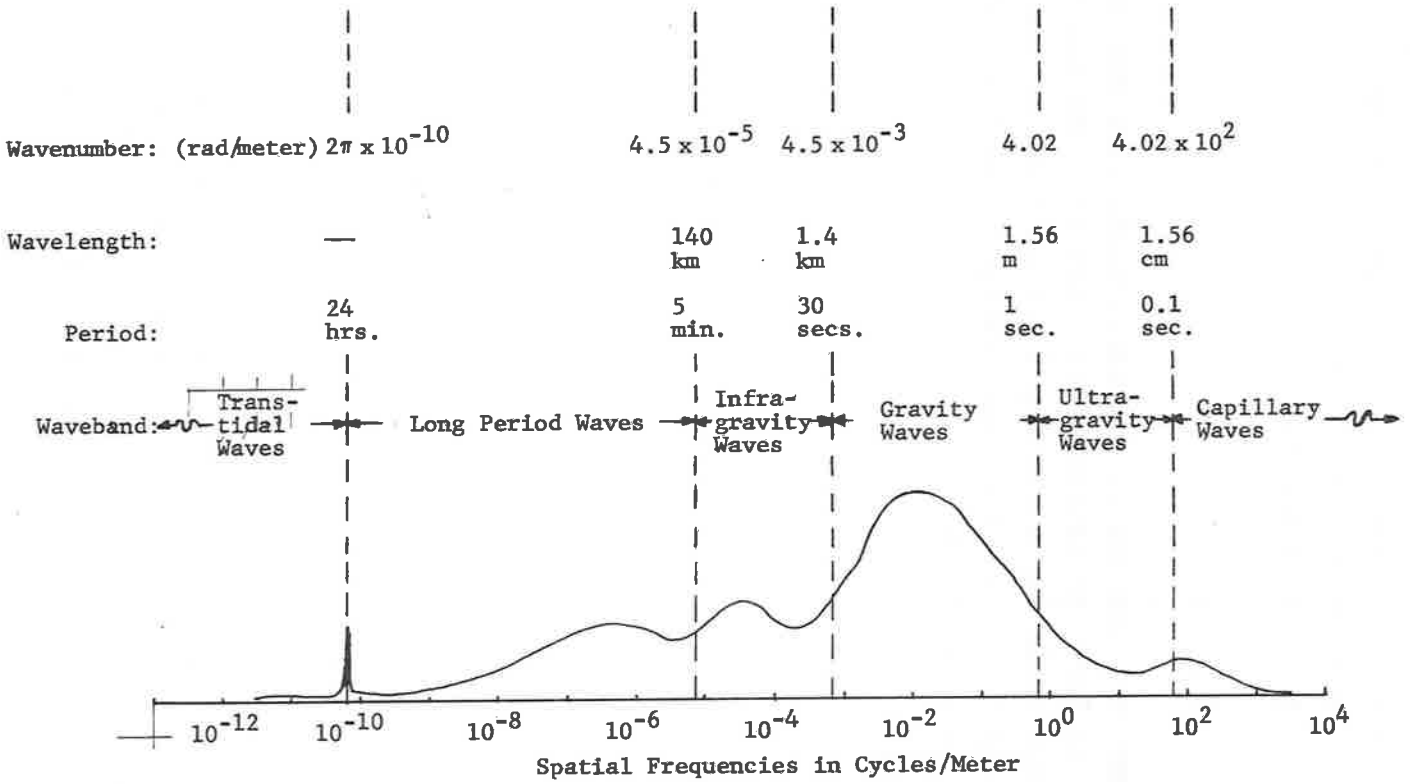

Figure 2.11 Schematic Representiation of Ocean Surface Power Spectral Density

The sea state descriptors which need to be measured are those which affect the bistatic scattering cross-section σ. DeRosa [2.17] has shown that for a composite (two-scale) surface σ is given by the sum of two terms, i.e.,

$$\sigma = \sigma_{LS} + \sigma_{SS} \tag{2.31}$$

where σ_{LS} and σ_{SS} are due to the large-scale (LS) and small-scale (SS) surface undulations, respectively. The two terms depend on the probability density function (pdf) of the LS surface slopes $p(Z_x,Z_y)$ and the power spectral density (psd) of the SS surface heights $S(k_x,k_y)$ as

$$\sigma_{LS} \sim p\left(\frac{q_x}{q_z}, \frac{q_y}{q_z}\right) \tag{2.32}$$

$$\sigma_{SS} \sim S(kq_x, kq_y) \tag{2.33}$$

where

$$q_x = \sin\theta_S \cos\varphi_S \tag{2.34}$$

$$q_y = \sin\theta_i - \sin\theta_S \sin\varphi_S \tag{2.35}$$

$$q_z = -(\cos\theta_i + \cos\theta_s) \tag{2.36}$$

$$k = 2\pi/\lambda \tag{2.37}$$

$$\lambda = \text{wavelength of carrier} \tag{2.38}$$

There is some theoretical evidence [2.9] that to a first approximation, the SS scatter component is negligibly small compared to the LS component in the vicinity of the specular point. However, in the event that the SS scatter component proves to be of appreciable magnitude in the experimental flight tests, it will become necessary to use the more sophisticated composite model. This being the case, it will then be necessary to have measurements of both scales of roughness.

Derivations of σ_{LS} and σ_{SS} are made using the Kirchoff approximation and the small perturbation method, respectively. These require that for the LS surface undulations, the Brekhovskii condition [2.10] is satisfied

$$4\pi\rho_{LS} \sin\gamma \gg \lambda \ , \tag{2.39}$$

and for the SS surface undulations, only small perturbations are considered [6], [7]

$$\sigma_{SS} \ll \lambda/2\pi \tag{2.40}$$

$$\alpha_{SS} \ll 1 \tag{2.41}$$

where

ρ_{LS} is the local radius of curvature of the LS surface

γ is the local grazing angle of the incident radiation

λ is the wavelength of the incident radiation

σ_{SS} is the rms height of the SS surface

α_{SS} is the rms slope of the SS surface.

In Appendix E, it is shown that the minimum value of the radius of curvature for a sinusoidal component is given by

$$\rho_{min} = \frac{1}{k^2 H} = \frac{L^2}{(2\pi)^2 H} = \frac{1}{k^2\sigma\sqrt{2}} \tag{2.42}$$

where

H is the wave amplitude

σ is the rms wave amplitude

L is the wavelength

$k = \frac{2\pi}{L}$ is the wavenumber.

Then for each spectral component of the LS surface, the Brekovskii condition(2.39) which is necessary to ensure the validity of the Kirchoff approximation, can be written as

$$k \ll k_0 \tag{2.43}$$

where

$$k_0 = \sqrt{\frac{4\pi \sin\gamma}{\lambda H}} = \sqrt{\frac{4\pi \sin\gamma}{\lambda\sigma\sqrt{2}}} \tag{2.44}$$

Using $k_0/10$ as k_{max}, the maximum value of k which is very much less than k_0, gives the requirement

$$k < k_{max} = k_0/10 \tag{2.45}$$

Thus LS surface fluctuations are those spectral components which satisfy [2.11].

Cox and Munk [2.11] have shown that the pdf of the LS slopes is approximately zero-mean Gaussian. Thus in order to characterize σ_{LS}, we need to determine the rms slope of the large-scale component.

From (2.33), it is obvious that $S(k_x,k_y)$ need be known only over the range of kq_x and kq_y. From (2.34) through (2.37), it is obvious that

$$0 \leq |kq_x| \leq 2\pi S_{max} \tag{2.46}$$

where the maximum spatial frequency S_{max} is given by

$$S_{max} = \frac{(kq_x)_{max}}{2\pi} = \frac{1}{\lambda} \tag{2.47}$$

An identical relationship holds for kq_y. A graph of maximum spatial frequency (Fig. 2.12) shows that for L-band propagation (1.6 GHz), we only need measure the small-scale psd of ocean waves with spatial frequencies $S \leq 5.3$ cycles/meter (wavelengths $L \geq 19$ cm/cycle or wavenumbers $k \leq 33.3$ radians/meter). From Fig. 2.11, it is seen that the highest frequency waves that we need observe are in the ultra gravity region.

2.3.2 Measurement Techniques

Several techniques for measurement of sea state descriptors are discussed in this section:

a) Sea photo analysis
b) Spar buoy methods
c) Laser profilometer
d) Radar altimeter
e) Local anemometer
f) NOO hindcast data
g) Visual observations.

Each of the methods is detailed in the subsequent sections, and recommendations are made for utilizing the better methods. From the list above, a, b, e, f, and g are recommended for usage while c and d are not.

2.3.2.1 Sea Photo Analysis

In the photographic analysis developed by Stillwell [2.14], the wave height spectrum of surface waves is deduced from oblique photographs. The output of this analysis is a contour plot of constant spectral amplitude in the region photographed. For ultragravity and smaller wavelength gravity waves, 2 low-altitude, orthogonal flight trajectories would have to be flown. For longer wavelength, wind-driven gravity waves, a similar flight would be made in the direction of the wind using a strip camera. The flights would be a few miles in duration, and all the necessary photographs could be taken in 6 to 10 minutes.

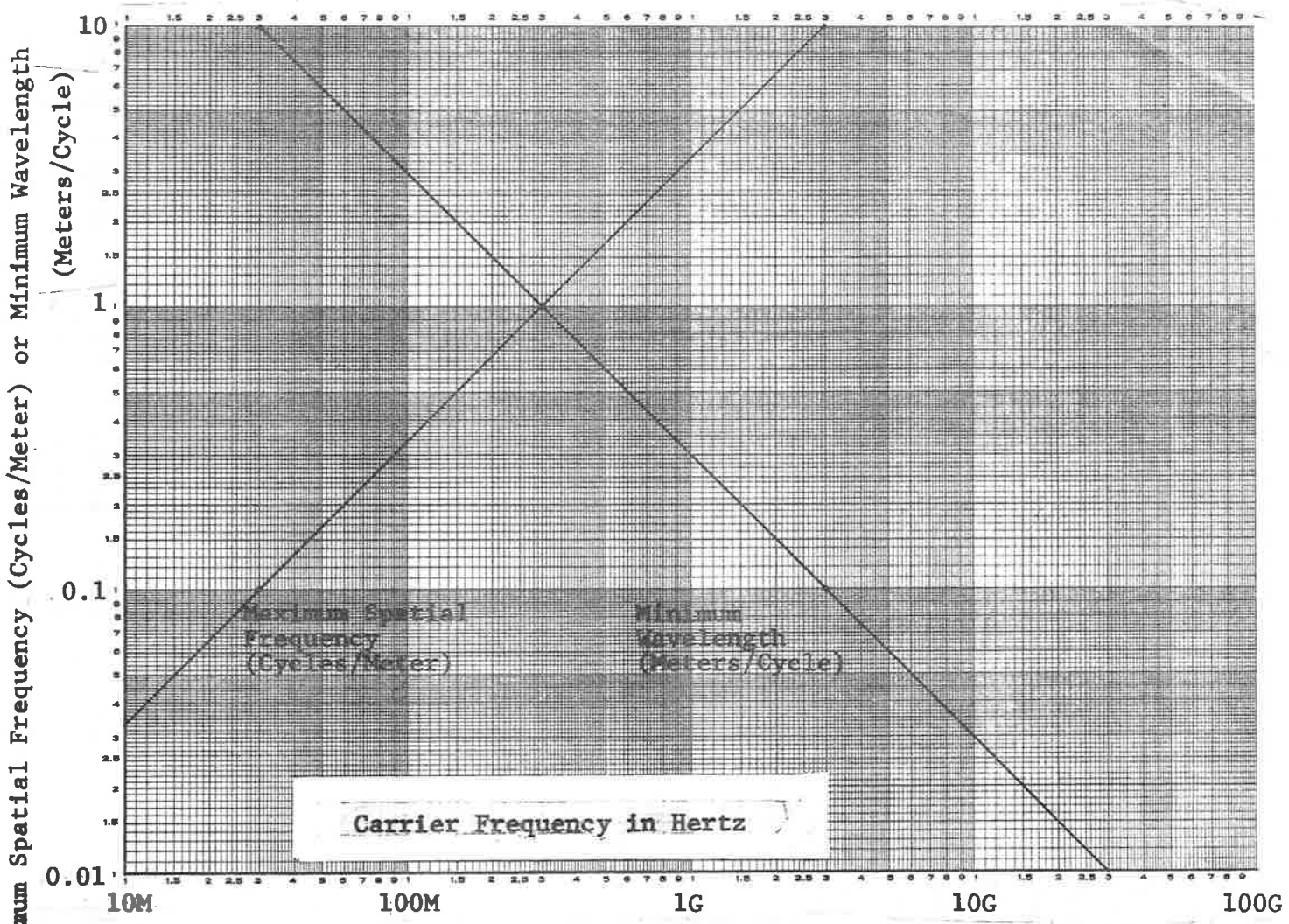

Figure 2.12 Maximum Spatial Frequency (Minimum Spatial Wavelength) Which Contributes to Scattering Cross Section at a Given Carrier Frequency

If two sets of data were taken to increase reliability, up to about 20 minutes of test time would be necessary. If there is no weather front within about 100 to 200 miles, these measurements should be accurate for about 3 or 4 hours.

Measurements of the smaller wavelength surface waves have been made using a frame camera, and sufficient documentation exists[2.14]to judge the method as a reliable means for obtaining the relevant sea state descriptors. The strip camera method has been used only a few times, and although some success was achieved, documentation on the tests is not yet available.

The photo analysis fails in hazy conditions and when there is a predominance of white-capping. Also, since strip camera photographs are taken only in the direction of the local wind field, swell components generated outside the region which propagate in a different direction are not measured. For these reasons a second sea state measurement technique should be used in conjunction with the photo analysis.

2.3.2.2 Spar Buoy Methods

A spar buoy is a long cylinder which floats vertically in the water with its upper end exposed. The cylinder is attached by cable to a deeply submerged (~300 feet) damping disk (diameter ~4 feet). The buoy is damped sufficiently so that it remains stationary relative to the surface waves. A step resistance or continuous wire gage[2.15]attached to the top of the cylinder at water level can then be used to measure the ocean surface height. The data can be telemetered to a nearby (buoy-tending) ship or recorded aboard the buoy and later retrieved by the ship.

By using two gages separated by a horizontal distance d, an approximate wave slope can be determined as the ratio of the height difference Δz to the distance d. In order to determine the value of d necessary to get the rms slope of the LS surface components, we will express the surface height $z(x,y,t)$ as the sum of LS and SS terms, i.e.,

$$z(x,y,t) = z_{LS}(x,y,t) + z_{SS}(x,y,t) \tag{2.48}$$

Considering the variation of z in only one coordinate direction at a fixed time t_0 gives

$$\Delta z = [z_{LS}(x+d) - z_{LS}(x)] + [z_{SS}(x+d) - z_{SS}(x)] \tag{2.49}$$

Assuming Δz is zero mean, its variance is given by

$$\overline{(\Delta z)^2} = 2\sigma_{LS}^2[1-\rho_{LS}(d)] + 2\sigma_{SS}^2(1-\rho_{SS}(d)] \tag{2.50}$$

where σ_{LS}^2, σ_{SS}^2 are the variances and ρ_{LS}, ρ_{SS} are the normalized correlation functions of the LS and SS components, respectively.

Now if d is chosen much less than the reciprocal of the highest (spatial) frequency component of the LS fluctuations, ρ_{LS} cannot vary rapidly within d and is closely approximated by the first two (non-zero) terms of its power series expansion, i.e., for

$$d \ll 1/(S_{LS})_{max} \tag{2.51}$$

$$\rho_{LS}(d) \approx 1 + \frac{\partial^2\rho_{LS}(0)}{\partial x^2}\frac{d^2}{2} \tag{2.52}$$

If d is also chosen much larger than the correlation width of the SS fluctuations, then

$$\rho_{SS}(d) \approx 0 \tag{2.53}$$

Substituting (2.52) and (2.53) into (2.50) gives

$$\overline{(\Delta z)^2} = -\frac{\partial^2\rho_{LS}(0)}{\partial x^2}\sigma_{LS}^2 d^2 + 2\sigma_{SS}^2 \tag{2.54}$$

But from Papoulis [2.16, p. 317],

$$\frac{\partial^2 \rho_{LS}(0)}{\partial x^2} = \frac{-\alpha_{LS}^2}{\sigma_{LS}^2} \tag{2.55}$$

where α_{LS}^2 is the variance of the LS slopes. Substituting (2.55) into (2.54) and dividing by d^2 gives

$$\alpha_{LS}^2 = \overline{\left(\frac{\Delta z}{d}\right)^2} \left[1 - \frac{2\sigma_{SS}^2}{\overline{(\Delta z)^2}}\right] \tag{2.56}$$

Since

$$\overline{(\Delta z)^2} = \sigma_{LS}^2 + \sigma_{SS}^2 \ , \tag{2.57}$$

$$\alpha_{LS}^2 = \overline{\left(\frac{\Delta z}{d}\right)^2} \left[1 - \frac{2\sigma_{SS}^2}{\sigma_{LS}^2 + \sigma_{SS}^2}\right] \tag{2.58}$$

Thus if $\overline{(\Delta z/d)^2}$ is used as the estimate of α_{LS}^2, it becomes a biased estimate with a relative error of $2\sigma_{SS}^2/(\sigma_{LS}^2 + \sigma_{SS}^2)$.

In order to determine the rms slope in both the x- and y-directions along the surface, three vertical wave-height gages can be mounted in two orthogonal x-z and y-z planes.

2.3.2.3 Laser Profilometer

The laser profilometer is essentially an airborne altimeter which uses an amplitude modulated beam. The range from the aircraft to a surface reflection point is determined by comparing the phase of the received modulation with that of the transmitted modulation. There are several difficulties associated with laser profilometer measurement methods:

1) Measurements can not be obtained in hazy conditions
2) Aircraft speed is different from phase speed of each wave
3) Aircraft vertical motion induces surface profile errors.

If the profilometer were to be used as a back-up measurement to the sea photo analysis, 1) above indicates that both techniques would fail under the same (hazy) conditions. Also since the ocean is a dispersive medium to surface waves, each spectral component travels at a different velocity relative to the aircraft making 2) above a severe restriction. Finally, 3) above can falsely indicate the presence of large-scale surface components.* For these reasons it is recommended that the laser profilometer not be used for measurement of sea state descriptors.

2.3.2.4 Radar Altimeter

NRL has used a radar altimeter with a few nanosecond pulse widths to determine the peak-to-trough heights of the ocean surface. This is done by examining the spread of the returned pulse.† By flying at 500 feet they can map the surface heights in the same manner as a laser profilometer. At higher altitudes the average peak-to-trough heights over the illuminated area are determined. NRL has not yet supplied any documentation on the method or equipment, so it is difficult to assess the value of a radar altimeter to measure rms sea slope. Yaplee at NRL was not aware of an existing method for determining rms sea slope directly from their altimeter measurements.

*This may not be a severe limitation, since the slow motion of the aircraft could either be filtered out or accounted for by accelerometer data.

†It is interesting to note that this amounts to remotely sensing the ocean by examining multipath spread which is in many ways equivalent to predicting multipath spread by knowing sea state.

Since the radar altimeter does not suffer from the weather limitations of the photographic and laser methods, and since it can provide a synoptic view of the entire test region, it represents an excellent probe for sea state. However, there does not seem to exist a specific method whereby the rms slope of the surface can be determined. Unless NRL or other experimenters can demonstrate this ability, it is recommended that a radar altimeter not be used.

2.3.2.5 Local Anemometer

The measurement of wind velocity in the local scattering region can be used in empirical relationships to crudely determine rms sea slope and wavenumber spectrum. Cox and Munk used sun glitter measurements to determine rms slope for both a normal and oil-slicked ocean in terms of the wind velocity measured 41 feet above the surface. The oil slick effectively eliminates wavelengths shorter than one foot. The wave height spectrum for fully developed seas has been given by Pierson and Moskowitz[2.18]in terms of the wind speed measured 64 feet above the mean ocean surface. It is reasonable to assume that there is not much wind shear between the 41 feet and 64 feet, so that anemometer measurements can be taken anywhere in that interval to use the empirical results above.

2.3.2.6 Hindcast Data

The Naval Oceanographic Office gives hindcast data on wave height and period near the test area. They also forecast wind speed and direction of swell. However, since this data can be very inaccurate, [2.19]. it is recommended that hindcast data be obtained only to back up measurements made in the test area.

2.3.2.7 Visual Observations

Visual observations in the form of photographs taken from a ship in the test area will be useful for estimating approximate sea state. Although this information is not critical, it is useful and the cost of obtaining it is incremental compared to the costs of obtaining more definitive data.

2.4 SENSITIVITY ANALYSIS OF RECORDED FLIGHT PARAMETERS

This section examines the relationship between channel parameter measurements and measurements of aircraft altitude, heading, speed, pitch and roll, as well as rms sea slope. A rough estimate of these effects is derived from the first-order steepest descent approximation applied to the Kirchoff model [2.5]. The errors introduced into the channel measurements are manifested by an apparent change in effective width of either the delay or Doppler power spectral density (psd) or a change in received multipath power. The calculations are made for "cross-plane" flights. Similar calculations can be made for "in-plane" flights.

The relative error ϵ_T in the duration of the delay psd is shown to be equal to the relative error in the altitude measurement. The heading error is shown to reduce multipath power by effectively reducing the antenna beamwidth. The relative error ϵ_B in Doppler bandwidth is equal to the relative error in the speed measurement. Near level flights, ϵ_B is less than the pitch angle divided by the tangent of the grazing angle. The roll again effects apparent antenna beamwidth. Lastly, ϵ_B is equal to the relative error in the measurement of rms sea slope while ϵ_T is twice this value. Some typical flight parameter errors are listed in Table 2-8 with corresponding channel parameter errors.

The accuracy to which the flight parameters are to be recorded aboard the aircraft is determined by the accuracy to which the delay and Doppler power spectral densities are to be measured. The errors in the spectral densities can be measured either by the total area under each curve or by the effective width of each. The delay spectrum $Q(\xi)$ and the Doppler spectrum $P(\nu)$ are given by Bello [2.5].as

$$Q(\xi) = \frac{1}{4\alpha^2 H/c} \exp\left[-\left(\frac{\sin\theta + 1/\sin\theta}{2}\right)\left(\frac{\xi}{4\alpha^2 H/c}\right)\right] I_0\left[\left(\frac{\frac{1}{\sin\theta} - \sin\theta}{2}\right)\frac{\xi}{4\alpha^2 H/c}\right] \qquad (2.59)$$

TABLE 2-8. THE EFFECTS OF ERRORS IN RECORDED FLIGHT PARAMETERS ON CHANNEL MEASUREMENTS

Flight Parameter (FP)	Error in FP	Relative Error in FP	Relative Error in Width of $Q(\xi)$	Relative Error in Doppler Bandwidth	Multipath Power Change
Altitude	$\pm$ 300 ft.	$\pm$ .01	$\pm$ .01	—	—
Heading	$\pm 5^{o}$	—	—	—	0.25 dB
Speed	$\pm$ 10 knots	$\pm$ .025	—	$\pm$ .025	—
Pitch	$\pm 3^{o}$	—	—	$\pm$ .03	—
Roll	$\pm 3^{o}$	—	—	—	< 3 dB†
RMS Sea Slope*	$\pm$ .002	$\pm$ .01	$\pm$ .02	$\pm$ .01	—

*Note: Here rms sea slope α = 0.2, while Boeing defines rms sea slope = $\sqrt{2}\ \alpha$ = 0.28.

†This loss can be recovered by proper antenna design (see Section 2.5.1.3)

and

$$P(\nu) = \frac{\sqrt{2}}{B_{rms}\sqrt{\pi}} \exp\left(-\frac{2\nu^2}{B_{rms}^2}\right) \tag{2.60}$$

where

$$B_{rms} = 4\left(\frac{f_0}{c}\right)\alpha \sqrt{(v_x \sin\theta + v_z \cos\theta)^2 + v_y^2 \sin^2\theta} \tag{2.61}$$

The indicated parameters have the following definitions:

α = rms sea slope
H = height of aircraft above ocean (x-y plane)
c = speed of propagation
θ = grazing angle of scattered ray
f_0 = carrier frequency (1.6 GHz)
(v_x, v_y, v_z) = velocity of aircraft in x,y,z directions.

2.4.1 Aircraft Altitude

From Eq. (2.59) it is seen that the accuracy to which the delay psd $Q(\xi)$ is measured is dependent upon the accuracy to which the aircraft altitude H is measured. Using the change of variable

$$\delta = \xi/4\alpha^2(H/c) \tag{2.62}$$

area under $Q(\xi)$ can be expressed as

$$\rho = \int f(\delta)\, d\delta \tag{2.63}$$

where

$$f(\delta) = \exp\left[-\left(\frac{\sin\theta + 1/\sin\theta}{2}\right)\delta\right] I_0\left[\left(\frac{\frac{1}{\sin\theta} - \sin\theta}{2}\right)\delta\right] \tag{2.64}$$

Note that the shape of the normalized psd $f(\delta)$ does not depend on H. When the aircraft is at an altitude H_0, the $\frac{1}{e}$ duration of $f(\delta)$ is some value Δ_0. The corresponding delay duration T_0 is given by

$$T_0 = \Delta_0 4\alpha^2 \frac{H_0}{c} \tag{2.65}$$

When a relative error of ϵ_H is made in the measurement of H_0, i.e.,

$$H = H_0(1 + \epsilon_H), \tag{2.66}$$

the corresponding delay duration becomes

$$T = T_0(1 + \epsilon_T) \tag{2.67}$$

where

$$\epsilon_T = \epsilon_H \tag{2.68}$$

2.4.2 Aircraft Heading

Assuming that the vertical (z-) component of aircraft velocity is zero, the rms width of the Doppler spectrum is given by

$$B_{rms} = 4(\frac{f_0}{c})\alpha v \sin\theta \tag{2.69}$$

where the speed v of the aircraft is given by

$$v = \sqrt{v_x^2 + v_y^2} \tag{2.70}$$

Note that to a first approximation, (i.e., steepest descent approximation) the speed of the aircraft, not the heading, affects Doppler bandwidth.

The received multipath power, however, may be affected by a change in antenna illumination. An error in the aircraft heading can be characterized as an error in the azimuth angle of the antenna beam center. Thus a 5^{o} error in heading would roughly correspond to a little less than an effective 5^{o} reduction in antenna azimuth beamwidth. When the antenna has an azimuth beamwidth of 30^{o}, it is shown in Section 2.5.1.3 that a 5^{o} reduction in this beamwidth results in a 0.25 dB reduction in received multipath power.

2.4.3 Aircraft Speed

From Eq. (2.69) it is evident that a relative error in aircraft speed of ϵ_v corresponds to a relative error in rms Doppler bandwidth of ϵ_B where

$$\epsilon_B = \epsilon_v \tag{2.71}$$

2.4.4 Aircraft Pitch

When the aircraft is flying at a pitch angle of θ_p and a heading of θ_h as shown in Fig. 1, the velocity components are given by

$$v_x = v \cos \theta_p \cos \theta_h \tag{2.72}$$

$$v_y = v \cos \theta_p \sin \theta_h \tag{2.73}$$

$$v_z = v \sin \theta_p \tag{2.74}$$

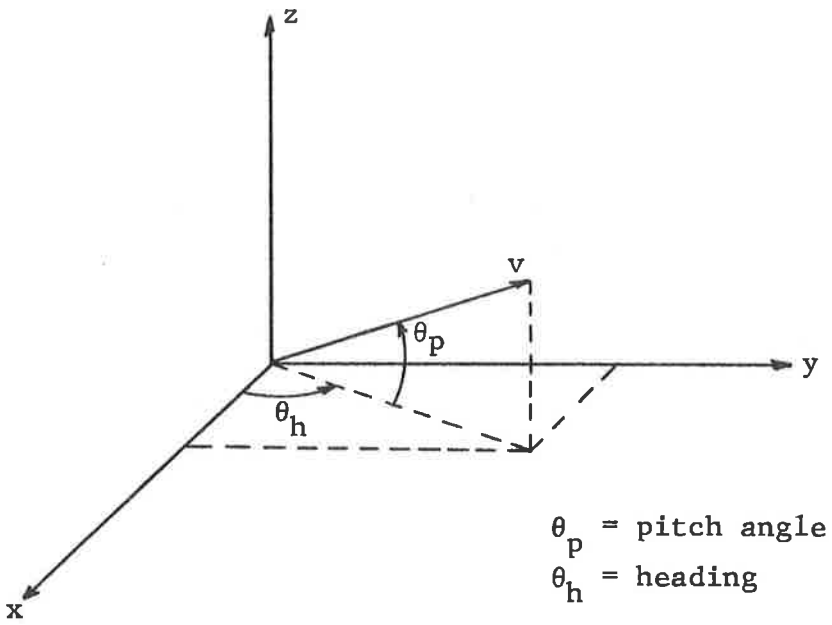

Figure 2.13 Aircraft Velocity

Substituting (2.72) - (2.74) into (2.61) gives the rms Doppler bandwidth in terms of the pitch and heading

$$B_{rms} = 4\left(\frac{f_0}{c}\right)\alpha v \sqrt{\sin^2\theta \cos^2\theta_p + \cos^2\theta \sin^2\theta_p + 2 \sin\theta \cos\theta \cos\theta_p \sin\theta_p \cos\theta_h} \tag{2.75}$$

When the aircraft is in level flight $\theta_p=0$, and the bandwidth is B_0

$$B_0 = 4\left(\frac{f_0}{c}\right)\alpha v \sin\theta \tag{2.76}$$

When the aircraft is pitched at a small angle θ_p, such that $\sin\theta_p \approx \theta_p$, $\cos\theta_p \approx 1$, neglecting terms $0\theta_p^2$ gives

$$B_{rms} \approx 4\left(\frac{f_0}{c}\right)\alpha v \sqrt{\sin^2\theta(1 + 2\theta_p \cos\theta_h/\tan\theta)} \tag{2.77}$$

As long as the pitch angle is much less than the tangent of the grazing angle

$$B_{rms} = B_0(1 + \epsilon_B) \tag{2.78}$$

where

$$\epsilon_B \approx \theta_p \cos\theta_h/\tan\theta \leq \theta_p/\tan\theta \tag{2.79}$$

Thus the error in the rms Doppler bandwidth induced by an error in the pitch angle (measured from level flight) is approximately upper-bounded by the ratio of the pitch angle to the tangent

of the grazing angle. At a 10^{o} grazing angle (tan 10^{o} =0.176) and a pitch angle error of 3^{o} (0.0523 radians), ϵ_B would be about .03. At higher grazing angles, the Doppler bandwidth error becomes less.

2.4.5 Aircraft Roll

When the aircraft rolls, there is a natural tendency for the velocity vector to change direction unless the pilot compensates with a bearing change. The error due to a heading change has been discussed in Section 2.2. Assuming that the aircraft is able to maintain the same course and heading, a roll of the aircraft will not directly affect the duration of the delay psd or the bandwidth of the Doppler psd. However a roll of 3^{o} will reduce the effective elevation angle beamwidth of the antenna by about 3^{o} when the aircraft is flying across the plane containing the satellite, specular point and aircraft.

When the elevation angle beamwidth of the antenna is 68^{o} (centered at an elevation angle of 127^{o}, measured from above to below the aircraft), Section 2.5.1.3 shows that there is a 1 dB loss in multipath power. If the aircraft rolls away from the satellite such that the beam center is at 124^{o}, Fig. 2.21 shows there will be less than 0.3 dB additional multipath loss. However, if the aircraft rolls toward the satellite to a beam center of 130^{o}, the multipath loss could be as much as 2 or 3 dB. To compensate for this potential loss the antenna beamwidth could be increased by 3^{o}, or the beam center moved by 3^{o} to 124^{o}, It should be noted that the calculations of power

loss were made for ideal antennas with a gain of 1 inside and 0 outside the beam. However, since the antenna gain does not change abruptly from 1 to 0 at the beam edge, the multipath power loss will not be as sensitive to aircraft roll as indicated above.

When the aircraft is flying in this plane, it can be shown that the change in azimuth beam center $\Delta\varphi$ is given by

$$\tan \Delta\varphi = \sin \theta_r \tan \theta \tag{2.80}$$

where θ and θ_r are the grazing angle of the ray and the roll angle of the aircraft, respectively. For small roll angles,

$$\Delta\varphi \approx \theta_r \tan \theta \tag{2.81}$$

When the grazing angle is 30^o ($\tan 30^o = .578$) and the roll angle is 3^o, the effective change in azimuth angle beamwidth is 1.73^o. Figure 2.20 shows that this corresponds to less than 0.1 dB of multipath power loss.

2.4.6 RMS Sea Slope

When the rms sea slope is α_0, the duration of the normalized delay psd is Δ_0. The corresponding duration of the delay psd is T_0, where

$$T_0 = \Delta_0 4\alpha_0^2 H/c \tag{2.82}$$

When a relative error of ϵ_α is made in the measurement of α_0, i.e.,

$$\alpha = \alpha_0(1 + \epsilon_\alpha) \tag{2.83}$$

the corresponding delay duration becomes

$$T = T_0(1 + \epsilon_T) \tag{2.84}$$

where

$$\epsilon_T = 2\epsilon_\alpha + \epsilon_\alpha^2 \approx 2\epsilon_\alpha \tag{2.85}$$

In a similar manner, it can be shown that a relative error of ϵ_α in rms sea slope results in a relative error of ϵ_B in rms Doppler bandwidth, where

$$\epsilon_B = \epsilon_\alpha \tag{2.86}$$

Thus an error of 1 percent in rms sea slope would result in an error of 2 percent in delay duration and 1 percent in Doppler bandwidth.

2.5 MULTIPATH CALCULATIONS

This section determines the delay power spectral density (psd), and the frequency correlation function, for the Boeing, omni-directional and various ideal directional antennas. Evaluations are made for an aircraft at a 10 km (32,808 ft.) altitude with specular point grazing angles of 5^o, 10^o, 20^o, and 30^o. The Doppler psd is also computed for 10^o, 20^o, and 30^o grazing angles. The delay-Doppler scattering function is expressed in terms of the scattering cross section of the ocean and the geometric properties of the link, while numerical evaluations are deferred to a later study.

2.5.1 Delay Power Spectral Densities

It was shown in Section 2.2.3 that the total multipath power normalized to the direct path power is given by

$$P = \frac{r_{SA}^2}{4\pi} \iint \frac{\sigma(\theta,\varphi)}{r_1^2 r_2^2} r_0^2 \sin\theta \, d\theta d\varphi \qquad (2.87)$$

where, as shown in Fig. 2.1, r_{SA}, r_1, and r_2 are the slant ranges from satellite to aircraft, satellite to scattering point, and scattering point to aircraft, respectively; r_0 is the mean earth radius (6370 km); and σ is the bistatic scattering cross-section given in Section 2.2.3.

In Section 2.2.1 it was shown that contours of constant delay ξ are superimposed on the (θ,φ) coordinates of the earth's surface. For each value of θ and ξ, a corresponding value of φ is determined, which is shown functionally as

$$\varphi = \varphi(\theta,\xi) \qquad (2.88)$$

Using the change of variable (2.88), Eq. (2.87) can then be written as

$$P = \int Q(\xi) \, d\xi \qquad (2.89)$$

where $Q(\xi)$ is the delay power spectral density (psd) normalized to the direct path power, given by

$$Q(\xi) = \frac{r_{SA}^2}{4\pi} \int \frac{\sigma[\theta,\varphi(\theta,\xi)]}{r_1^2 r_2^2} \frac{\partial\varphi}{\partial\xi} r_0^2 \sin\theta \, d\theta \qquad (2.90)$$

The factor $\partial\varphi/\partial\xi$ represents the Jacobian of the coordinate transformation (2.29) and is computed from Section 2.1. In an analogous manner the delay psd can be written as an integral over the φ coordinate, i.e.,

$$Q(\xi) = \frac{r_{SA}^2}{4\pi} \int \frac{\sigma[\theta(\varphi,\xi),\varphi]}{r_1^2 r_2^2} \frac{\partial\theta}{\partial\xi} r_0^2 \sin\theta(\varphi,\xi)\, d\varphi \qquad (2.91)$$

The factor $\partial\theta/\partial\xi$ represents the Jacobian of the transformation from (θ,φ) to (φ,ξ) coordinates and is also computed from 2.1.

The total psd including the direct path power P_d, the specular component P_{spec},* and $Q(\xi)$ is shown diagrammatically in Fig. 2.14. The scattering cross-section can be written as

$$\sigma(\theta,\varphi) = G_S G_A \sigma^0(\theta,\varphi) \qquad (2.92)$$

where G_S and G_A are the satellite and aircraft antenna gain patterns (normalized to the direct path gain), and σ^0 is the cross-section when omni-directional antennas are used. Since the satellite is so far away from the aircraft and the multipath glistening region, it is assumed that the satellite antenna gain is the same in both directions, i.e.,

$$G_S = 1 \qquad (2.93)$$

Evaluations of delay power spectra when an omni-directional antenna is used are presented in Section 2.3.1.1. Comparisons are made between the omni-directional and the Boeing multipath antennas in Section 2.3.1.2, multipath power calculations are also given, and in Section 2.3.1.3, multipath power loss is computed for ideal directional antennas as a function of beamwidths.

*For grazing angles greater than 10°, the specular component occurs less than 1% of the time at L-band (Reference [2.6], p. 154).

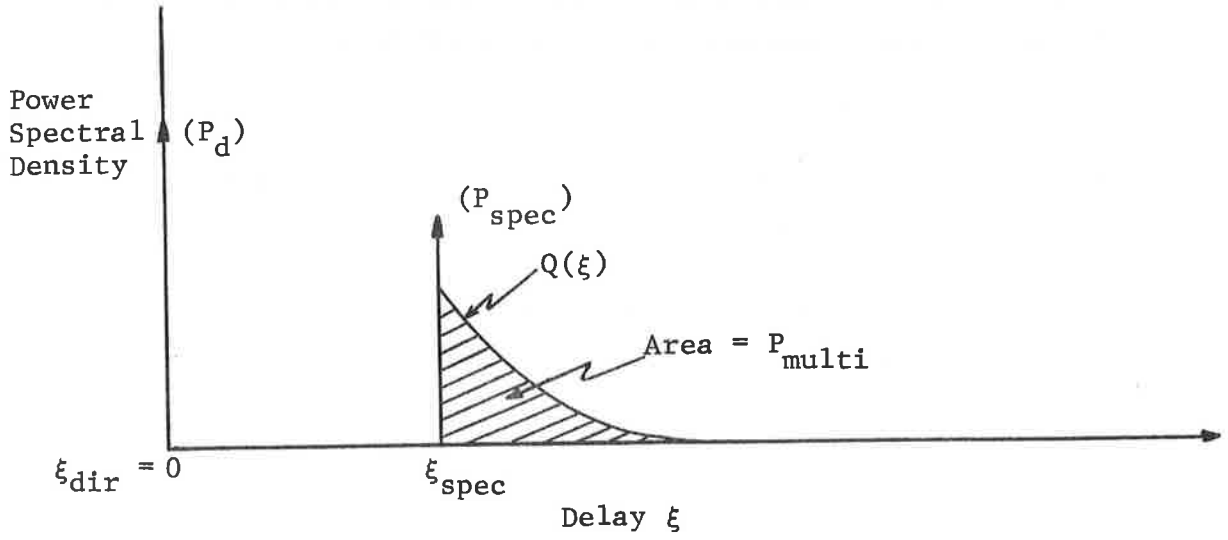

Figure 2.14 Total Power Spectral Density

2.5.1.1 Omni-Directional Antenna

When an omni-directional antenna is used aboard the aircraft, the delay psd is undistorted by the antenna gain and can be computed directly from Eq. (2.90) or (2.91) with $\sigma=\sigma^0$. For each value of delay the integration is performed over the interval $[\theta_1,\theta_2]$, where θ_1 and θ_2 are the values of θ at which the given delay contour crosses the specular point plane of incidence, i.e., $\varphi = \pi/2$. The formalism for calculating these values is given in Appendix B. Since $\frac{\partial\varphi}{\partial\xi}$ goes to infinity at $\varphi = \pi/2$ (see Appendix C), the integrand of Eq. (2.31) is also unbounded at these end points. Therefore in order to evaluate $Q(\xi)$, we must divide the integration interval into two end regions of θ-extent ϵ_1 and ϵ_2, and an interior region of extent $\theta_1-\theta_2-(\epsilon_1+\epsilon_2)$. Then

$$Q(\xi) = \int_{\theta_2}^{\theta_2+\epsilon_2} \delta Q(\xi) + \int_{\theta_2+\epsilon_2}^{\theta_1-\epsilon_1} \delta Q(\xi) + \int_{\theta_1-\epsilon_1}^{\theta_1} \delta Q(\xi)$$

where (2.94)

$$\delta Q(\xi) = \frac{r_{SA}^2}{4\pi} \frac{\sigma^0[\theta,\varphi(\theta,\xi)]}{r_1^2 r_2^2} \frac{\partial\varphi}{\partial\xi} r_0^2 \sin\theta d\theta \qquad (2.95)$$

The numerical integration over the interior region is then done according to Eq. (2.90), while the end region values are obtained according to (2.91), i.e.,

$$\int_{\theta_2}^{\theta_2+\epsilon_2} \delta Q(\xi) = \int_{\varphi=\pi/2}^{\pi/2+\Delta_2\varphi} \delta\hat{Q}(\xi) \qquad (2.96)$$

$$\int_{\theta_1-\epsilon_1}^{\theta_1} \delta Q(\xi) = \int_{\varphi=\pi/2+\Delta_2\varphi}^{\pi/2} \delta\hat{Q}(\xi) \qquad (2.97)$$

where

$$\delta\hat{Q}(\xi) = \frac{r_{SA}^2}{4\pi} \frac{\sigma^0[\theta(\varphi,\xi),\varphi]}{r_1^2 r_2^2} \frac{\partial\theta}{\partial\xi} r_0^2 \sin\theta(\varphi,\xi)\, d\varphi \qquad (2.98)$$

and $\Delta_1\varphi$, $\Delta_2\varphi$ are the φ-intervals corresponding to ϵ_1, ϵ_2. The integration over each region is performed using Simpson's rule, and the values of φ for the mid-region integration and θ for the end region integrations are computed using the Fortran scientific subroutine RTMI (see Appendix A).

In order to compare various psd's on the same basis, each has been normalized to its value at the specular point. It is shown in Appendix C that this value is given by

$$Q(\xi_{spec}) = \frac{c}{r_0} \frac{R_{SA}^2}{4\pi} \frac{2\sigma(\theta_{spec}, \pi/2)}{R_1^2 R_2^2} \sqrt{\frac{2\sin\theta_{spec}}{A_1(A_2-A_3)}} \qquad (2.99)$$

where

$$A_1 = \frac{P_2}{R_2} \sin\theta_A \qquad (2.100)$$

$$A_2 = \frac{P_1}{R_1} \cos\theta_{spec} + \frac{P_2}{R_2} \cos(\theta_A-\theta_{spec}) \qquad (2.101)$$

$$A_3 = \frac{P_1^2}{R_1^3} \sin^2\theta_{spec} + \frac{P_2^2}{R_1^3} \sin^2(\theta_A-\theta_{spec}) \qquad (2.102)$$

The delay psd $Q(\xi)$ normalized to its value at the specular point delay ξ_{spec} is shown in Fig. 2.15 for horizontal, vertical and (opposite-sense) circular polarization. The sense of circular polarization in the receiver is referenced to the direct path. Since there is a tendency for the sense of the circular polarization to reverse upon reflection from the ocean, a receiving antenna which has (opposite-sense) circular polarization captures more multipath power than one which has (same-sense) circular polarization. The grazing angle is 10^{o} and the rms sea slope is 0.2. Similar curves can be generated for 20^{o} and 30^{o} grazing angles. A comparison of 10^{o}, 20^{o}, and 30^{o} for (opposite-sense) circular polarization is shown in Fig. 2.16. The total multipath power normalized to the direct path power is computed numerically as the area under each of these curves (multiplied by the specular point value), and the results are presented in Table 2-9.

In Fig. 2.17 the normalized delay psd for (opposite-sense) circular polarization is compared to the steepest descent calculation [2.5] at a 10^{o} grazing angle. It is seen that the steepest descent calculation becomes less accurate at larger delay values as would be expected. The total multipath power normalized to the direct path power is -12.5 dB. Note that this constitutes a 7.8 dB reduction in multipath from the case in which the transmitter and receiver have opposite sense polarizations.

2.5.1.2 Boeing (ATS-5) Multipath Antenna

When the Boeing (ATS-5) multipath antenna* is used instead of an omni-directional antenna, the scattering cross-section becomes

$$\sigma(\theta,\varphi) = G(\theta,\varphi)\sigma^{0}(\theta,\varphi) \qquad (2.103)$$

where G is the antenna gain pattern evaluated at the scattering point, and σ^{0} is the scattering cross-section for the omni.

*The Boeing (ATS-5) multipath antenna to which we refer is the one used in the ATS-5 flight tests [2.7].

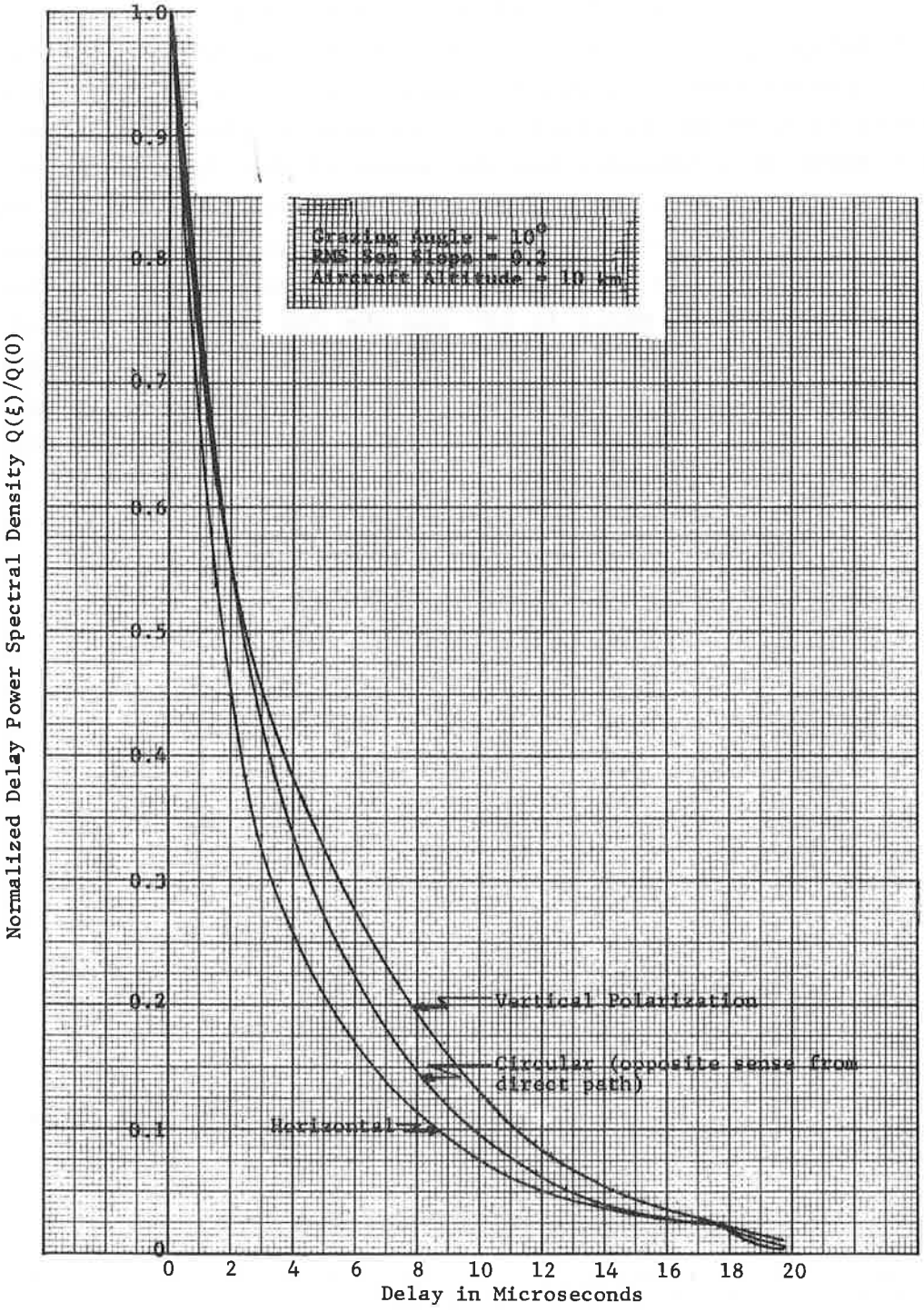

Figure 2.15 Comparison of Delay Power Spectral Densities for Omni-Directional Antennas with Horizontal, Vertical and Circular Polarizations

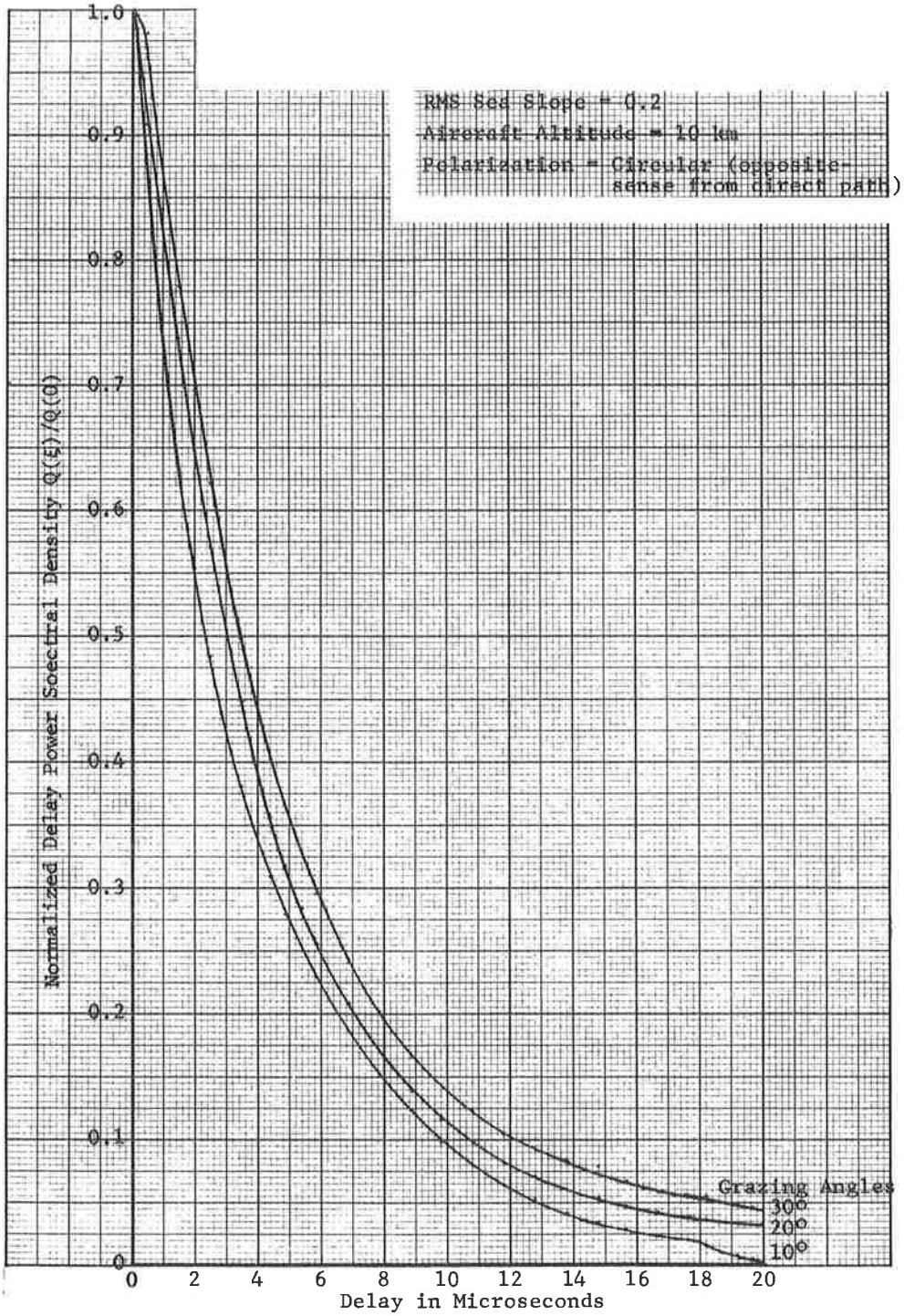

Figure 2.16 Comparison of Delay Power Spectral Densities for Omni-Directional Antennas at 10°, 20°, and 30° Grazing Angles

Table 2-9

MULTIPATH POWER WITH AN OMNI-DIRECTIONAL ANTENNA

Grazing Angle Degrees	Multipath Power w/r to P_{direct} in dB			
	Horizontal	Vertical	Circular (Opposite-Sense)	Circular (Same-Sense)
5	—	—	-7.5	—
10	-2.7	-8.3	-4.7	-12.5
20	-0.8	-4.2	-2.5	-13.6
30	-0.1	-2.0	-1.6	—

Aircraft Altitude = 10 km

RMS Sea Slope = 0.2

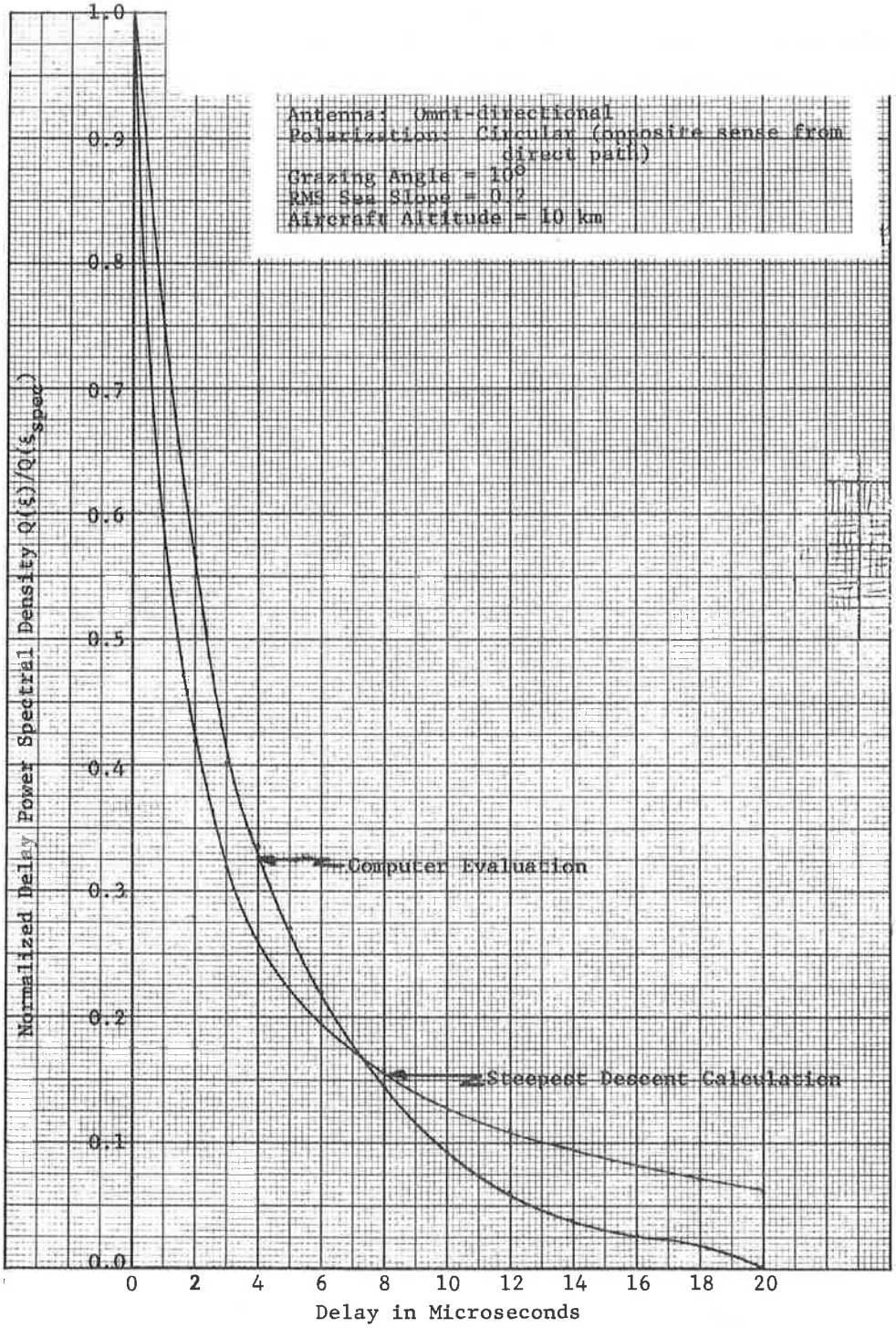

Figure 2.17 Comparison of Delay Power Spectral Density with Steepest Descent Calculation

Since the maximum gain of the antenna occurs 15^{o} down and 7^{o} aft of the aircraft, the antenna will not necessarily be "pointing at" the specular point. The heading of the aircraft is described by α which is the angle between the velocity vector and a perpendicular to the plane of S, A and the specular point (see Fig. 2.5). Thus when α is 7^{o} (assuming level flight), the antenna is pointing in the azimuthal plane of the specular point at an elevation angle of $(90^{o} + 15^{o} =) 105^{o}$. When $\alpha = 0^{o}$, the antenna is 7^{o} in azimuth away from the specular point. The delaypsd for (opposite sense) (circular) polarization is shown in Fig. 2.18 for a 10^{o} grazing angle (the psd using an omni is shown for comparison).

Presented in Table 2-10 is the loss in multipath power (normalized to P_d) due to antenna discrimination. This loss in dB is determined from

$$L = P_{multi}^{omni} - P_{multi} \qquad (2.104)$$

where P_{multi}^{omni} is the multipath power for an omni-directional antenna (see Table 2-9), and P_{multi} is the multipath power when the Boeing antenna (normalized to unity gain) is used. Each of these is normalized to the power in the direct path which is assumed to be received by an omni-directional, unity-gain antenna.

It is clear from Fig. 2.18 and Table 2-9, that the effects of the Boeing multipath antenna on measurement of the delay psd are as follows:

1) More than 4 dB of multipath power is lost due to antenna discrimination
2) The tails of the delay psd are attenuated from that provided by an omni-directional antenna.

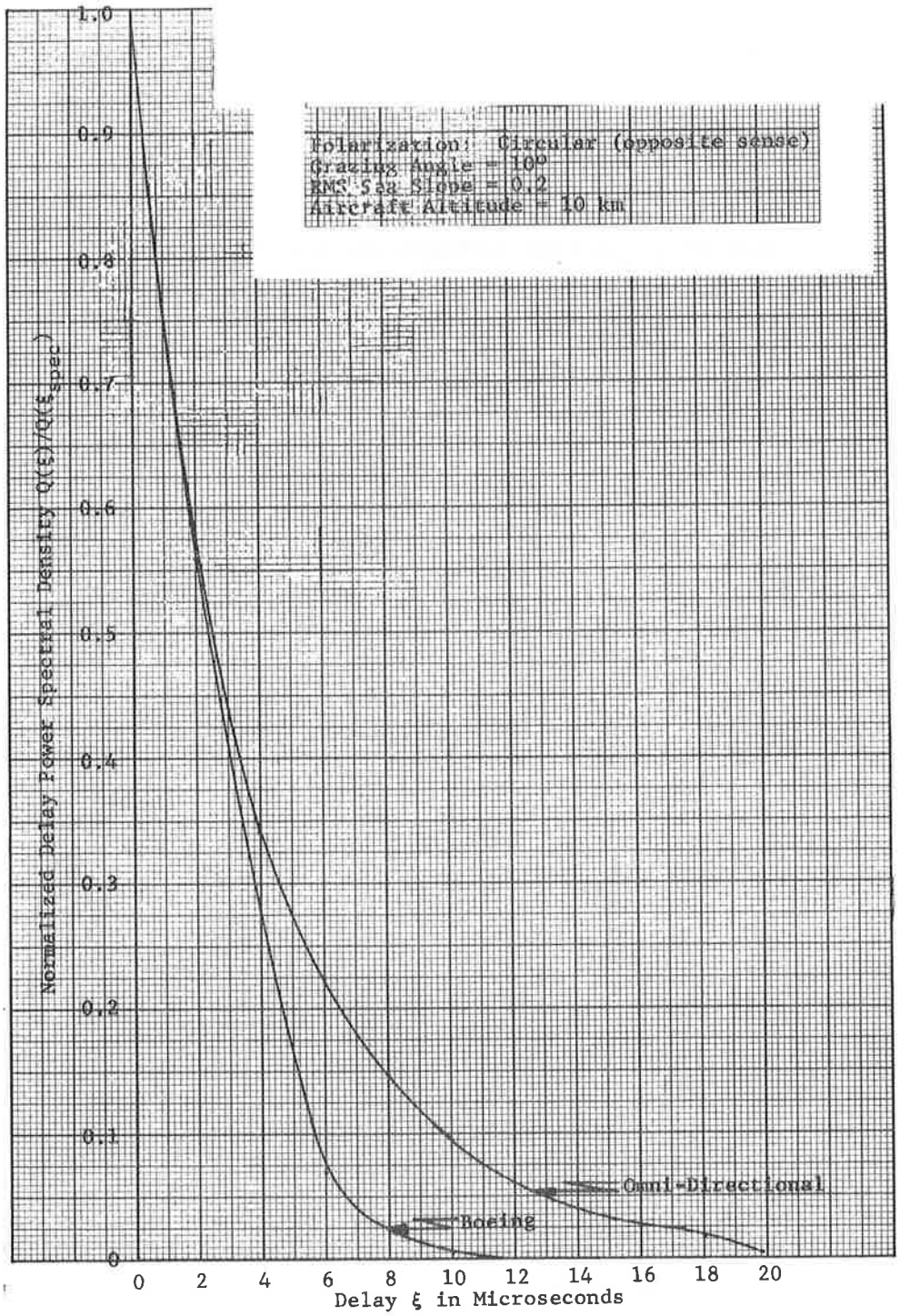

Figure 2.18 Comparison of Delay Power Spectral Densities of Omni-Directional and Boeing (ATS-5 Multipath) Antenna

Table 2-10

EFFECT OF BOEING ANTENNA ON MULTIPATH RATIO AT 10^{o}, 20^{o} AND 30^{o} GRAZING ANGLES

Grazing Angle Degrees	Multipath Power dB Above P_{direct}		Multipath Power Loss L dB
	Omni	Boeing (ATS-5)	
10	-4.7	-8.7	4.0
20	-2.5	-7.1	4.6
30	-1.6	-7.0	5.4

Polarization = circular (opposite sense from direct path)
RMS sea slope = 0.2
Aircraft altitude = 10 km

The loss in multipath power in the tails of the delay psd causes the frequency correlation function to become flatter near the origin. The frequency correlation function is given by the Fourier transform of the delay psd. This was computed numerically using an FFT algorithm, and the results are shown in Fig. 2.19 for both an omni-directional antenna and the Boeing antenna. It will be shown in Section 2.6 that this in turn makes the performance of a ranging system appear to be better than it actually is (using an omni-directional antenna). Detailed calculations of the change in performance due to the Boeing antenna are presented in 2.6.

2.5.1.3 Ideal Directional Antenna

In order to specify the approximate characteristics of a multipath antenna, the delay psd and multipath power loss has been determined as a function of elevation and azimuth angle beamwidths. The antenna is assumed to be ideal in the sense that the gain is unity inside and zero outside the beamwidth. Since the actual candidate antennas will have smooth variations in the gain pattern, the beamwidths derived in this section should be used only as indications of approximate design goals. The antenna patterns for specific operational antennas (which have these approximate beamwidths) can then be incorporated into the analysis of 2.5.1 to yield specific delay spectra and multipath loss calculations. Likewise performance calculations can also be made according to the methods outlined in Section 2.6.

Assuming that the aircraft is in level flight on a bearing which is perpendicular to the specular point incident plane, the elevation angle θ^A is measured from above to below the aircraft, and the azimuth angle φ^A is measured from the nose toward the tail. The first ideal antenna to be considered is one for which

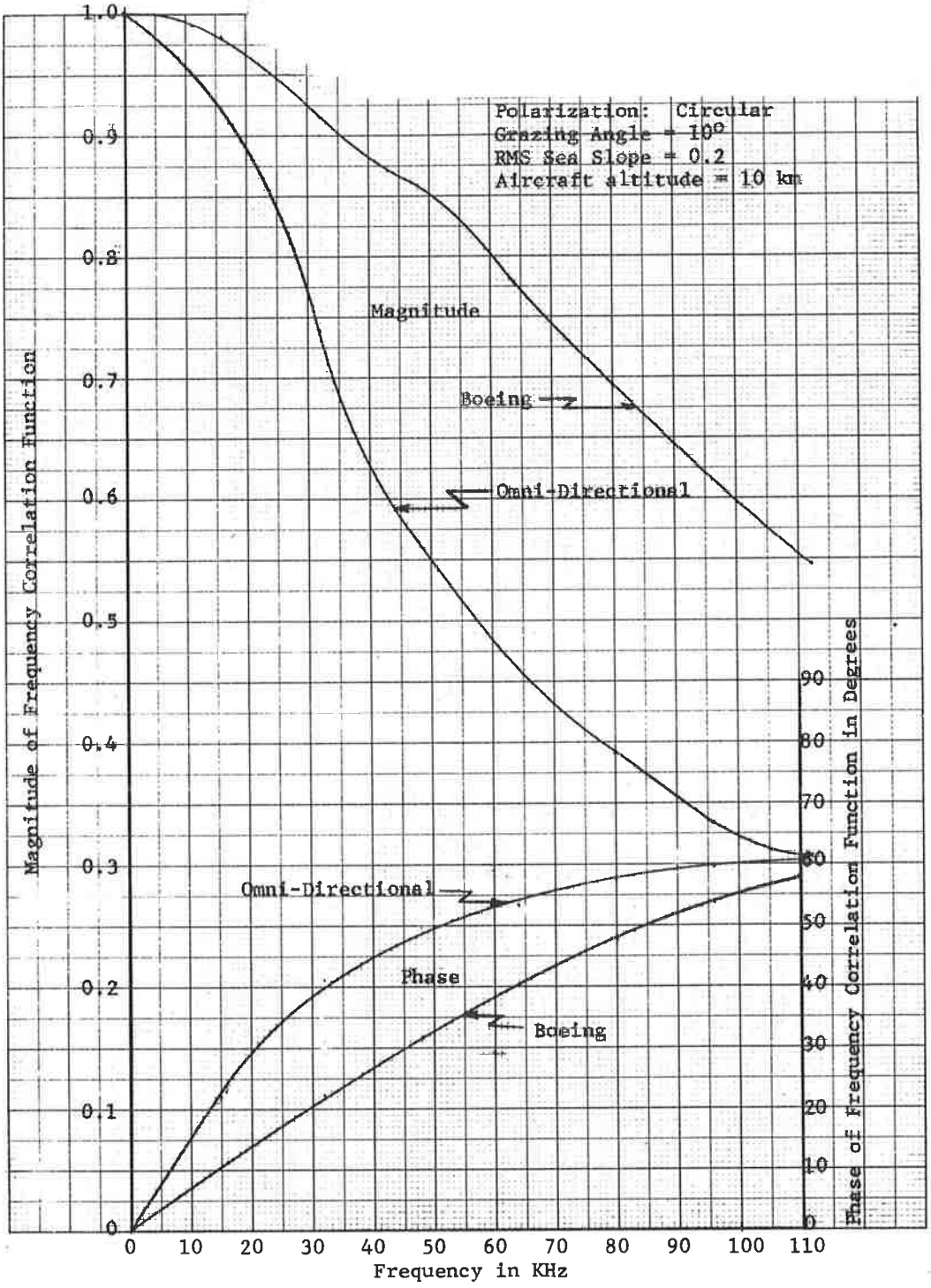

Figure 2.19 Comparison of Frequency Correlation Functions of Omni-Directional and Boeing Antennas

The elevation angle beamwidth is 180^{o} and the azimuth angle beamwidth is variable. In Fig. 2.20 the multipath power loss is shown as a function of azimuth angle beamwidth. It is assumed that the center of the beam is at the specular point incident plane, i.e., the plane containing the satellite, specular point, and aircraft. This is the obvious choice of azimuth position. Since it would be desirable to measure Doppler psd while flying in this plane as well as across this plane, the antenna should rotate 90^{o} in azimuth. From Fig. 2.20 it is seen, for example, that to obtain a multipath power loss of less than 1 dB, an azimuth beamwidth of greater than 16^{o} is needed at a 10^{o} grazing angle, while at a 30^{o} grazing angle a 29^{o} beamwidth is required.

The next ideal antenna to be considered is one for which the azimuth angle beamwidth illuminates only the region bounded by the cut-off delay contour, and the elevation angle beamwidth is variable. Thus if the cut-off delay is 10 μsec, the antenna is assumed to illuminate that region of the surface within a 10 μsec contour (see Fig. 2.6). Since it is not obvious in which elevation plane the antenna should point, the analysis has been done with sufficient generality to present a range of possibilities to the antenna designer. In Fig. 2.21a the multipath power loss is plotted as a function of cut-off delay and in Fig. 2.21b, the range of elevation angles which this cut-off delay contour subtends is indicated. Values are obtained from 2.8 - 2.10.

The variety of design possibilities can best be indicated by example. Assuming a multipath loss of 1 dB is allowable, then from curve (2.21a) at a 10^{o} grazing angle points on the scattering surface with delays of 7.5 μsec (and less) must be illuminated by the antenna. From curve (2.21b), it is seen that these points

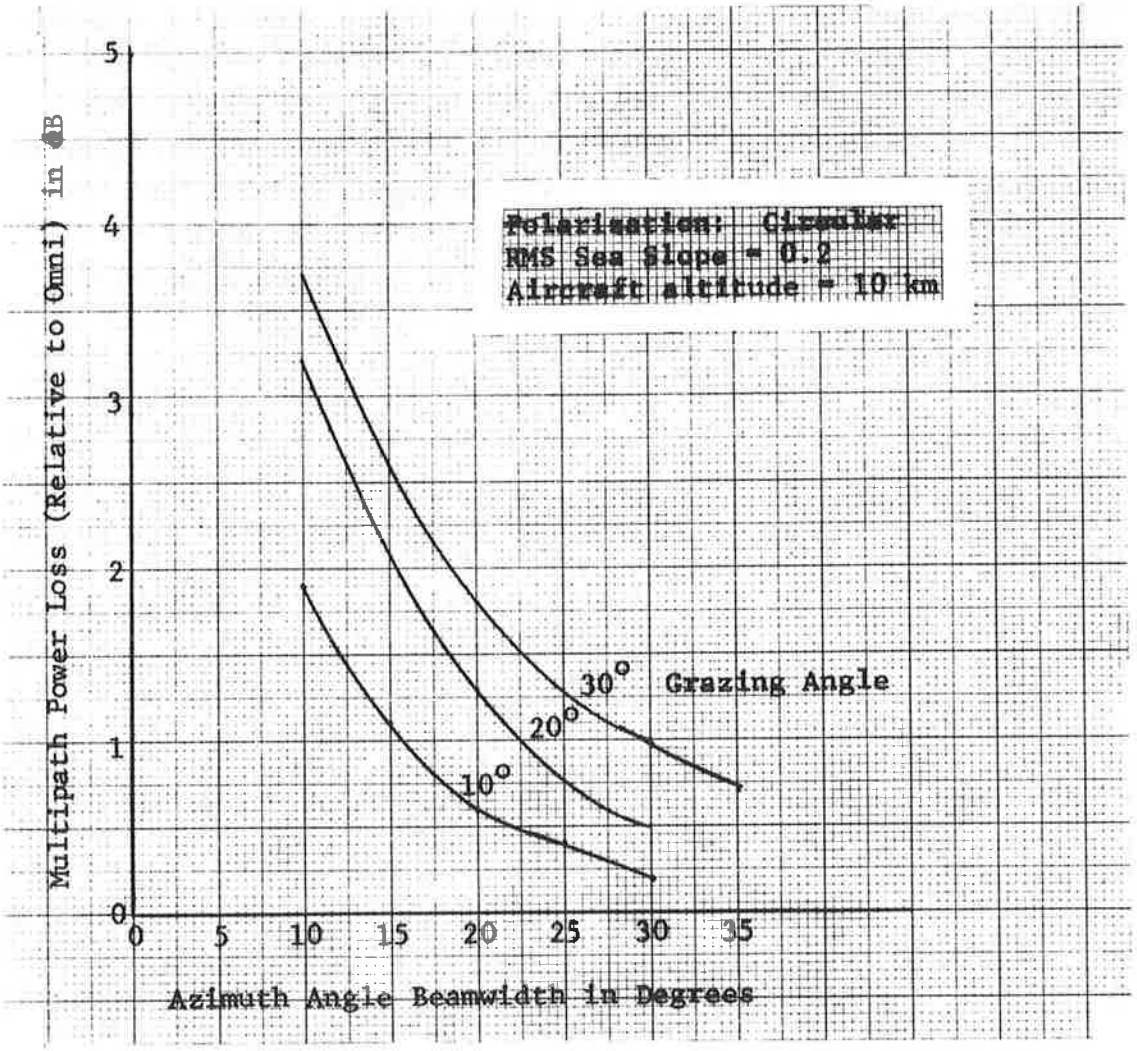

Figure 2.20 Multipath Power Loss Vs. Azimuth Angle Beamwidth

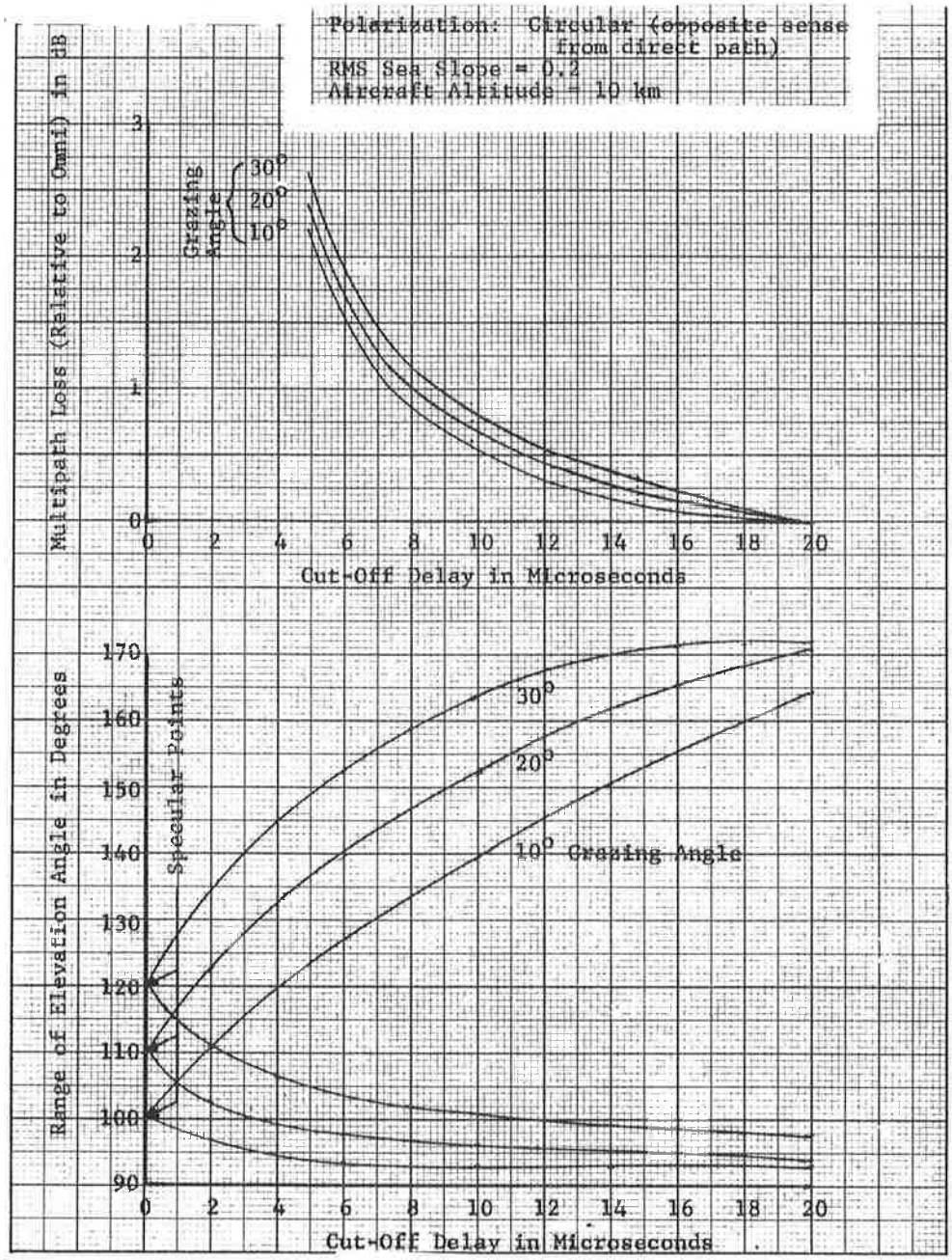

Figure 2.21 a. Multipath Power Loss Vs. Cut-Off Delay
b. Range of Elevation Angle Vs. Delay

lie in elevation angle from 94° to 132°, i.e., an elevation beamwidth of 38° centered at an elevation angle of 113°. The 1 dB criterion applied to the 30° grazing angle case gives a 60° beamwidth centered at 132° (from 101° to 161°). Thus the antenna may be designed to step from 113° to 132° with a 60° beamwidth. Alternatively, if the antenna is to be stationary, it will illuminate from 93° to 161°, i.e., a beamwidth of 68° centered at 127°. Trade-offs between antenna beamwidths (and therefore antenna gain) and multipath power loss may be made as required by antenna design considerations. The relationship between multipath loss and ranging performance is given in Section 2.6.

2.5.2 Doppler Power Spectral Density

In a manner similar to that outlined for the delav psd, contours of constant Doppler ν are superimposed on the (θ,ψ) coordinates of the earth's surface. For each value of θ and ν, a corresponding value of φ can be determined, which is shown functionally as

$$\varphi = \varphi(\theta,\nu) \tag{2.105}$$

Using the change of variable (2.105), Eq. (2.21) can be written as

$$P = \int P(\nu)\, d\nu \tag{2.106}$$

where $P(\nu)$ is the Doppler psd normalized to the direct path power, given by

$$P(\nu) = \frac{r_{TR}^2}{4\pi} \int \frac{\sigma[\theta,\varphi(\theta,\nu)]}{r_1^2 r_2^2} \frac{\partial\varphi}{\partial\nu} \sin d\theta \tag{2.107}$$

Calculations have been made of the cross-plane* Doppler psd for an omni-directional antenna at an altitude of 10 km with an rms sea slope of 0.2. The results are displayed for (opposite-sense) circular polarization at 10^{o}, 20^{o}, and 30^{o} grazing angles in Figs. 2.22, 2.23, and 2.24. These correspond to the Doppler contours displayed in Fig. 2.4 and 2.5 of Section 2.2.1. Tables of the Doppler psd, for horizontal, vertical, (opposite-sense) circular, and (same-sense) circular polarizations are presented in Appendix F.

Calculations for an in-plane flight would be performed in exactly the same manner. The Doppler contours on the ocean surface would be identical to those of the cross-plane flight except that they would be rotated 90^{o}.

*A cross-plane flight is defined as one in which the aircraft is traveling in a line perpendicular to the plane of the satellite, aircraft and specular point. A flight which is perpendicular to the cross-plane is an in-plane flight.

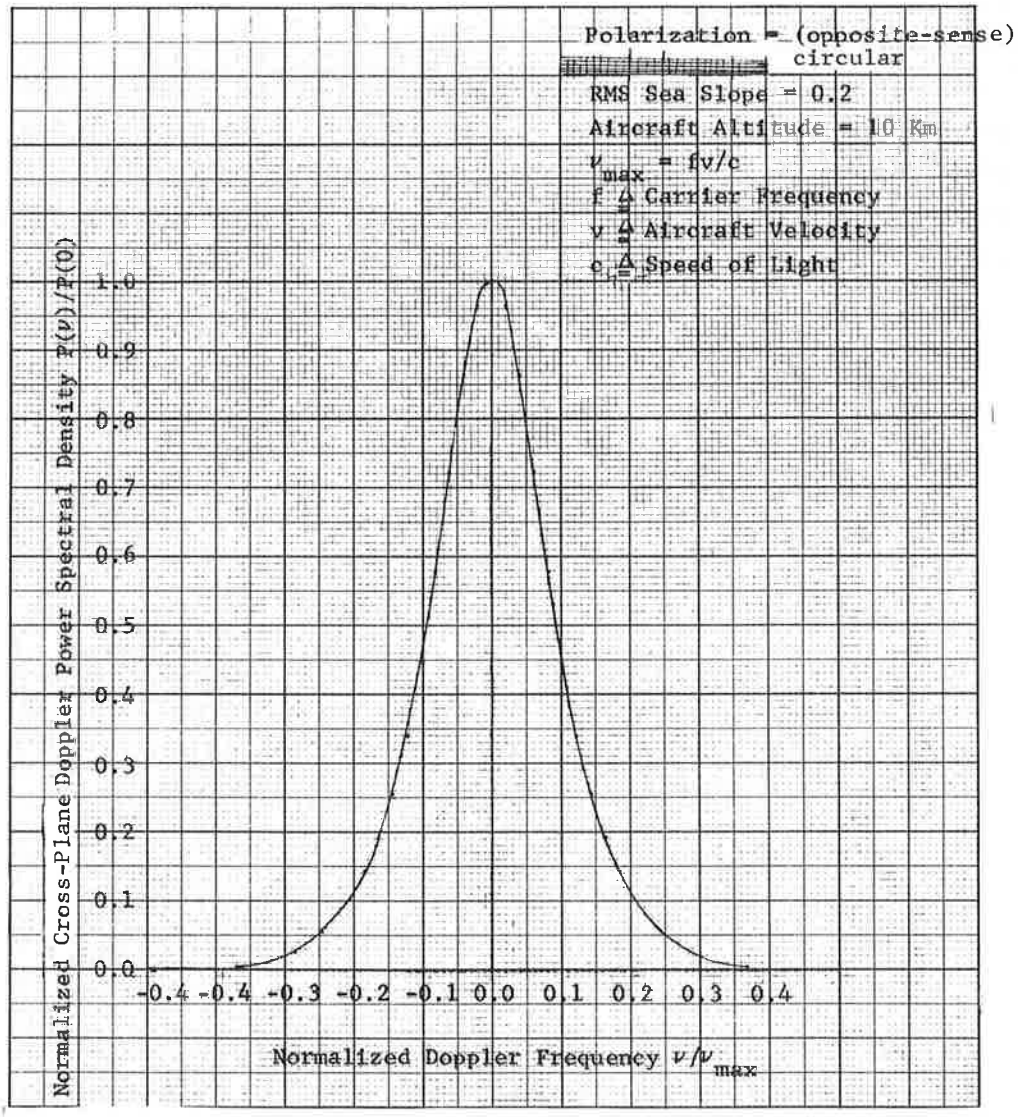

Figure 2.22 Doppler Power Spectral Density for an Omni-Directional Antenna at 10^{o} Grazing Angle

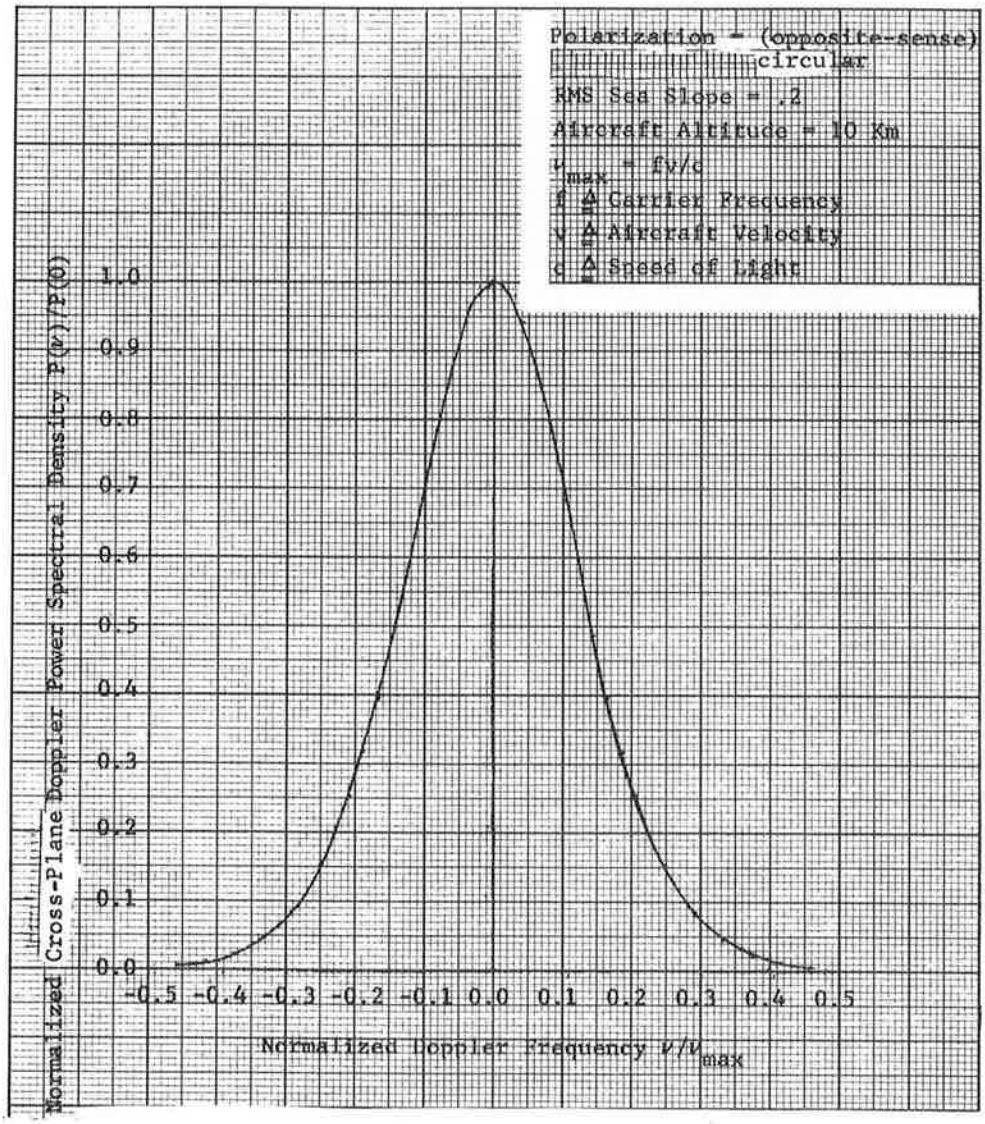

Figure 2.23 Doppler Power Spectral Density for an Omni-Directional Antenna at 20° Grazing Angle

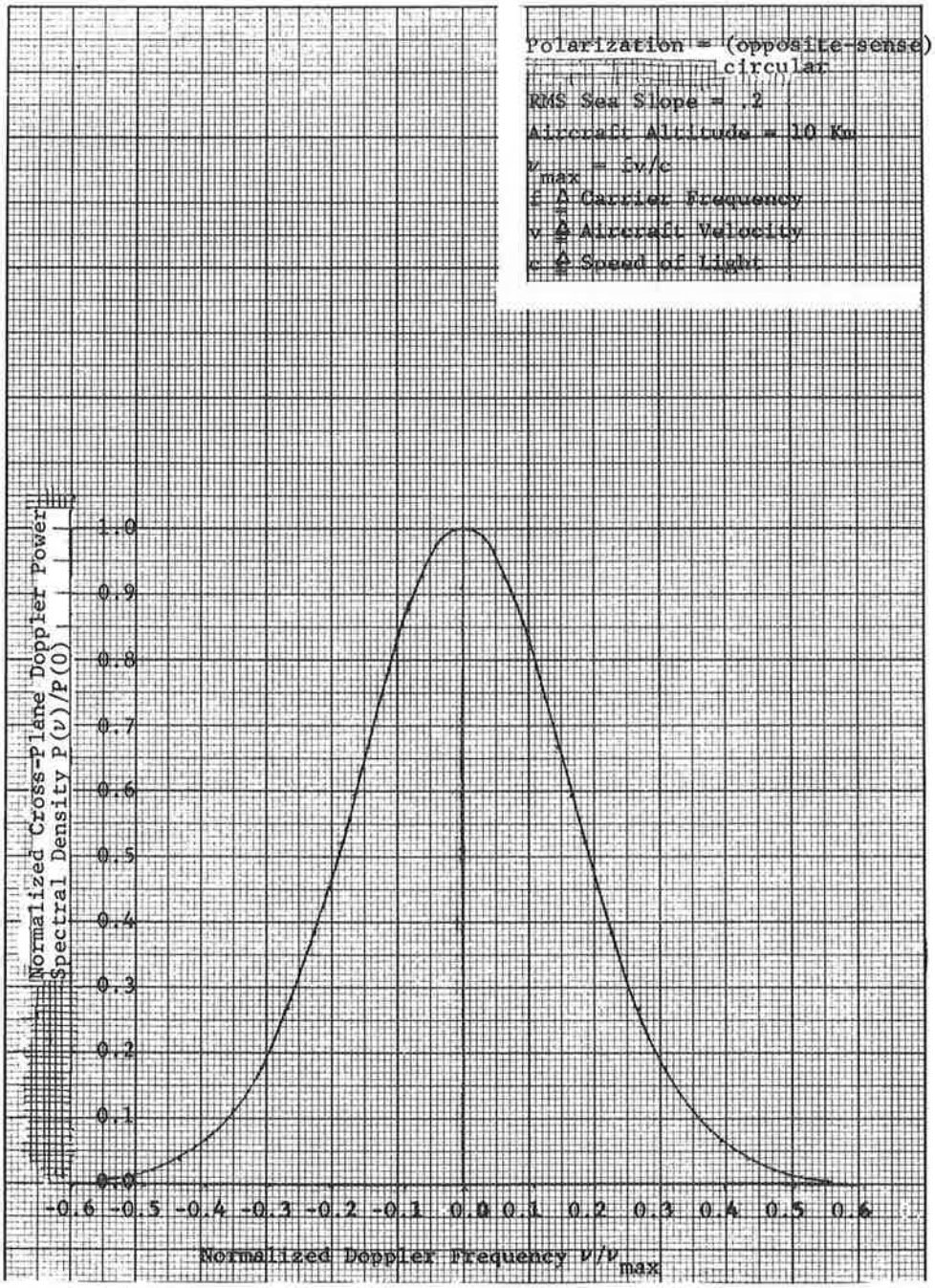

Figure 2.24 Doppler Power Spectral Density for an Omni-Directional Antenna at 30^{o} Grazing Angle

2.5.3 Delay Doppler Scattering Function

The delay Doppler scattering function is computed using a two-dimensional coordinate transformation from the (θ,φ) coordinates of the surface to the delay-Doppler (ξ,ν) coordinates induced upon the surface by the aircraft location and velocity, i.e.,

$$\theta = \theta(\xi,\nu) \tag{2.108}$$

$$\varphi = \varphi(\xi,\nu) \tag{2.109}$$

By superimposing the corresponding delay and Doppler contours shown in Section 2.2.1, it becomes apparent that this transformation is double valued, (i.e., there are two (θ,φ) points which map to the same (ξ,ν) point). When the aircraft heading is in-plane, the two (θ,φ) points corresponding to a given (ξ,ν) intersection are symmetrically located to either side of the specular point plane. The scattering cross-sections will therefore be the same at each of these points. However, when the aircraft heading is cross-plane, the points are not symmetrically located, and the scattering cross-sections are different. In general, the coordinate transformation must be performed separately in each of the two single valued regions. Under this coordinate transformation Eq. (2.21) becomes

$$P = \iint S(\xi,\nu)\, d\xi\, d\nu \tag{2.110}$$

where $S(\xi,\nu)$ is the delay-Doppler scattering function given by

$$S(\xi,\nu) = \frac{r_{SA}^2}{4\pi} \sum_{2 \text{ regions}} \frac{\sigma[\theta(\xi,\nu)\varphi(\xi,\nu)]}{r_1^2 r_2^2} J\, r_0^2 \sin\theta \tag{2.111}$$

The summation is performed over each of the single valued regions, and J is the Jacobian of the coordinate transformation (2.108) and (2.109). Since this transformation is double-valued, measurement of $S(\xi,\nu)$ does not generally constitute measurement of σ. Two special cases in which σ can be recovered from $S(\xi,\nu)$ are as follows:

1) When the aircraft is flying in the plane of the satellite, the specular point and the earth's center, the two terms in (2.111) are identical, and the sum can be replaced by two times either term.

2) When the antenna discriminates against either region, only one term in the sum (2.111) contributes to $S(\xi,\nu)$.

Special case 1) above is easily achieved during flight test by flying the aircraft toward the satellite while utilizing an antenna with a gain pattern which is symmetric to either side of the aircraft. Special case 2) is not easily achieved without sophisticated antenna design and is therefore probably not practical in a flight test. It is therefore recommended that in-plane flights be made using an antenna which is symmetric in azimuth.

Calculations of the delay-Doppler scattering function can then be made according to Eq. (2.111). It would of course be desirable to use an antenna with a wide enough beamwidth to capture the significant multipath power (see Table 2-1). In the event that the antenna attenuates the power in any given delay-Doppler interval, accurate knowledge of the antenna gain pattern at that point would be required to recover the correct value of scattering cross-section.

2.6 TONE RANGING PERFORMANCE

The variance in the estimate of (one-way) delay by a single-sideband tone ranging system has been shown [2.2] to be given by

$$\sigma_f^2 = \frac{1}{(2\pi\Omega)^2}\left[\frac{W_N}{\gamma B_N}\left(1 - \mathrm{Re}\ (r_{13})\right) + \frac{1}{S}\right] \qquad (2.112)$$

where Ω is the frequency separation of the tones, γ is the ratio of direct-to-multipath power, W_N and B_N are the two-sided noise bandwidths of the tone filter and Doppler spectrum, respectively, and S is the signal-to-noise ratio. The term r_{13} is given by

$$r_{13} = q(\Omega)\ \exp\left[-j2\pi\Omega(\xi_{spec} - \xi_d)\right] \qquad (2.113)$$

where $q(\Omega)$ is the (normalized) frequency correlation function, ξ_{spec} is the specular point delay and ξ_d is the direct path delay.

Assuming that $W_N = B_N$ and $S \gg 1$, the (one-way) rms ranging error has been computed for the Boeing and omni-directional antennas at 10°, 20°, and 30° grazing angles for an aircraft altitude of 10 km. The results are summarized in Table 2-11 for circular polarization with a tone frequency separation of 16 KHz and an rms sea slope of 0.2. The relative error in the estimate of rms ranging error σ is defined as

$$\epsilon = (\sigma_{omni} - \sigma)/\sigma_{omni} \qquad (2.114)$$

where σ_{omni} is the true rms error. Defining σ_γ and σ_q as the values of σ when only γ or only $q(\Omega)$ has been changed from its omni-directional values, i.e.,

Table 2-11

RANGING ERRORS FOR OMNI-DIRECTIONAL AND BOEING ANTENNAS.
RMS SEA SLOPE = 0.2, TONE FREQUENCY SEPARATION = 16 KHz, POLARIZATION = CIRCULAR
(Aircraft Altitude = 10 km)

Grazing Angle Degrees	γ_{omni} dB	σ_{omni} Ft.	γ_{Boeing} dB	σ_{Boeing} Ft.	Attenuation Relative Error ϵ_γ	Correlation Relative Error ϵ_q	Relative Error ϵ
10	4.7	301.1	8.7	219.8	0.369	-0.16	0.27
20	2.5	765.4	7.1	497.5	0.411	-0.10	0.35
30	1.6	1033.5	7.0	547.8	0.475	-0.010	0.47

γ = direct path power/multipath power

σ = rms ranging error

$\epsilon = (\sigma_{omni} - \sigma_{Boeing})/\sigma_{omni}$ = relative error

ϵ_γ = relative error due to change in γ only

ϵ_q = relative error due to change in frequency correlation only

$$\sigma_{\gamma}^2 = \frac{1}{(2\pi\Omega)^2} \frac{[1 - \mathrm{Re}\ (r_{13_{omni}})]}{\gamma} \tag{2.115}$$

and

$$\sigma_{q}^2 = \frac{1}{(2\pi\Omega)^2} \frac{[1 - \mathrm{Re}\ (r_{13})]}{\gamma_{omni}} \tag{2.116}$$

then the relative errors in the estimates of σ_{omni} when γ and q have been separately corrected is

$$\epsilon_{\gamma} = (\sigma_{omni} - \sigma_{\gamma})/\sigma_{omni} \tag{2.117}$$

$$\epsilon_{q} = (\sigma_{omni} - \sigma_{q})/\sigma_{omni} \tag{2.118}$$

where

$$\sigma_{omni}^2 = \frac{1}{(2\pi\Omega)^2} \frac{[1 - \mathrm{Re}\ (r_{13_{omni}})]}{\gamma_{omni}} \tag{2.119}$$

Substituting (2.115), (2.116) and (2.119) into (2.117) and (2.118) gives

$$\epsilon_{\gamma} = 1 - \sqrt{\gamma_{omni}/\gamma} \tag{2.120}$$

and

$$\epsilon_{q} = 1 - \sqrt{\frac{1 - \mathrm{Re}\ (r_{13})}{1 - \mathrm{Re}\ (r_{13_{omni}})}} = 1 - \frac{\sigma}{\sigma_{omni}} \sqrt{\frac{\gamma}{\gamma_{omni}}} \tag{2.121}$$

Note from Table 2-11, that if the loss in multipath power due to antenna discrimination is accounted for, the relative error due to the decorrelation is still as much as 16%. Decorrelation tends to increase range error while multipath power loss tends to decrease it.

When an ideal directive antenna (with a gain of 1 inside and 0 outside the beamwidth) is used, the apparent rms ranging error varies with antenna beamwidth. Corresponding to the curves in Fig. 2.20 of multipath loss versus azimuth beamwidth, Fig. 2.25 presents the corresponding rms range error versus azimuth beamwidth. Likewise, if the antenna only illuminates points on the surface within a certain delay contour (called the cut-off delay), the rms ranging error is as shown in Fig. 2.26 corresponding to the multipath losses and elevation angle beamwidths previously shown in Fig. 2.21.

For example, from Fig. 2.25 it is seen that an azimuth angle beamwidth of 30^{o} gives an apparent rms range error equal to 100% of its omni-directional value at a 10^{o} grazing angle, 95% at a 20^{o} grazing angle, and 90% at a 30^{o} grazing angle. From Fig. 2.20 it is seen that this beamwidth corresponds to a maximum multipath loss of 1 dB (at 30^{o} grazing angle). Likewise, a cut-off delay of 8.8 μsec yields rms ranging errors of 99%, 95% and 89% of the omni-directional values at 10^{o}, 20^{o}, and 30^{o}, respectively. From Fig. 2.21 this also corresponds to a maximum multipath loss of 1 dB using a 68^{o} elevation angle beamwidth centered at 127^{o} (measured from above the aircraft).

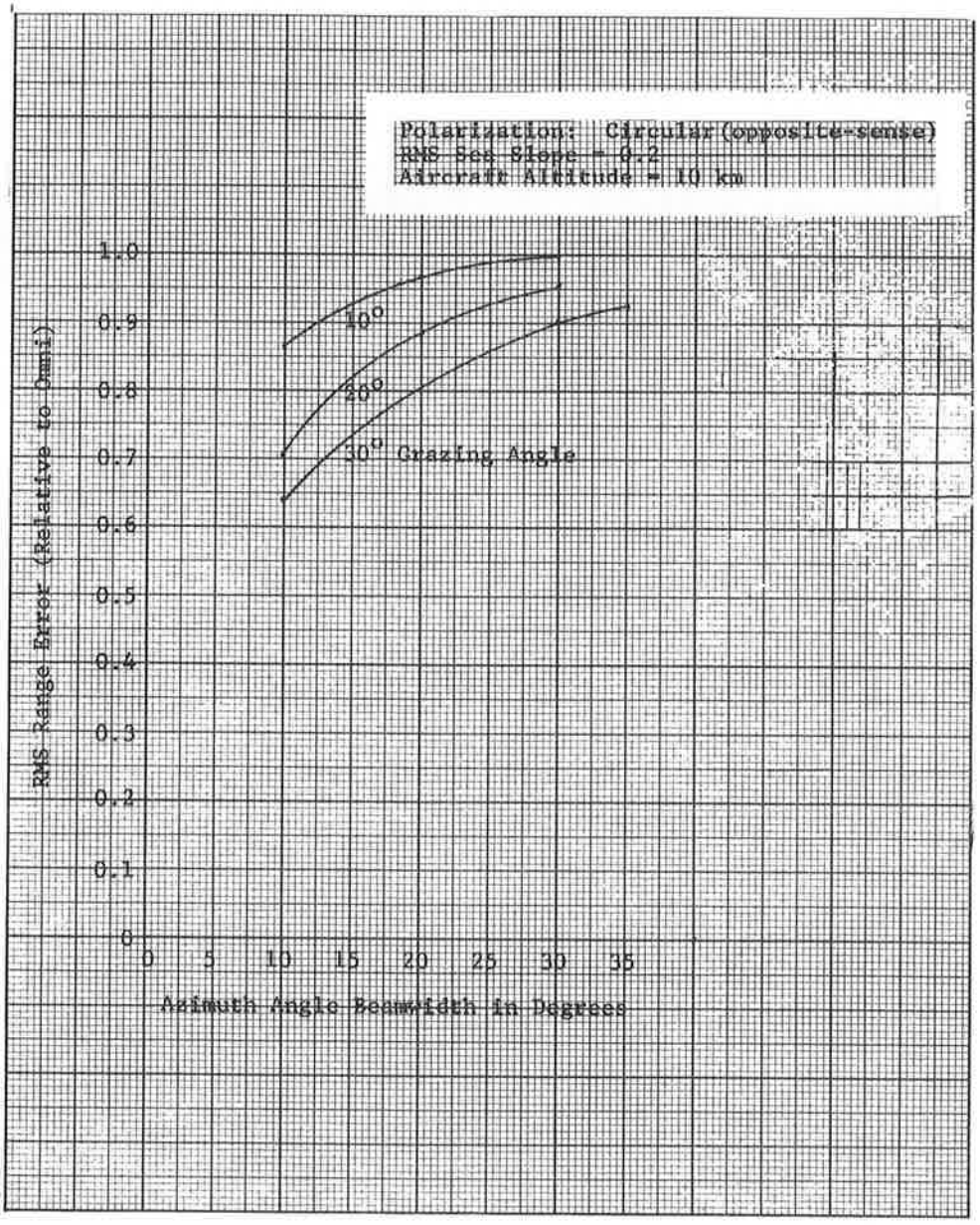

Figure 2.25 RMS Range Error Vs. Azimuth Angle Beamwidth

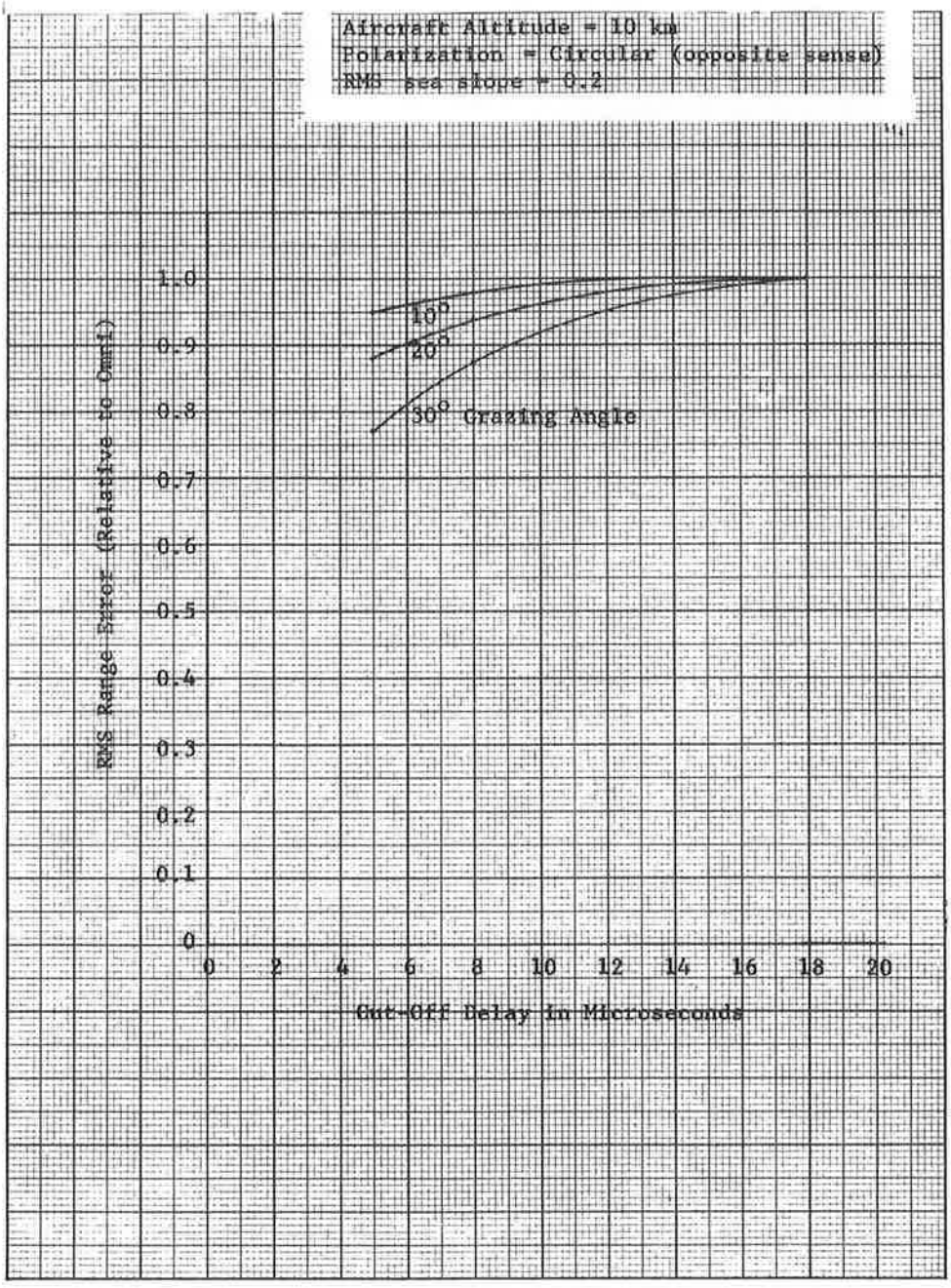

Figure 2.26 RMS Range Error Vs. Cut-Off Delay

REFERENCES

2.1 J. K. DeRosa, "The Characterization of Multipath and Doppler Fading in Earth Scatter Communication, Navigtion and Radar Links," Ph.D. Dissertation, Northeastern University, Boston, Massachusetts, June 1972.

2.2 P. A. Bello and C. J. Boardman, "Effect of Multipath on Ranging Error for an Airplane-Satellite Link," IEEE Trans. on Communication, Vol. COM-21, No. 5, May 1973, pp. 564-576.

2.3 R. W. P. King, Fundamental Electromagnetic Theory, Dover Publications, New York, 1963, p. 525.

2.4 P. Beckmann and A. Spizzichino, The Scattering of Electromagnetic Waves from Rough Surfaces, New York, Pergamon, 1963.

2.5 P. A. Bello, "Aeronautical Channel Characterization," IEEE Trans. on Communication, Vol. COM-21, No. 5, May 1973, pp. 548-563.

2.6 P. Horn et al., "Theoretical Study of Multipath Effects in an Aeronautical Satellite System," Messerschmidt-Bialkow Blohm GmbH for European Space Res. Technol. Cen., Syst. Study Div., Noordwijk, Holland, Final Report Contract 1064/70CG (RFQ 1737), Nov. 1970.

2.7 R. W. Sutton, et al., "Sattelite-Aircraft Multipath and Ranging Experiment Results at L-Band," IEEE Trans. on Communication, Vol. COM-21, No. 5, May 1973, pp. 639-646.

2.8 B. Kinsman, Wind Waves, Prentice-Hall, Inc., Englewood Cliffs, New Jersey, 1965.

2.9 P. A. Bello, "Aeronautical Channel Characterization," IEEE Trans. on Comm., Vol. COM-21, No. 5, May 1973, pp. 548-564.

2.10 L. M. Brekhovskikh, "The Diffraction of Waves by a Rough Surface Part I," (in Russian), Zh Eksper i Teor, Fiz. Vol. 23, 1952, pp. 275-289.

2.11 C. Cox and W. Munk, "Measurement of the Roughness of the Sea Surface from Photographs of the Sun's Glitter," J. Opt. Soc. of Amer., Vol. 44, No. 11, November 1954, pp.838-850.

2.12 K. M. Mitzner, "Effects of Small Irregularities on Electromagnetic From an Interface of Arbitrary Shape," J. Math Physics, Vol. 5, No. 12, pp. 1776-1786, 1964.

2.13 I. M. Fuks, "Theory of Radio Wave Scattering at a Rough Sea Surface," Izvestiga VUZ Radifizika, Vol. 9 No. 5, pp. 876-887, 1966.

2.14 D. Stillwell, "Directional Energy Spectra of the Sea From Photographs," J. Geoph. Res., Vol. 74, No. 8, April 1969, pp. 1974-1986.

2.15 I. Katz and C. I. Beard, "Methods for Measuring Ocean Waves," APL/JHU CF-2177, February 1954.

2.16 A Papoulis, Probability, Random Variables, and Stochastic Processes, McGraw-Hill, New York, 1965.

2.17 D. B. Ross, et al., "Laser and Microwave Observations of Sea-Surface Condition for Fetch-Limited 17- to 25-m/s Winds," IEEE Trans. on Geos. Elec., Vol. GE-8, No. 4, October 1970, pp. 323-336.

2.18 W. J. Pierson and L. Moskowitz, "A Proposed Spectral Form for Fully Developed Wind Seas Based on the Similarity Theory of S. A. Kitaigorodskii," J. Geophys. Res. 69, (No. 24), 5181, 1964.

2.19 R. O. Pilon, Determination of Ocean Surface Descriptors Using Sea Photo Analysis Techniques, NRL Report 7574, NRL, Washington, D.C., July 18, 1973.

3. SIMULTANEOUS DATA TRANSMISSION AND TONE PROBING THROUGH A HARD LIMITER

This section considers the problem of transmitting one or two tones with a data signal through a hard-limiting satellite repeater to an aircraft so that the tones may be used to sample the time variant transfer function of the satellite-aircraft channel in the vicinity of the data signal. The tones and data signal are assumed to occupy no more than the 50 Kc narrowband Aerosat channel. In addition the data signal is to be FSK and/or PSK at 1200 bits/sec. Due to the hard limiting, both signal suppression effects and intermodulation products are produced. This analysis is concerned with determining the effect of the selection of frequency locations and relative amplitudes of the tones and data signal on signal suppression and signal/intermodulation power ratios.

3.1 MATHEMATICAL FORMULATION

The complex envelope of the signal into the hard limiter for the two-tone case may be expressed in the form

$$z(t) = \alpha e^{j2\pi Ft} + \alpha e^{-j2\pi Gt} + e^{j\theta(t)} \tag{3.1}$$

where the tones are located F Hz above and G Hz below the data signal. Each tone has an amplitude α relative to the data signal.

The hard limiter output is given by

$$\ell(t) = \frac{z(t)}{|z(t)|} \tag{3.2}$$

Using (3.1) in (3.2) we find

$$\ell(t) = e^{j\theta(t)} \left\{ \frac{1 + \alpha e^{jX} + \alpha e^{-jY}}{|1 + \alpha e^{jX} + \alpha e^{-jY}|} \right\} \tag{3.3}$$

where

$$X = 2\pi Ft - \theta(t) \tag{3.4}$$

$$Y = 2\pi Gt + \theta(t) \tag{3.5}$$

Note that the term in brackets is doubly periodic in X and Y and may be expanded in a Fourier series, i.e.,

$$\ell(t) = e^{j\theta(t)} \sum_{-\infty}^{\infty} \sum_{-\infty}^{\infty} q_{nm} e^{jnX} e^{-jmY} \tag{3.6}$$

where

$$q_{nm} = \frac{1}{(2\pi)^2} \int_{-\pi}^{\pi} \int_{-\pi}^{\pi} \left\{ \frac{1 + \alpha e^{jX} + \alpha e^{-jY}}{|1 + \alpha e^{jX} + \alpha e^{-jY}|} \right\} e^{-jnX} e^{jmY} \, dXdY \tag{3.7}$$

It is readily determined that q_{nm} is real, so that (3.7) may be simplified to

$$q_{nm} = \frac{2}{(2\pi)^2} \int_{0}^{\pi} \int_{-\pi}^{\pi} \frac{\cos(mY-nX) + \alpha \cos(mY-(n-1)X) + \alpha \cos((m-1)Y-nX)}{\sqrt{1 + 2\alpha^2 + 2\alpha^2 \cos(X+Y) + 2\alpha \cos X + 2\alpha \cos Y}} \, dxdy \tag{3.8}$$

Using (3.4), (3.5) in (3.6) we find that

$$\ell(t) = q_{00}e^{j\theta(t)} + q_{10}e^{j2\pi Ft} + q_{01}e^{-j2\pi Gt}$$

$$+ \sum_{n=-\infty}^{\infty} \sum_{m=-\infty}^{\infty} q_{nm}e^{j2\pi(nF-mG)t}e^{j(1-m-n)\theta(t)}$$

$$m,n \neq (0,0),\ (1,0),\ (0,1) \qquad (3.9)$$

The first three terms are the desired terms and the other terms are intermodulation distortion terms. Note that each intermodulation term may be regarded as an interfering data signal with a generally increased modulation index (by the factor (1-m-n)) located at the frequency nF-mG. The spectral width of the intermodulation term depends on the character of $\theta(t)$. For binary DPSK it may be seen that exp $[j(1-m-n)\theta(t)]$ will reduce to the data signal or its complement when (1-m-n) is an odd integer, but when (1-m-n) is even it reduces to a constant. On the other hand, for FSK the term exp $[j(1-m-n)\theta(t)]$ will be an FSK data signal with new mark and space signals increased in separation by (1-m-n).

Consider now the simpler case of a single probing tone. In this case the input signal is represented by

$$z(t) = \alpha e^{j2\pi Ft} + e^{j\theta(t)} \qquad (3.10)$$

and the limited signal by

$$\ell(t) = e^{j\theta(t)} \left\{ \frac{1 + \alpha e^{jX}}{|1 + \alpha e^{jX}|} \right\} \tag{3.11}$$

A single Fourier series expansion of the bracketed term yields

$$\ell(t) = e^{j\theta(t)} \sum_{-\infty}^{\infty} c_n e^{jnX} \tag{3.12}$$

where

$$c_n = \frac{1}{2\pi} \int_{-\infty}^{\infty} \left\{ \frac{1 + \alpha e^{jX}}{|1 + \alpha e^{jX}|} \right\} e^{-jnX} \, dX$$

$$= \frac{1}{\pi} \int_{0}^{\infty} \frac{\alpha \cos (n-1)X + \cos nX}{\sqrt{1 + 2\alpha \cos X + \alpha^2}} \, dX \tag{3.13}$$

Thus

$$\ell(t) = c_0 e^{j\theta(t)} + c_1 e^{j2\pi Ft} + \sum_{\substack{-\infty \\ n\neq 0,1}}^{\infty} c_n e^{j2\pi nFt} e^{-j(n-1)\theta(t)} \tag{3.14}$$

The intermodulation components again are pseudo-data signals but now are centered at the frequencies nF. In contrast with the double-tone sounding case, one may select F so that no

intermodulation components overlap onto the data and probing signals.

3.2 NUMERICAL RESULTS

Computer evaluation of Fourier coefficients were carried out for the single and double tone cases for a range of values of α up to α=1. Figure 3.1 presents graphs of q_{nm} as a function of α for selected values of (n,m). The values of (n,m) selected were the result of a laborious iterative procedure where spectral widths and locations of intermodulation components were accounted for in determining those components which overlapped data and tone signals as a function of positions of the probing tones relative to the data signal. A general data signal was considered first, but subsequent calculations revealed that it was necessary to take advantage of the reduced bandwidth expansion of DPSK intermodulation components to keep the number of interfering components of significant strength small enough. The values of m,n depend upon the tone frequencies which must be selected to minimize the number of low order interfering intermodulation components overlapping onto the data signal (the low order ones having the higher strengths). As a result of this minimization,tone frequencies were selected 17.5 KHz above and 7 KHz below the data signal. Figure 3.2 presents for α = .45 an idealized sketch of the spectrum at the limiter output for the components listed in Fig. 3.1. The bandwidth of an intermodulation component is assumed to be either zero or the bandwidth of the data signal because of the assumption of DPSK, as discussed in Section 3.1. This is clearly an idealization since the DPSK modem output will depart from the mathematical model in two important ways: phase transitions will not occur in zero

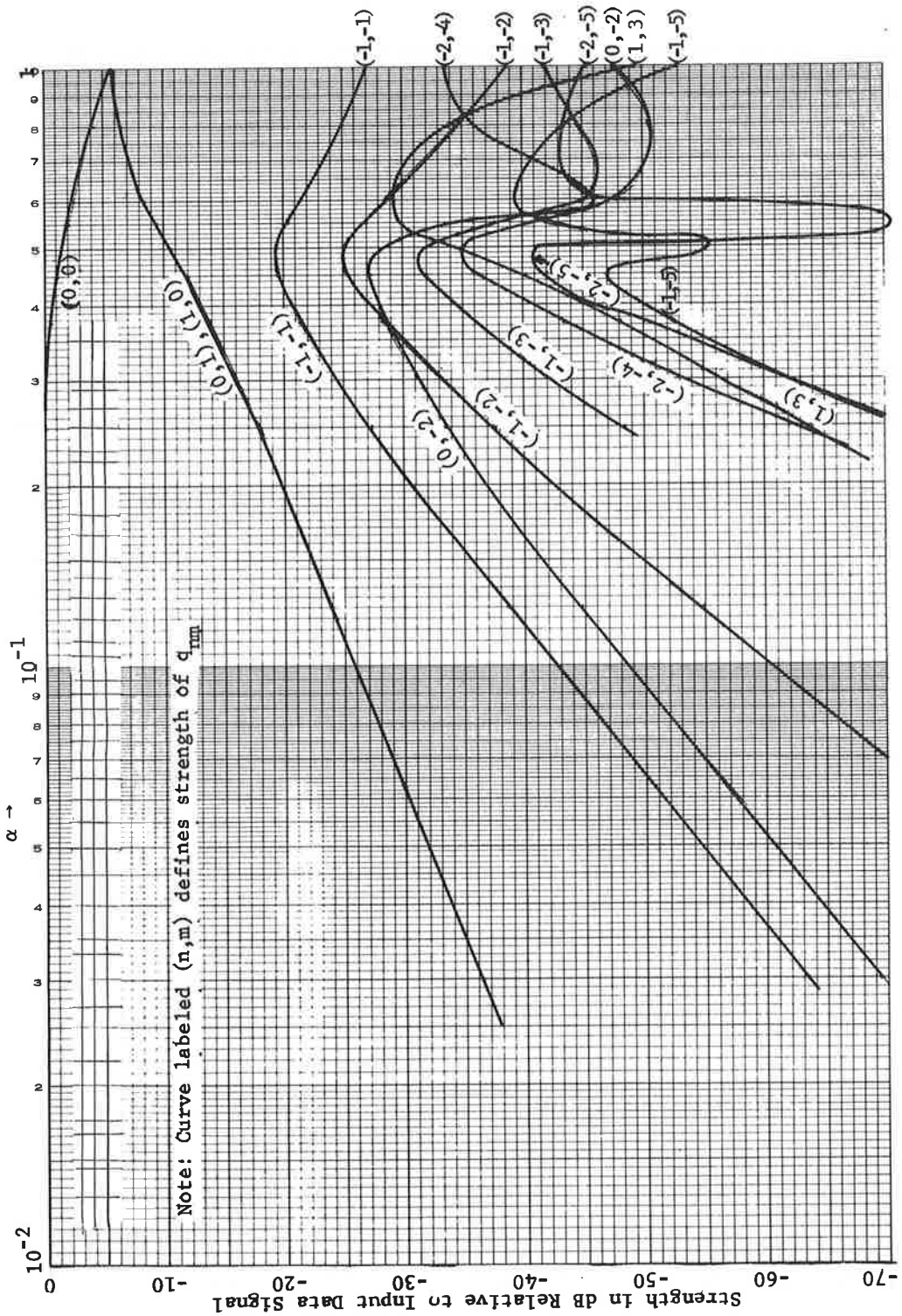

Figure 3.1 Strength of Selected Limiter Output Components as a Function of Probing Tones Strength α. Two Probing Tones

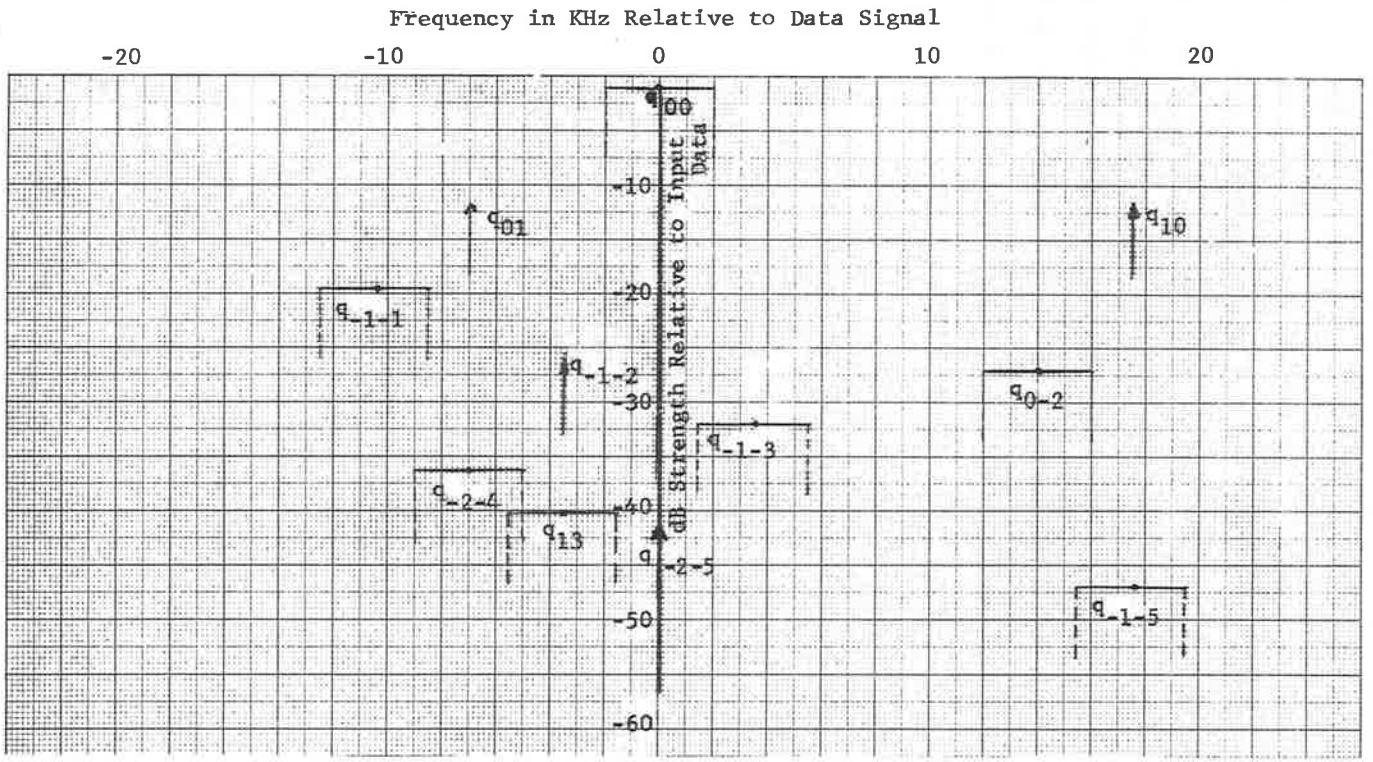

Figure 3.2 Sketch of Limiter Output Spectrum for Two Probing Tones F = 17.5 KHz, G = 7.0 KHz, and α = .45

time and some output bandlimiting will occur, introducing phase and amplitude fluctuations. Both these departures will make the intermodulation components broader in spectrum occupancy. Without detailed knowledge of the modem processing it is not possible to predict precisely the power spectra of the intermodulation components. In fact even the spectrum of the DPSK modem output cannot be clearly defined. We have, somewhat arbitrarily, represented the DPSK modem output as being confined to a bandwidth of 4 Kc for a 1.2 Kb/sec signal.

With the limited available radiated power in the Aerosat experiments it appears that too much suppression of the sounding tones by the hard limiter will not be allowable. In fact one may argue that α should be set equal to unity because the maximum fading rates will be an appreciable fraction of the data rate. Thus with α=1 and widening the probing tone filter to pass the full Doppler spectrum, the received probing tone SNR will be only a few dB bigger than the data signal SNR. At 50 dB-Hz, total received signal power to noise power density, the data signal SNR cannot exceed 18 dB and will be less as power is allocated to probing tones. Accurate measurement of channel phase fluctuations with the probing tones requires sufficient SNR, e.g., 20 dB for 36^{o} phase error.

For α=1 we see from Fig. 3.1 that the limiter output data and probing signals are suppressed equally around 6 dB relative to their input powers, and that the only significant interfering intermodulation component is the case n = -2, q = -4 which overlaps the probing tone at 7 KHz but is 27.5 dB below it.

Filtering the probing tone at the receiver will reduce this intermodulation component at least another 3 dB to 30.5 dB below the received tone limit. It appears very likely that the additive noise level on the extracted tone will be larger than this intermodulation component.

In the case of single tone probing it is possible to select the tone spacing so that no interfering intermodulation components exist. From Eq. (3.14) we see that the two components adjacent to the desired components are

$$c_{-1}e^{-j2\pi Ft}\, e^{+j2\theta(t)} + c_2 e^{j4\pi Ft} e^{-j\theta(t)} \qquad (3.15)$$

Assuming idealized DPSK, the intermodulation component F Hz below the data signal has zero bandwidth while that at 2 F Hz has the bandwidth of the data signal.*

Figure 3.3 presents plots of the coefficients c_{-2}, c_{-1}, c_0, c_1, c_2 as a function α. Note that at α=1 a 2 dB signal suppression effect occurs as opposed to the 6 dB suppression produced for the two sounding tones.

*If exp (j2θ(t)) could be regarded as a constant, then one might consider using this intermodulation component as an additional probing tone. However, the utility of this concept depends upon the detailed spectral characteristics of the DPSK modem output.

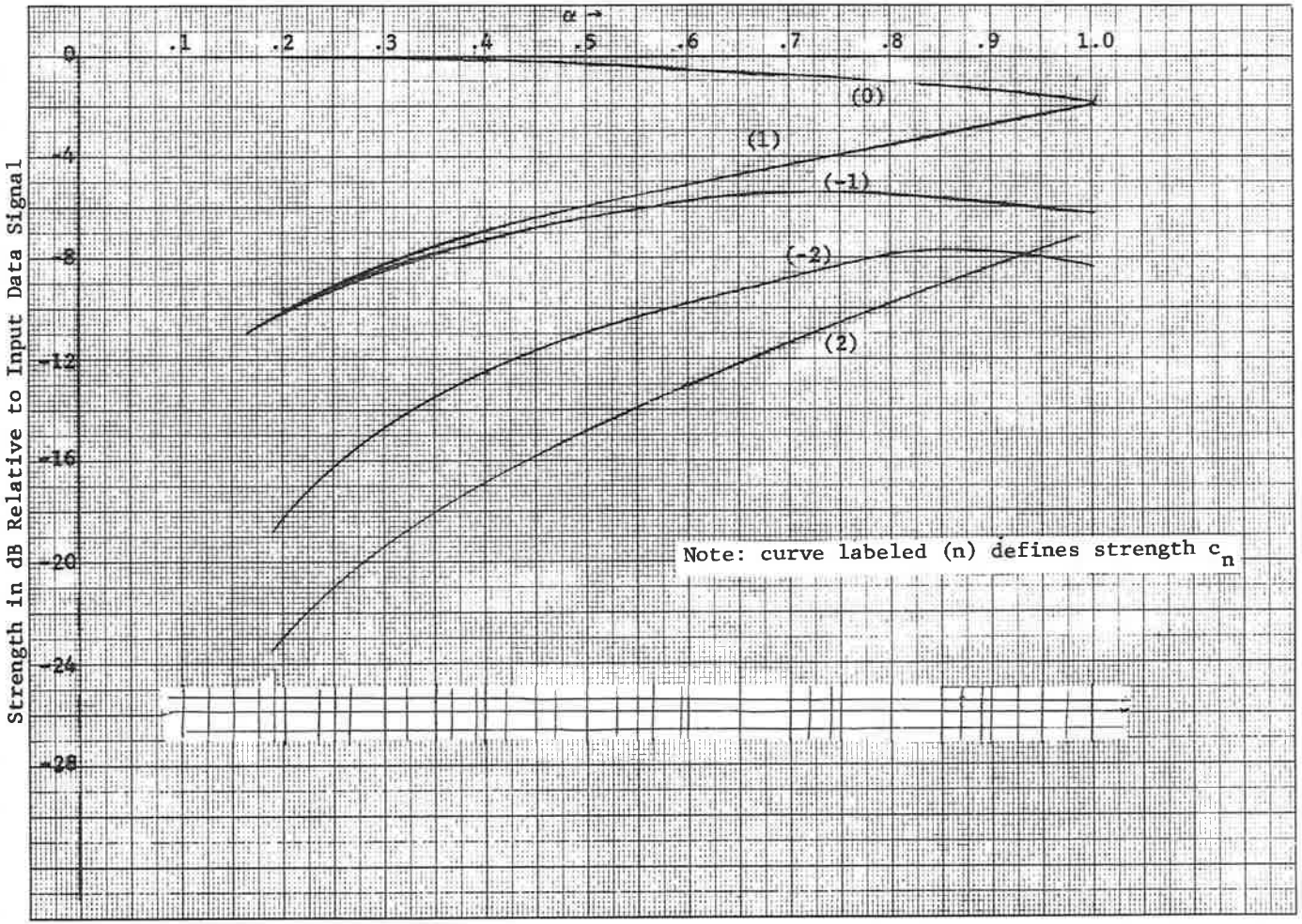

Figure 3.3 Strength of Selected Limiter Output Components as a Function of Single Tone Probing Strength

4. PERCENTAGE MEASUREMENT ERROR FOR MEASUREMENT OF ERROR RATE IN RICEAN CHANNELS

The time required to achieve a given rms error in measurement of error rate is larger on a fading than a non-fading channel. This section derives expressions for the rms error in error rate measurement for binary orthogonal transmission when the receiver employs predetection maximal-ratio diversity combining and incoherent detection. The channel statistics are assumed flat-fading Ricean (multiplication by a complex Gaussian non-zero-mean random process).

We define a sample error rate P_K as the sum

$$P_K = \frac{1}{K} \sum_{k=1}^{K} x_k \tag{4.1}$$

where x_k is a random variable

$$x_k = \begin{cases} 1 \; ; & \text{the k'th binary symbol is received in error} \\ 0 \; ; & \text{the k'th binary symbol is received correctly} \end{cases} \tag{4.2}$$

The mean squared and variance of the sample error rate are given by

$$\overline{P}_K = \frac{1}{K} \sum_{k=1}^{K} \overline{x_k} = \overline{x} \tag{4.3a}$$

$$\overline{P_K^2} = \frac{1}{K^2} \sum_{1}^{K} \sum_{1}^{K} \overline{x_k x_\ell} = \frac{1}{K} \sum_{-(K-1)}^{(K-1)} (1 - \frac{s}{K}) c_s \qquad (4.3b)$$

$$\overline{\sigma_G^2} = \overline{P_K^2} - \overline{P_K}^2 = \frac{1}{K} \sum_{-(K-1)}^{K-1} (1 - \frac{s}{K})(c_s - \overline{x}^2) \qquad (4.3c)$$

where we have assumed stationary statistics,

$$c_s = \overline{x_k x_{k+s}} \qquad (4.4)$$

Note that $\overline{x_k}$ is the probability that the k'th symbol is received in error over the ensemble of possible channel conditions. Similarly $\overline{x_k x_\ell}$ is the ensemble probability that the k'th and ℓ'th binary symbols are both received in error. To calculate the mean, mean squared, and variance of the sample error rate requires the computation of these two averages. We shall compute these averages in two steps. First we shall fix the channel fluctuations and average over the additive noise alone. These conditional probabilities will then be averaged over the channel fluctuations.

The channel and receiver structure we wish to analyze are shown in Fig. 4.1. The complex signal input to the matched filters w(t), can be expressed in the form

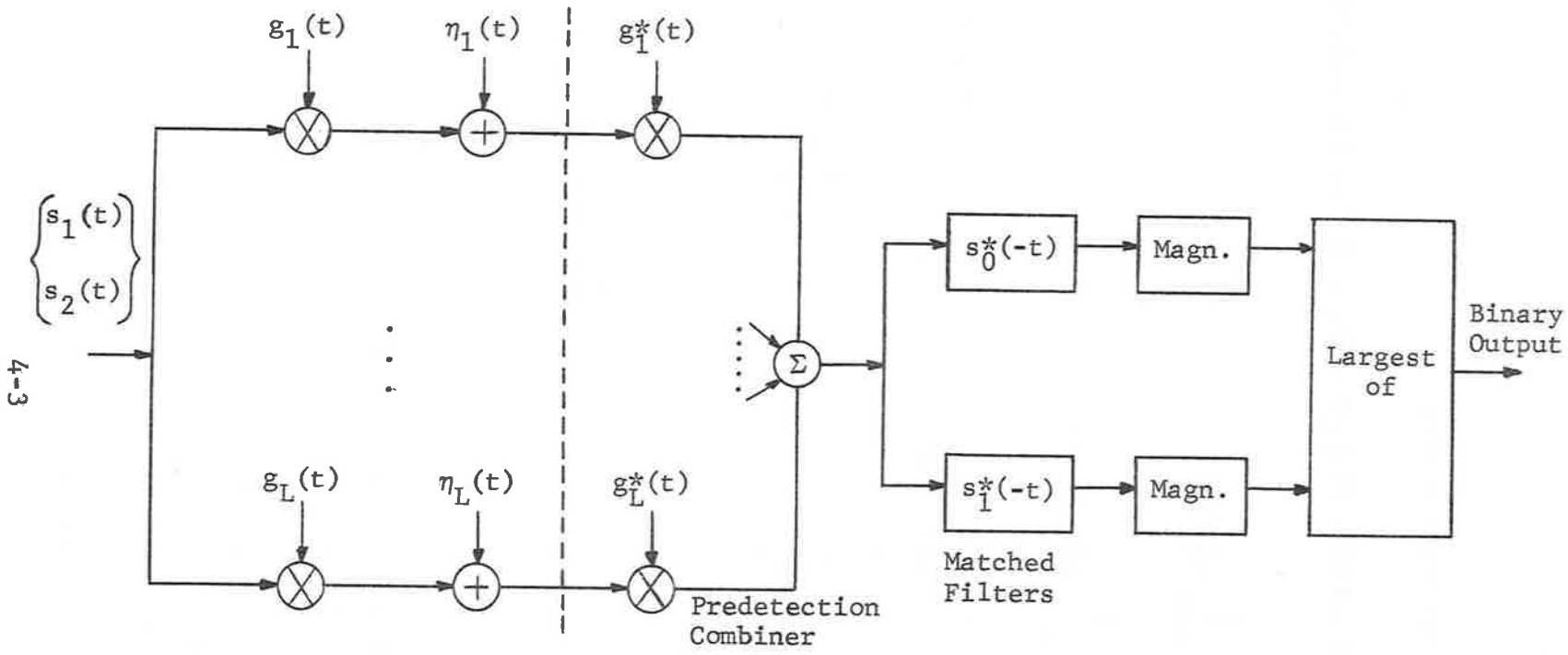

Figure 4.1 Predetection Maximal Ratio Combining With Incoherent Detection of Binary Orthogonal Signals

$$w(t) = Z(t)s(t) + N(t) \tag{4.5}$$

where s(t) is the complex representation of the transmitted signal and

$$Z(t) = \sum_{\ell=1}^{L} |g_\ell(t)|^2 \tag{4.6}$$

$$N(t) = \sum_{\ell=1}^{L} g_\ell^*(t)\eta_\ell(t) \tag{4.7}$$

in which $g_\ell(t)$ is the complex gain of the ℓ'th diversity channel and $\eta_\ell(t)$ is the additive noise of the same channel. Note that when $\{g_\ell(t);\ \ell = 1,2, \ldots L\}$ are fixed, w(t) becomes identical to a received signal over a white Gaussian noise channel in which the one sided noise power density N_0 is

$$\hat{N}_0 = Z\ N_0 \tag{4.8}$$

where N_0 is the one sided noise power density for a single diversity channel and the signal energy $\hat{E}$ is

$$\hat{E} = Z^2 E \tag{4.9}$$

where E is the energy of the received real signal over some time interval of duration T,

$$E = \frac{1}{2}\int_0^T |s(t)|^2 dt \tag{4.10}$$

The transmitted data signal is given by

$$s(t) = \Sigma\ s_{\alpha_k}(t-kT) \tag{4.11}$$

where

$$\alpha_k = \begin{cases} 0 \; ; & \text{transmitted source digit = 0 for } (k-1)T < t < kT \\ 1 \; ; & \text{transmitted source digit = 1 for } (k-1)T < t < kT \end{cases} \tag{4.12}$$

and $s_1(t)$, $s_2(t)$ are orthogonal, equal energy signals,

$$\int_0^T s_1^*(t) s_0(t)\, dt = 0 \tag{4.13}$$

$$\frac{1}{2}\int_0^T |s_1(t)|^2 dt = \frac{1}{2}\int_0^T |s_0(t)|^2 dt = E \tag{4.14}$$

Assuming matched filters followed by envelope detectors and a "largest of" selection as shown in Fig. 4.1, the probability that the k'th symbol is received in error conditioned on a particular fading history is given, for slow fading, by [4.1]

$$E[x_k/Z(t)] = \frac{1}{2}\exp\left[-\frac{\hat{E}}{2\hat{N}_0}\right] = \frac{1}{2}\exp\left[-\frac{1}{2}Z(kT)\rho\right] \tag{4.15}$$

where ρ is the average input SNR for one diversity channel and we have normalized

$$\overline{|g_\ell|^2} = 1 \tag{4.16}$$

The conditional probability of having the k'th and p'th digits both received in error is just the product $E[x_k/Z(t)]$ $E[x_p/Z(t)]$ because the noises are assumed independent in the k'th and p'th time intervals occupied by the signals carrying the k'th and p'th pulses. Thus

$$E[x_k x_p/Z(t)] = \begin{cases} \frac{1}{4} \exp\ [-\frac{1}{2}\ (Z(kT) + Z(pT))\rho] & ;\quad k\neq p \\ \\ \frac{1}{2} \exp\ [-\frac{1}{2}\ Z(kT)\rho] & ;\quad k=\rho \end{cases} \tag{4.17}$$

where the second equality follows from the fact that $\overline{x_k^n} = x_k$.

We consider now the average of the conditional expectations over the channel fluctuations

$$\overline{x_k} = \overline{E[x_k/Z(t)]} \tag{4.18}$$

$$\overline{x_k x_{k+s}} = \overline{E[x_k x_{k+s}/Z(t)]} \qquad ; \qquad k\neq s \tag{4.19}$$

The averages we desire are special cases (P=1 and P=2) of the more general average

$$\overline{E[x_{\nu_1} x_{\nu_2} \cdots x_{\nu_P}/Z(t)]} = \frac{1}{2^P} \overline{\exp\ [-\frac{1}{2}\ \rho \sum_{p=1}^{P} Z(\nu_p T)]} \quad ;\ \nu_1\neq\nu_2\neq \cdots \neq\nu_P \tag{4.20}$$

Note that

$$\sum_{p=1}^{P} Z(\nu_p T) = \sum_{\ell=1}^{L} \sum_{p=1}^{P} |g_\ell(\nu_p T)|^2 \tag{4.21}$$

is a Hermitian symmetric quadratic form in complex Gaussian non-zero mean random variables. Thus the desired average is just the characteristic function of this quadratic form evaluated at a particular value of the characteristic function variable. Fortunately this characteristic function is known [4.2] so that under very general conditions of correlation and mean values among the variables $\{g_\ell(\nu_p T);\ \ell=1, \ldots L,\ p=1, \ldots P)\}$, we may evaluate the p'th order moment in (4.20).

In the present case by trivial linear transformations we can avoid the heavy machinery in [4.2] if we assume independently fluctuating diversity channels and consider $P \leq 2$. Thus with these assumptions we note that

$$\overline{x_k x_{k+s}} = c_s = \begin{cases} \frac{1}{4}\left[\overline{\exp\left[-\frac{1}{2}\rho(|g_\ell(kT)|^2 + |g_\ell((k+s)T)|^2)\right]}\right]^L & ;\quad s\neq 0 \\ \frac{1}{2}\left[\overline{\exp\left[-\frac{1}{2}\rho|g_\ell(kT)|^2\right]}\right]^L & ;\quad s=0 \end{cases} \tag{4.22}$$

To simplify notation let

$$z = g_\ell(kT) \tag{4.23}$$

$$w = g_\ell((k+s)T) \tag{4.24}$$

In general z and w are correlated. Assuming identically distributed diversity channels

$$\bar{z} = \bar{w} = \overline{g_\ell(t)} \equiv \alpha \tag{4.25}$$

$$\overline{|z - \bar{z}|^2} = \overline{|w - \bar{w}|^2} = 2\sigma^2 \tag{4.26}$$

$$\overline{(z - \bar{z})^*(w - \bar{w})} = 2\sigma^2 r(sT)e^{j\theta(sT)} \tag{4.27}$$

where α is the steady or non-fading component in the channel, σ^2 is the strength of the fluctuating component, and $re^{j\theta}$ is the complex normalized correlation coefficient between $g_\ell(kT)$ and $g_\ell((k+s)T)$, (r is the magnitude and θ is the phase). Because the channel is stationary this correlation depends only on the time difference sT.

Recall we had normalized

$$\overline{|w|^2} = \overline{|z|^2} = 2\sigma^2 + |\alpha|^2 = 1 \tag{4.28}$$

so that σ^2, $|\alpha|^2$ are related with this normalization.

Other parameters of more common use in channel modeling are

$$S = \rho\left(\frac{1+\gamma}{\gamma}\right) \tag{4.29}$$

$$\gamma = \frac{1}{2\sigma^2} - 1 = \frac{|\alpha|^2}{2\sigma^2} \tag{4.30}$$

$$\beta = \frac{S}{\gamma} \tag{4.31}$$

where S is the direct path SNR, γ is the direct path/scatter path power ratio, and β is the scatter path SNR.

If z, w are two correlated complex Gaussian variables we may express these variables in terms of independent complex Gaussian variables u, v by

$$z = e^{-j\theta}(u+v) \tag{4.32}$$

$$w = (u - v) \tag{4.33}$$

or

$$u = \frac{1}{2}\,(ze^{j\theta} + w) \tag{4.34}$$

$$v = \frac{1}{2}\,(ze^{j\theta} - w) \tag{4.35}$$

With the transformations (4.32), (4.33)

$$|z|^2 + |w|^2 = 2(|u|^2 + |v|^2) \tag{4.36}$$

and

$$\overline{x_k x_{k+s}} = \frac{1}{4}\left[\overline{\exp\ [-\rho\,|u|^2]}\ \overline{\exp\ [-\rho\,|v|^2]}\right]^L \tag{4.37}$$

From [4.2], [4.3] we see that for a complex Gaussian non-zero-mean random variable w,

$$\overline{\exp\ [-\rho\,|w|^2]} = \frac{1}{1+2\rho}\ \exp\ [\frac{-\rho}{1+2\rho}\ |\bar{w}|^2] \tag{4.38}$$

where w has been normalized so that

$$\overline{|w - \bar{w}|^2} = 2 \tag{4.39}$$

For

$$\overline{|w - \bar{w}|^2} = 2\delta^2 \tag{4.40}$$

From (4.34) and (4.35) we find

$$\overline{\exp\ [-\rho |w|^2]} = \frac{1}{1 + 2\rho\delta^2} \exp\ [- \frac{\rho}{1 + 2\rho\delta^2} |\bar{w}|^2] \tag{4.41}$$

From

$$\bar{u} = \frac{1}{2} \alpha(e^{j\theta}+1) \tag{4.42}$$

$$\bar{v} = \frac{1}{2} \alpha(e^{j\theta}-1) \tag{4.43}$$

$$\overline{|u - \bar{u}|^2} = 2\sigma^2(\frac{1+r}{2}) \tag{4.44}$$

$$\overline{|v - \bar{v}|^2} = 2\sigma^2(\frac{1-r}{2}) \tag{4.45}$$

Thus using (4.42) - (4.44) in (4.41) and (4.37)

$$\overline{x_k x_{k+s}} = \frac{1}{4}\left[\overline{\exp\ [-\rho|u|^2]} \cdot \overline{\exp\ [-\rho|v|^2]}\right]^L$$

$$= \frac{1}{4}\left(\frac{1}{1+\rho\sigma^2(1+r)}\right)^L\left(\frac{1}{1+\rho\sigma^2(1-r)}\right)^L$$

$$\times \exp\left[-\frac{L\rho}{1+\rho\sigma^2(1+r)}\frac{|\alpha|^2}{2}(1+\cos\theta)\right]$$

$$\times \exp\left[-\frac{L\rho}{1+\rho\sigma^2(1-r)}\frac{|\alpha|^2}{2}(1-\cos\theta)\right] \quad ; \quad s\neq 0$$

(4.46)

Similarly

$$\bar{x} = \frac{1}{2}\left[\overline{\exp\ [-\tfrac{1}{2}\rho|z|^2]}\right]^L$$

$$= \frac{1}{2}\left[\frac{1}{1+\rho\sigma^2}\right]^L \exp\left[-\frac{L\rho}{1+\rho\sigma^2}\frac{|\alpha|^2}{2}\right] \qquad (4.47)$$

Alternatively, using the more familiar parameters S, γ (4.29), (4.30) and carrying out some algebra

$$c_s = \frac{1}{4}\left[\frac{1}{(1+\frac{\beta}{2})^2 - r^2(sT)\,\frac{\beta^2}{4}}\right]^L \exp\left[-L\gamma\beta\,\frac{1+\frac{\beta}{2}\,(1 - r(sT)\cos\theta(sT))}{(1+\frac{\beta}{2})^2 - r^2(sT)\,\frac{\beta^2}{4}}\right] \quad ; \quad s\neq 0$$

$$\bar{x} = \frac{1}{2}\left[\frac{1}{1+\beta/2}\right]^L \exp\left[-L\gamma\left(\frac{\beta/2}{1+\beta/2}\right)\right] = c_0 \tag{4.48}$$

Returning to Eqs. (4.3), (4.4) we note that the variance of the sample error rate error is given by

$$\sigma_\epsilon^2 = \overline{P_K^2} - (\overline{P_K})^2 = \frac{2}{K}\sum_{s=1}^{K-1}(1 - \frac{s}{K})(c_s - \bar{x}^2)$$

$$+ \frac{1}{K}(\bar{x} - \bar{x}^2) \tag{4.49}$$

where we have taken advantage of the even nature of $c_s = c_{-s}$. Note that the first term accounts for the contribution to the variance due to the statistical dependence of the channel between symbols while the second term is identical to that for independent fluctuation of the channel from bit to bit.

If c_s changes little in a time interval T, which is consistent with the slow fading assumption, then the summation in (4.49) may be closely approximated by the integral

$$\sigma_\epsilon^2 = \frac{2}{T_0}\int_T^{T_0} (1 - \frac{\tau}{T_0})D(\tau)\, d\tau + \frac{1}{K}(\bar{x} - \bar{x}^2)$$

$$\approx \frac{2}{T_0}\int_0^{T_0} D(\tau)\, d\tau + \frac{1}{K}(\bar{x} - \bar{x}^2) \qquad (4.50)$$

where

$$D(\tau) = \frac{1}{4}\left[\frac{1}{(1+\frac{\beta}{2})^2 - r^2(\tau)\,\frac{\beta^2}{4}}\right]^L \exp\left[-L\gamma\beta\,\frac{1+\frac{\beta}{2}\,(1 - r(\tau)\cos\theta(\tau))}{(1+\frac{\beta}{2})^2 - r^2(\tau)\,\frac{\beta^2}{4}}\right]$$

$$- \frac{1}{4}\left[\frac{1}{(1+\frac{\beta}{2})^2}\right]^L \exp\left[-L\gamma\beta\left(\frac{1}{1+\frac{\beta}{2}}\right)\right] \qquad (4.51)$$

Note that

$$\lim_{\tau \to \infty} D(\tau) = 0 \qquad (4.52)$$

The percentage rms error is given closely by

$$\eta = \frac{\sigma_\epsilon}{\bar{x}} \approx \sqrt{\frac{1}{2T_0}\int_0^{\infty} E(\tau)\, d\tau + \frac{1}{K}\left(\frac{1}{\bar{x}}\right)} \qquad (4.53)$$

where

$$E(\tau) = \left[\frac{(1+\frac{\beta}{2})^2}{(1+\frac{\beta}{2})^2 - r^2(\tau)\,\frac{\beta^2}{4}}\right]^L \exp\left[-L\gamma\beta\left(\frac{1+\frac{\beta}{2}\,(1 - r(\tau)\cos\theta(\tau))}{(1+\frac{\beta}{2})^2 - r^2(\tau)\,\frac{\beta^2}{4}} - \frac{1}{1+\frac{\beta}{2}}\right)\right] - 1 \tag{4.54}$$

and we have assumed

$$\bar{x} \ll 1 \tag{4.55}$$

i.e., an error rate much smaller than unity.

For a real channel correlation function

$$\theta(\tau) = 0 \tag{4.56}$$

and $E(\tau)$ simplifies to

$$E(\tau) = \left[\frac{1}{1 - r^2(\tau)\,(\frac{1}{1+2\gamma/S})}\right]^L \exp\left[LS\left(\frac{1}{1+\frac{S}{2\gamma}} - \frac{1}{1+\frac{S}{2\gamma}+r(\tau)\,\frac{S}{2\gamma}}\right)\right] - 1 \tag{4.57}$$

where we must now allow $r(\tau)$ to be in the range $-1 < r(\tau) < 1$.

Normalizing the time scale of the fading, we can express η in the form

$$\eta \approx \sqrt{\frac{C(S,\gamma)}{2BT_0} + \frac{1}{KP(S,\gamma)}} \tag{4.58}$$

where

$$C(S,\gamma) \equiv \int_0^\infty E(\hat{\tau}_B)\, d\hat{\tau} \tag{4.59}$$

and

$$P(S,\gamma) \equiv \overline{x} \tag{4.60}$$

Figures 4.2 and 4.3 present plots of $C(S,\gamma)$ and $P(S,\gamma)$ vs. γ for S = 8, 16, 32, 64 assuming a Gaussian fading correlation function

$$r(\hat{\tau}_B) = \exp\left[-\frac{1}{2}\pi^2\hat{\tau}^2\right] \tag{4.61}$$

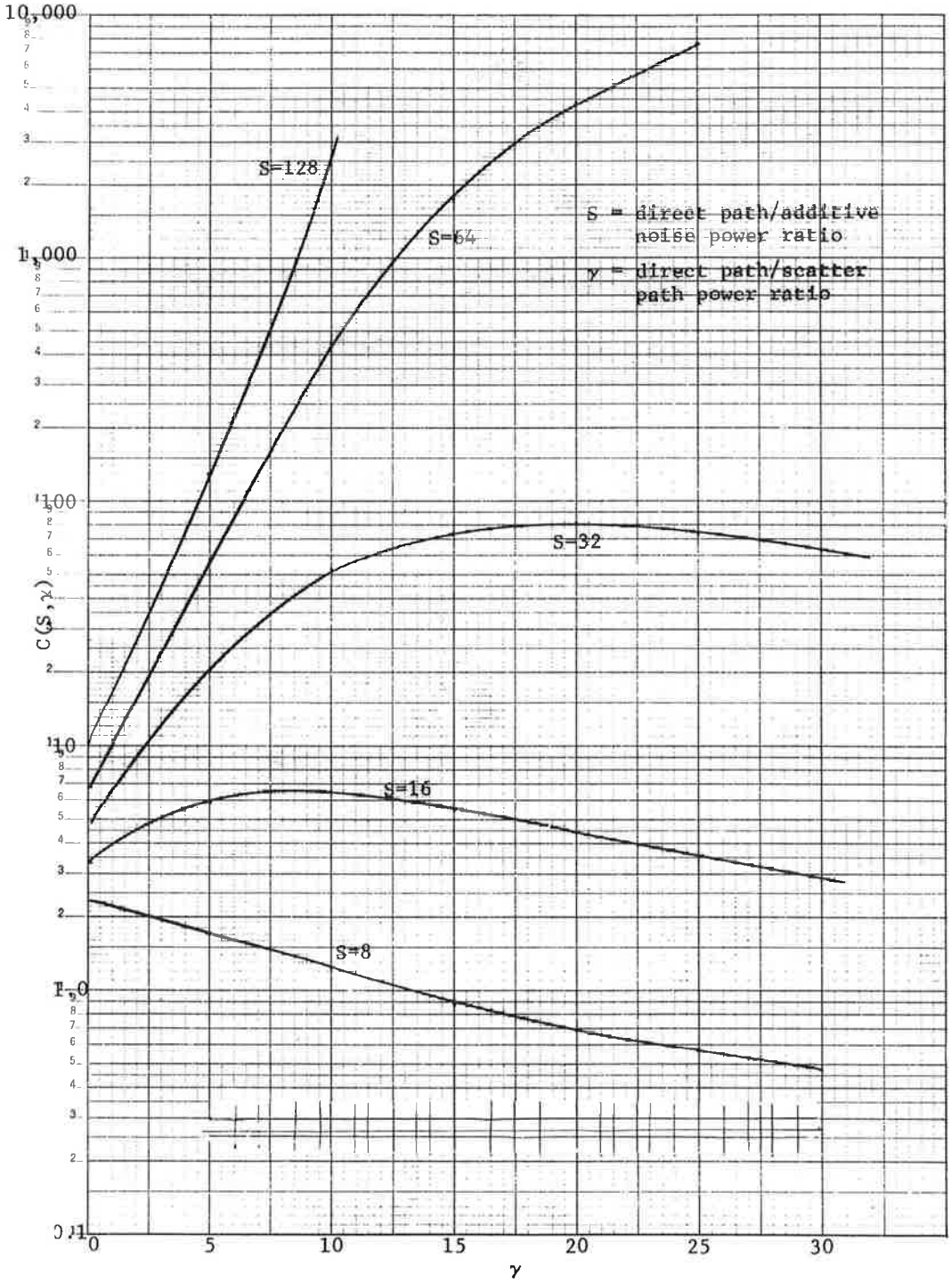

Figure 4.2 C(S,γ) Vs. γ for S=8, 16, 32, 64, 128

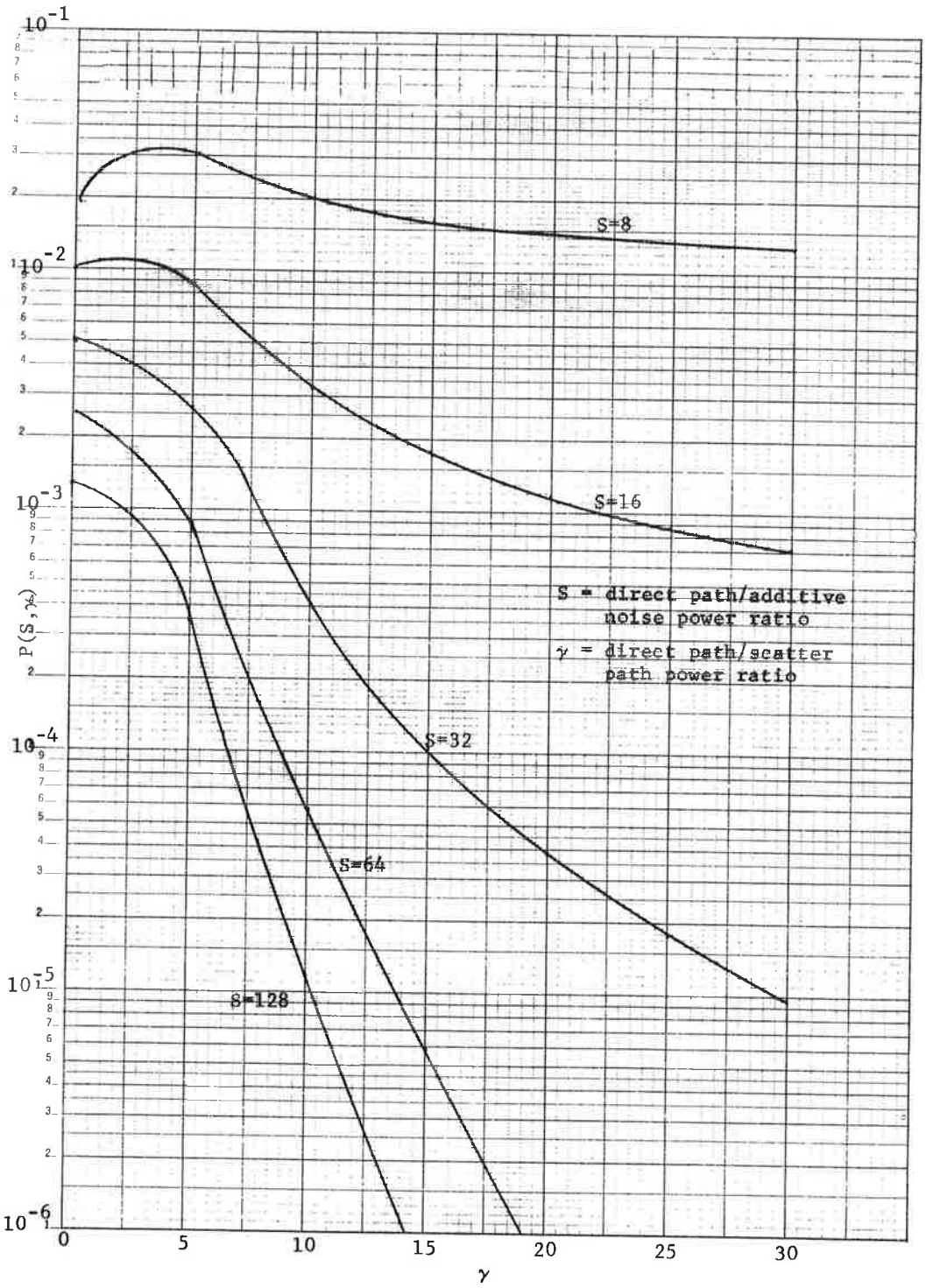

Figure 4.3 Error Rate P(S,γ) for Non-Coherent FSK Vs. γ for S=8, 16, 32, 64, 128

For large values of $\beta = S/\gamma$ we may find approximate expressions for $E(\tau)$ by using the expansion

$$r(\tau) \approx 1 - \frac{1}{2}(2\pi\tau)^2 \int f^2 P(f)\, df + \ldots \tag{4.62}$$

where $P(f)$ the Fourier transform of $r(\tau)$, is the Doppler power density spectrum. We have assumed that the carrier frequency has been chosen at the centroid of $P(f)$, i.e.,

$$\int f\, P(f)\, df = 0 \tag{4.63}$$

to be consistent with (4.56).

Using the definition of RMS Doppler spread B

$$B^2 = 4 \frac{\int f^2 P(f)\, df}{\int P(f)\, df} \tag{4.64}$$

and noting that we have normalized

$$\int P(f)\, df = r(0) = 1 \tag{4.65}$$

we see that

$$r(\tau) \approx 1 - \frac{1}{2}\pi^2 B^2 \tau^2 + \ldots \tag{4.66}$$

The first factor in (4.57) drops to a small value for small values of $B\tau$ when $\beta >> 1$. Using (4.66) in (4.57) for $\beta >> 1$ we find the approximate expression

$$E(\tau) \approx \left[\frac{1}{\frac{2}{\beta} + \pi^2 B^2 \tau^2}\right]^L \exp\,[\gamma L] \tag{4.67}$$

The integration of $E(\tau)$ over τ is given by

$$\int_0^\infty E(\tau)\, d\tau = \exp\,[\gamma L] \int_0^\infty \frac{d\tau}{(\frac{2}{\beta} + \pi^2 B^2 \tau^2)^L}$$

$$= \exp\,[\gamma L]\ (\frac{\beta}{2})^{L-\frac{1}{2}} \frac{1}{\pi B} \int_0^\infty \frac{d\tau}{(1+\tau^2)^L}$$

$$= \exp\,[\gamma L]\ (\frac{\beta}{2})^{L-\frac{1}{2}} \frac{1}{B} \frac{(2L-2)!}{2^{2L-1}[(L-1)!]^2} \tag{4.68}$$

For large β

$$P(S,\gamma) \to \frac{1}{2}\ (\frac{2}{\beta})^L \exp\,[-L\gamma] \tag{4.69}$$

Thus

$$\int_0^\infty E(\tau)\, d\tau \to \frac{1}{P(S,\gamma)} \frac{1}{B} \sqrt{\frac{2}{\beta}} \cdot \frac{(2L-2)!}{2^{2L}[(L-1)!]^2} \tag{4.70}$$

Using (4.58), (4.59), and (4.70) we see that for large β

$$\eta \approx \sqrt{\frac{1}{KP(S,\gamma)}} \sqrt{1 + \alpha_L} \quad ; \quad \beta >> 1 \tag{4.71}$$

$$\alpha_L = \sqrt{\frac{2}{\beta}} \cdot \frac{1}{BT} \cdot \frac{(2L-2)!}{2^{2L+1}[(L-1!)]^2} \tag{4.72}$$

Note that the factor in front in (4.71) is the error probability measurement percentage rms error for <u>independent</u> fading from bit to bit. The second term in the second square root determines the degree to which the rms error increases over that due to statistical dependence between bits. For non-diversity operation this term is

$$\alpha_1 = \frac{1}{4BT\sqrt{2\beta}} \tag{4.73}$$

In the case of the Aerosat channel with a data rate of 1200 bits/sec and a representative low rms Doppler spread of 50 Hz due to surface scatter multipath, this becomes

$$\alpha_1 = \frac{4.24}{\sqrt{\beta}} \quad ; \quad \beta >> 1 \tag{4.74}$$

which will be less than one for large β. In the case of ionospheric scintillation where fade rates are much slower, α_L could be much bigger than one.

Equations (4.72) and (4.74) apply for large β and seem to indicate that the measurement error blows up for small β. However (4.72) and (4.74) are only valid for $\beta \gg 1$. Actually as β decreases with S fixed (equivalent to γ increasing for S fixed) the measurement error due to the fading decreases to zero percent as may be seen from (4.57). Thus there is a worst value of β (or γ) at fixed S for which the percentage measurement error is maximized. For general β we may express α_L as (remember $\gamma = S/\beta$)

$$\alpha_L = \frac{P(S,\gamma)C(S,\gamma)}{2BT} \tag{4.75}$$

The integrals $P(S,\gamma)$, $C(S,\gamma)$ were evaluated at β=2, L=1, as a function of S assuming the Gaussian Doppler power spectrum. Using these results Fig. 4.4 shows a plot of $BT\alpha_1$, as a function of γ for S=8, 16, 32, 64, 128. Maxima occur in the vicinity of γ = 4 to 5. These maxima are quite close, ranging from .022 to .027. Then

$$\alpha_1 \leq \frac{.027}{BT} \tag{4.76}$$

For B = 50 Hz and T = 1/1200 this becomes

$$\alpha_1 \leq .648 \tag{4.77}$$

yielding

$$\eta \leq \frac{1.28}{\sqrt{KP(S,\gamma)}} \tag{4.78}$$

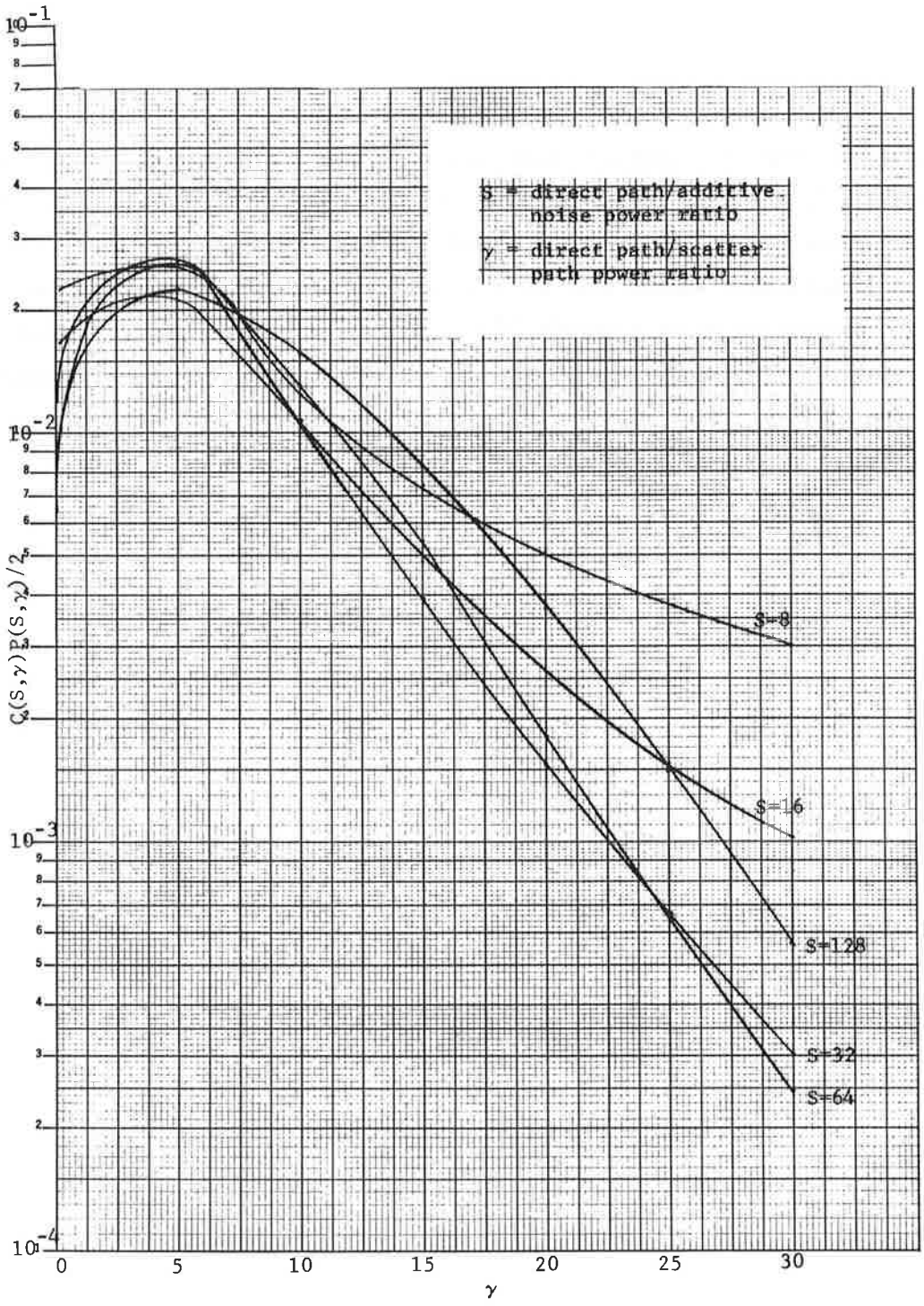

Figure 4.4 The Product $C(S,\gamma)P(S,\gamma)/2$ as a Function of γ for S=8, 16, 32, 64, 128

which is only a 28% increase in percentage rms measurement error due to the fading or alternatively, a 65% increase in measurement time to achieve the same percentage measurement error as would occur for a non-fading channel with the same average error rate. Were the Doppler spread to decrease to around 3 Hz, the increase in percentage measurement error would be 340%, or an increase in measurement time by a factor of around 12 to achieve the same percentage measurement error as would occur for a non-fading channel with the same average error rate.

REFERENCES

4.1 M. Schwartz, W. Bennet, and S. Stein, Communication Systems and Techniques, McGraw-Hill, 1966, p. 297.

4.2 G. L. Turin, "The Characteristic Function of Hermitian Quadratic Forms in Complex Normal Variables," Biometrica, Vol. 47, pp. 199-201, June 1960.

4.3 M. Schwartz, W. Bennet and S. Stein, Communication Systems and Techniques, McGraw-Hill, 1966, Appendix B, Part III.

5. CODING AND MODULATION CONCEPTS FOR AERONAUTICAL CHANNELS

5.1 INTRODUCTION

In this section the problem of transmitting digital data reliably over the aeronautical channel will be addressed. This particular channel is characterized by a time-varying distribution [5.1], [5.2], [5.3] which limits the effectiveness of certain types of conventional modulation techniques. Significant performance gains, i.e., a reduction in transmitted power and/or error probability, can be achieved if error correction coding concepts are combined with modulation concepts in an appropriate way. The importance of time domain coding techniques and the use of channel measurement information in the decoding process is illustrated by both theoretical and computer simulated results. By integrating these coding and modulation techniques it is shown for the aeronautical channel that it is quite possible to achieve a robust signaling technique which is fairly insensitive to the channel's scatter parameters; such as, scatter path energy and fading bandwidths. These results illustrate that the scatter energy does not limit the effectiveness of transmitting digital data and, in fact, can improve the performance when operating in the region of low direct signal-to-noise ratios. It is interesting to note that these coding results contradict many conventional system design approaches where every attempt is made to avoid the reception of scatter energy.

In evaluating the various signaling approaches a critical channel parameter is the ratio of the received direct signal power (Pr) to the noise power per Hertz (N_0). This ratio, sometimes denoted as C/KT, will be normalized by the data rate* (D) to obtain E_b/N_0 =

*This is the information bit rate which is less than the channel data rate when coding is applied.

P_r/DN_0, which is the direct path energy per data bit to the noise power density. All error probability results will be plotted as a function of E_b/N_0 so that a comparison can be made of a coded and uncoded system at the same received power.

The ratio of the scatter energy to the direct energy will be denoted by γ, and the correlation coefficient between the scatter components of successive signaling pulses will be denoted by ρ. Our results presented will be functions of E_b/N_0, γ and ρ, where the values of ρ are determined by the channel's fading bandwidth.*

5.2 APPLICATION OF CODING AND MODULATION TECHNIQUES

In this section both FSK and DPSK modulation formats will be considered and combined with error correction coding approaches.

5.2.1 DPSK Modulation

A possible receiving configuration for two-phase DPSK modulation formats is illustrated on Fig. 5.1. A baud interval of T seconds is assumed and an in-phase and quadrature component is received after T seconds of integration. Representing these two components as a complex number we have at the ith time interval

$$\overline{W_i} = U_i + jV_i \tag{5.1}$$

which for an assumed Rician channel is given by

$$\overline{W_i} = e^{j\pi X_i}[\overline{A} + \overline{S}_i] + \overline{N}_i \tag{5.2}$$

$$X_i = \text{data bit, 0 or 1} \tag{5.3}$$

*If a Gaussian spectrum of fading bandwidth $B = 2\sigma$ is assumed, i.e., $S(f) = \frac{2}{B\sqrt{2\pi}} e^{-2(f/B)^2}$ we have $\rho(\tau) = e - 1/2\ \pi^2 B^2 \tau^2 \approx 1 - \frac{\pi^2}{2} B^2 \tau^2$ for small values of $B\tau$. Similarly, if spectrum is assumed to be characterized by a (recursive) two-pole filter we also have $\rho(\tau) = \frac{1}{\cosh\ \pi B\tau} \approx 1 - \frac{\pi^2 B^2 \tau^2}{2}$ for small values of $B\tau$.

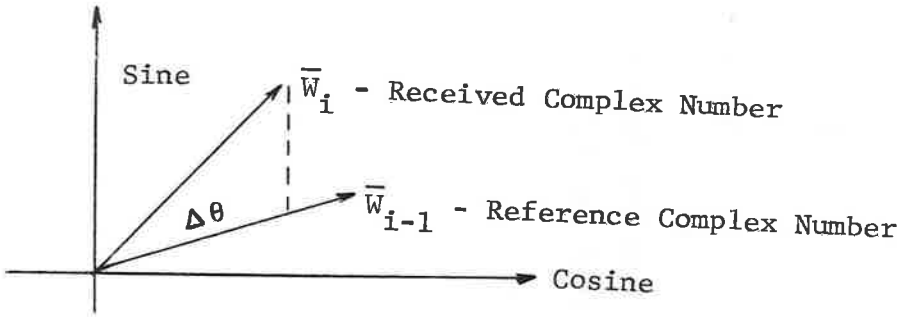

$$z_i = |\bar{W}_i|\,|\bar{W}_{i-1}| \cos \Delta\theta = U_i U_{i-1} + V_i V_{i-1}$$

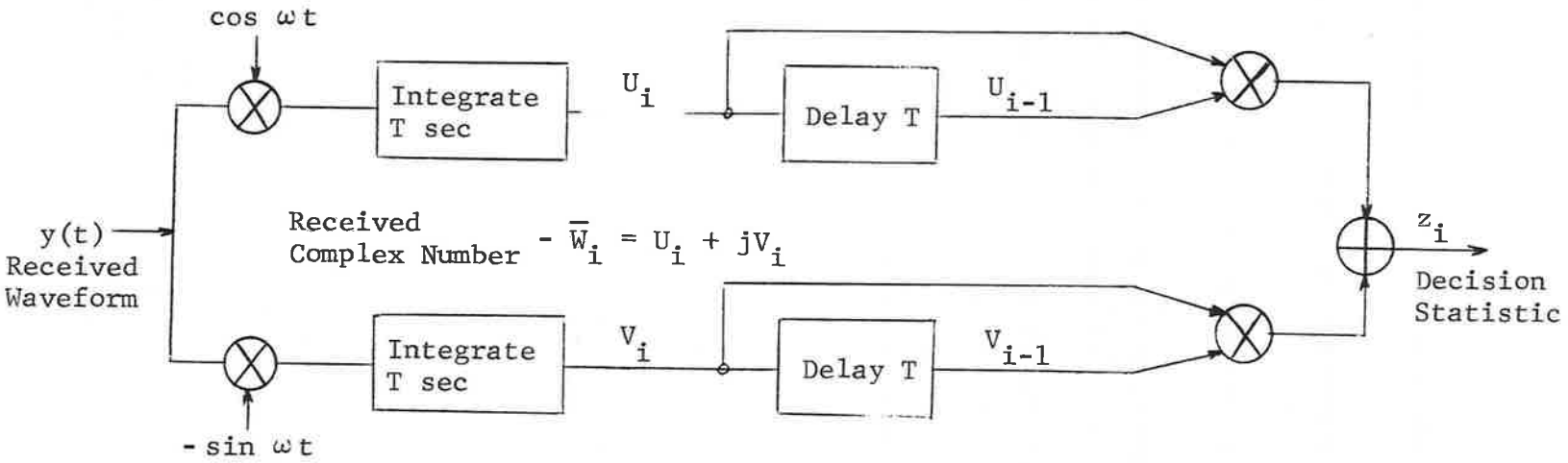

Confidence Value, $\alpha_i = |z_i|$

Binary Decision, $Y_i = 0$ if $z_i \geq 0$ (no phase change is assumed)

$= 1$ if $z_i < 0$ (180^o phase change is assumed)

Figure 5.1 Binary DPSK Demodulation

$\overline{A}$ = amplitude of direct component (5.4)

$\overline{S}$ = amplitude of scatter component (5.5)

$\overline{N}$ = additive Gaussian noise . (5.6)

The scatter component is assumed time-varying but with negligible delay difference* (multipath) between the components $\overline{A}$ and $\overline{S}$.

The energy over a T second interval associated with the above components can be written as

$$E_d = \overline{A}\ \overline{A}^* \text{ - direct signal components} \quad (5.7)$$

$$E_s = E[\overline{S}\ \overline{S}^*] \text{ - scatter components} \quad (5.8)$$

$$N_0 = E[\overline{N}\ \overline{N}^*] \text{ - noise components} \quad (5.9)$$

The in-phase and quadrature noise components are each assumed to have a variance of $\sigma^2 = N_0/2$.

To relate these energy terms to E_b/N_0 we first note that for a code of rate R composed of K information digits every N channel digits we have

$$R = \frac{K}{N} = DT < 1 \quad (5.10)$$

---

*A typical multipath spread for the aeronautical channel is 20 μsec (see Section 2) which for a well designed receiver will have a negligible effect on performance at the baud interval of 416.7 μsec; which occurs when a rate 1/2 code is used at a data rate of 1200 bps.

The signal-to-noise ratio per information bit can now be written as

$$\frac{E_b}{N_0} \doteq \frac{P_r}{N_0 D} = \frac{E_d/T}{N_0 D} = \frac{E_d}{N_0 R} \tag{5.11}$$

where in the above the received power P_r is given by E_d/T.

The ratio of the direct-to-scatter energy is now given by

$$\gamma = \frac{E_d}{E_s} \tag{5.12}$$

and the correlation coefficient over two successive signal bauds is given by*

$$\rho = \frac{E[\bar{S}_i \bar{S}^*_{i-1}]}{E_s} \tag{5.13}$$

For DPSK the reference statistic is obtained from the previous baud and is given by

$$\bar{W}_{i-1} = [\bar{A} + \bar{S}_{i-1}] + \bar{N}_{i-1} \tag{5.14}$$

The decision statistic is given by the dot product of $\bar{W}_i$ and $\bar{W}_{i-1}$, as

$$z_i = |\bar{W}_i||\bar{W}_{i-1}| \cos \wedge\rho = \mathrm{Re}[\bar{W}_i \bar{W}^*_{i-1}] = U_i U_{i-1} + V_i V_{i-1} \tag{5.15}$$

If this dot product is positive X_i is denoted as a 0, no phase change, while a negative dot product is decoded as 1.

The effects of the time variations in $\bar{S}$ can be modeled exactly for complex Gaussian processes by writing

$$\bar{S}_i = \bar{S}_0 + \bar{Z}_i \tag{5.16}$$

*For simplicity we assume here a symmetrical fading power spectrum and real ρ. The results may readily be generalized to complex ρ, i.e., unsymmetrical power spectra.

and

$$\bar{S}_{i-1} = \bar{S}_0 + \bar{Z}_{i-1} \tag{5.17}$$

where $\bar{S}_0$ is the completely correlated part of $\bar{S}_i$ and $\bar{S}_{i-1}$ and $\bar{Z}_{i-1}$ and $\bar{Z}_i$ represent zero-mean uncorrelated parts (independent for complex Gaussian) of $\bar{S}_i$ and $\bar{S}_{i-1}$. Thus we have

$$E[\bar{S}_i \bar{S}^*_{i-1}] = E[\bar{S}_0 \bar{S}^*_0] = \rho E_s \tag{5.18}$$

The variance of independent portions of $\bar{S}$ is given by

$$E[\bar{Z}\ \bar{Z}^*] = E[(\bar{S} - \bar{S}_0)((\bar{S}^* - \bar{S}^*_0)] = E_s(1-\rho) \tag{5.19}$$

Using the above results we can reduce the fast fading results to an equivalent slow fading result by noting that

$$\bar{W}_i = e^{j\pi X_i}[\bar{A} + \bar{S}_i] + \bar{N}_i = e^{j\pi X_i}[\bar{A} + \bar{S}_0] + \bar{Z}_i + \bar{N}_i \tag{5.20}$$

where the term $e^{j\pi X_i} = \pm 1$ so that the data has no effect on the statistics of $\bar{Z}_i$. The equivalent direct signal-to-noise ratio is now given by

$$\left(\frac{E_d}{N_0}\right)_{eq} = \frac{E_d}{E[\bar{Z}\ \bar{Z}^*] + E[\bar{N}\ \bar{N}^*]} = \frac{E_d}{E_s(1-\rho) + N_0} = \frac{\frac{E_d}{N_0}}{1 + \frac{E_d}{N_0}\frac{(1-\rho)}{\gamma}} \tag{5.21}$$

In terms of E_b/N_0 and the code rate R we have

$$\left(\frac{E_d}{N_0}\right)_{eq} = \frac{\left(\frac{E_b}{N_0}\right)R}{1 + \left(\frac{1-\rho}{\gamma}\right)\left(\frac{E_b}{N_0}\right)R} \qquad (5.22)$$

which can be used in expressions for the slow fading Rician channel [5.4] to obtain the error rate for the fast fading Rician channel. Note, of course, that the loss in signal-to-noise ratio due to the time-varying scatter components disappears as $\gamma \to \infty$, or $\rho \to 1$.

5.2.2 FSK Modulation

For the slow fading Rician channel the error performance of FSK is exactly equivalent to DPSK except for a 3 dB loss (factor of 2) in SNR [5.4]. Since the previous signaling baud is not used as a phase reference in an FSK receiver, (see Fig. 5.2), no adjustment in SNR is required unless the fading is so rapid that significant crosstalk is introduced into the adjacent decision filter. For the channel parameters assumed for the aeronautical channel* a negligible adjustment in E_b/N_0 is required for FSK and thus FSK will outperform DPSK when the value of $\left(\frac{1-\rho}{\gamma}\right)\left(\frac{E_b}{N_0}\right)R$ is greater than one. However, when the error correction coding is applied in the appropriate manner, the results in Section 5.4 indicate that FSK with coding will always be inferior to DPSK with coding.

5.2.3 Conventional Binary Coding

The most obvious (and highly unrecommended) approach for applying error correction coding to the aeronautical channel is illustrated on Fig. 5.3a.

---

*The crosstalk introduced into an adjacent decision filter at a fading bandwidth of 120 Hz can be made negligible by spacing the two transmitted frequencies by more than the reciprocal of the baud rate. Note also that the additive noise term Z_i in (5.20) for DPSK does not apply for FSK since $e^{j\pi X_i}$ is replaced by X_i, which will be zero for one filter and one for the adjacent filter.

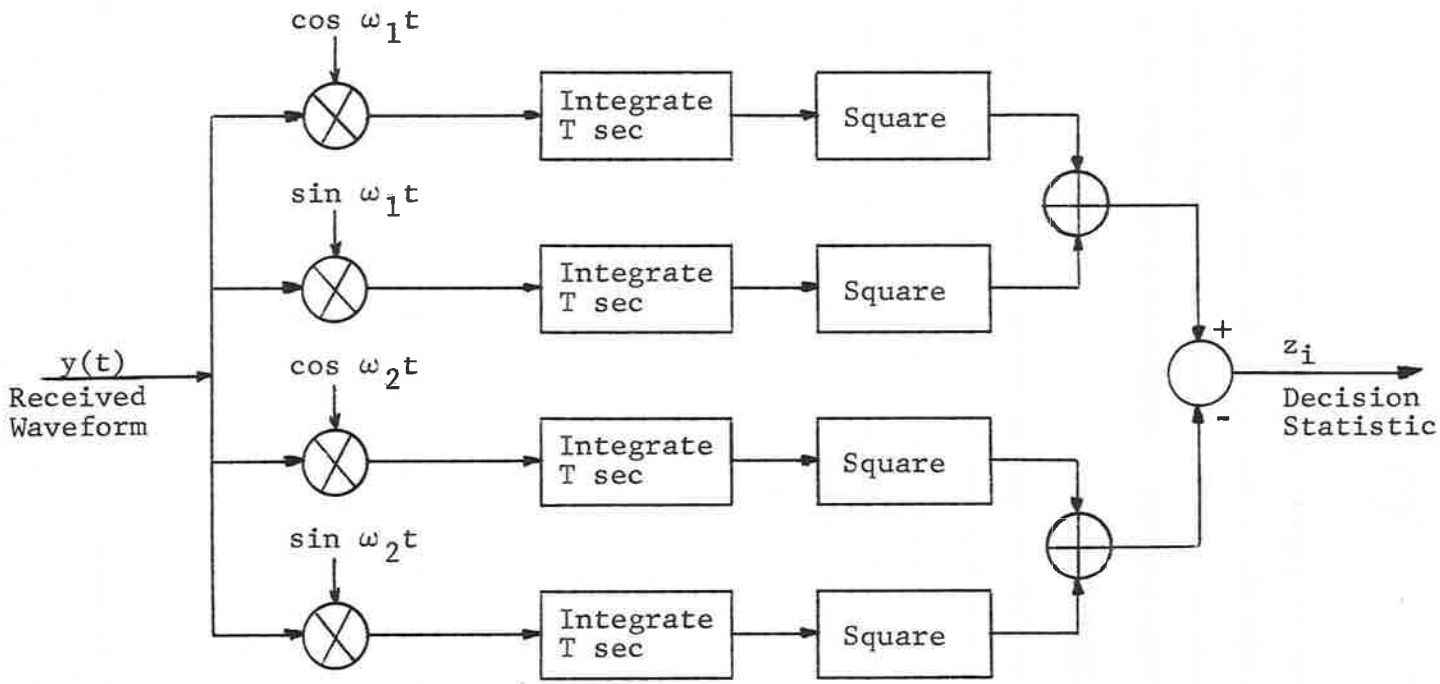

Confidence Value, $\alpha_i = |z_i|$

Binary Decision, $Y_i = 0$ if $z_i \geq 0$ (frequency ω_1 is assumed)
$= 1$ if $z_i < 0$ (frequency ω_2 is assumed)

Figure 5.2 Binary FSK Demodulation

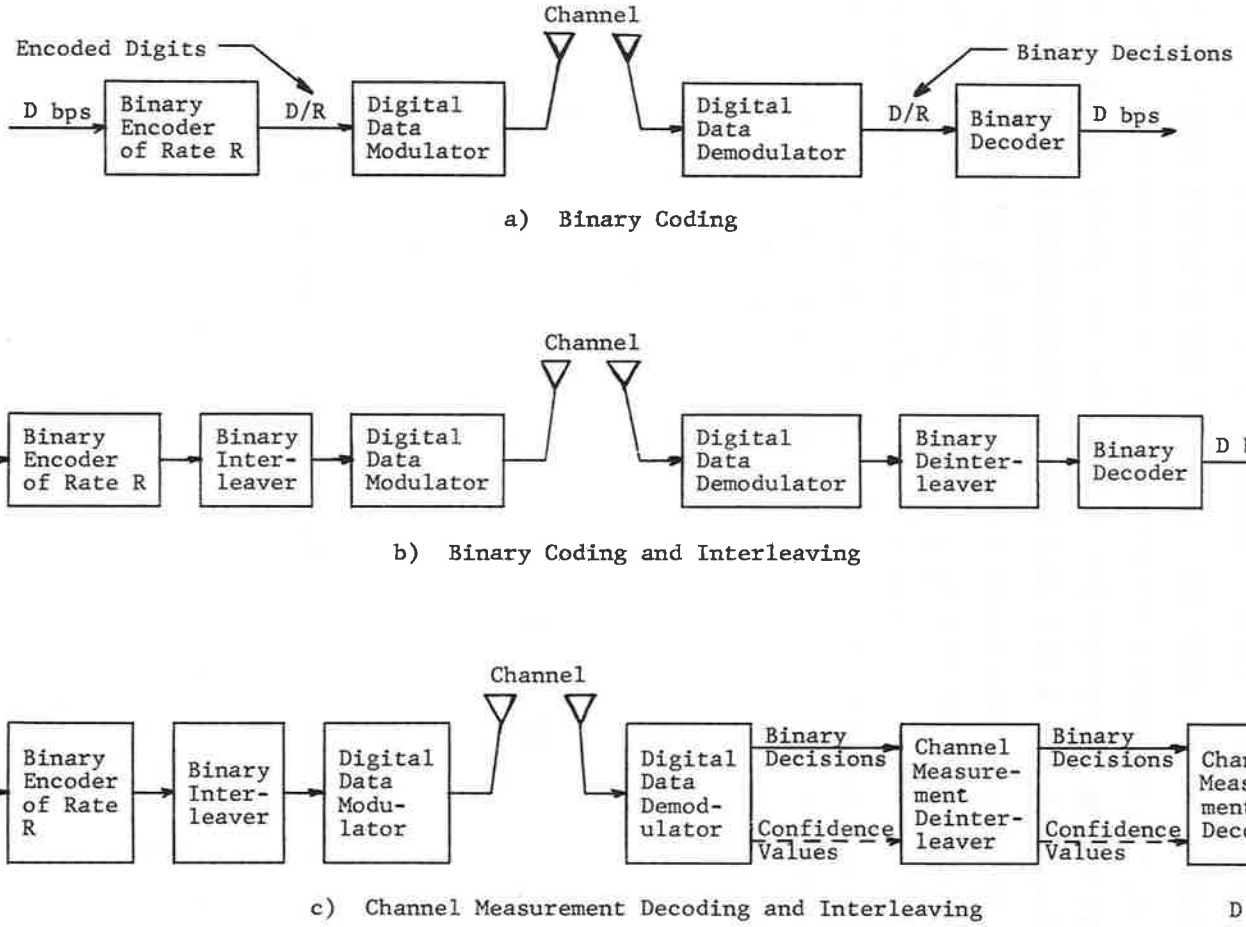

Figure 5.3 Interfacing of Coding and Modulation Processors

The data at D bps is encoded with a code of rate R so that input digit rate to the modulator is at D/R digits per second.

For DPSK the two-phase modulator will transmit a 180^{o} phase shift relative to the previous phase if the encoded digit is a 1, i.e., $X_i = 1$, otherwise no phase shift is transmitted. This type of encoding is attractive since only the phase of the previous baud is required for a bit decision. Unfortunately, errors tend to occur in pairs since a received statistic $\overline{W}_i$ is used to decode X_i, and as a reference for X_{i+1}. As the performance curves in Section 5.4 indicate, a conventional random error correction decoder will not be effective when errors are dependent. For DPSK we have a dependency of errors resulting from both DPSK modulation and the fact that the scatter components $\overline{S}_i$ are also correlated.

For FSK modulation there is still a dependence of errors due to the scatter components which is significant enough to limit the effectiveness of binary random error correcting codes.

5.2.4 Binary Coding and Interleaving

A considerable improvement in performance is possible by interleaving the uncoded binary data as indicated on Fig. 5.3b. Assuming the interleaving is such that the separation between code digits is large compared to the reciprocal of the channel's fading bandwidth,* channel errors within a given code block will be independent. The DPSK demodulator will still generate pairwise correlated errors, however, these errors will no longer be contained in the same code word.

---

*A separation equal to the reciprocal of the fading bandwidth can be shown by simulation to have negligible degradation when compared with the performance possible for statistical independent decision statistics.

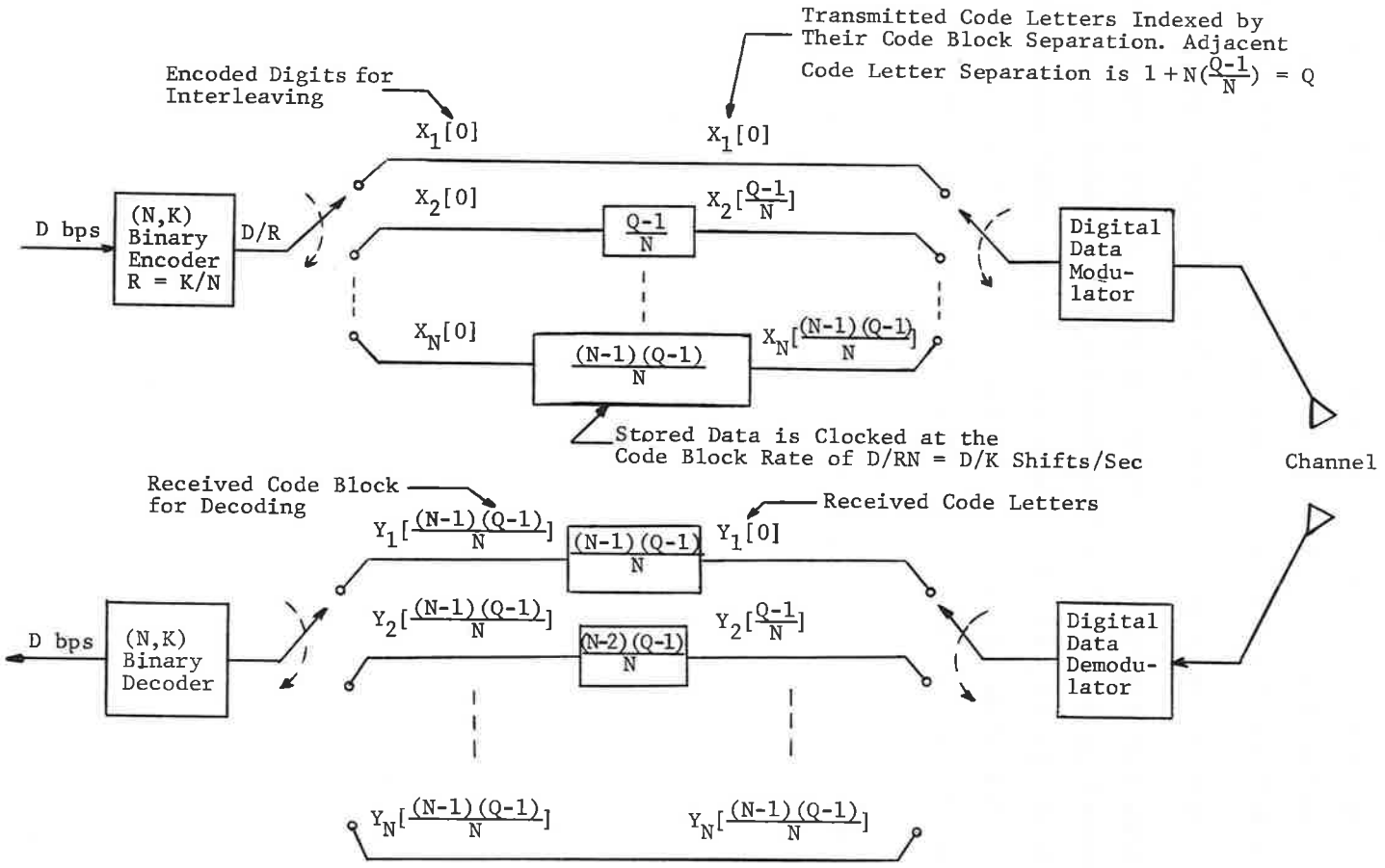

Total Decoding Delay = (N-1)(Q-1) Channel Digits

Q = Symbol Separation Between Adjacent Code Letters (Time Separation = $\frac{QR}{D}$)

Storage of Combined Transmitter and Receiver = (N-1)(Q-1) Bits

Figure 5.4 Periodic Interleaver/Deinterleaver

An efficient interleaver structure [5.5] is illustrated on Fig. 5.4. This structure is attractive since it requires no additional synchronization aside from code word sync and the storage is equal to the decoding delaying, and hence, is minimized.

5.2.5 Channel Measurement Decoding With Interleaving

An attractive approach for applying error correcting coding to this channel is to combine interleaving and channel measurement decoding [5.6], [5.7], [5.8]. The deinterleaver must now operate on quantized decision statistics, instead of binary decisions, and thus the storage at the receiver is increased as indicated on Fig. 5.3c.

A complex channel measurement decoder which correlates the received decision statistics with all possible 2^K code words $\underline{X}_m$ of block length N is obtained by selecting the code word which maximizes the expression below,

$$\sum_{i=0}^{N} z_i (-1)^{X_{m_i}} \tag{5.23}$$

where z_i is the decision statistic which for $\hat{X}_i = 0$ is positive and negative for $\hat{X}_i = 1$.

This rule is equivalent to selecting the code word which minimizes [5.6]

$$\sum_{i=1}^{N} \alpha_i (X_{m_i} \oplus Y_i) = \sum_{i=1}^{N} \alpha_i Z_{m_i} = W_\alpha (\underline{Z}_m) \tag{5.24}$$

where

$$\alpha_i = |z_i| \tag{5.25}$$

is called the confidence level of each received digit and $W_\alpha(\underline{Z}_m)$ is defined as the analog weight of the error pattern associated with a code word $\underline{X}_m$.

An efficient algorithm for approximating the performance of correlation channel measurement decoding is obtained by inverting all combinations of received binary associated with the $\left\lfloor \frac{d}{2} \right\rfloor$* lowest confidence levels to obtain additional code word estimates by feeding the perturbed binary sequence into a binary decoder. The code word selected in this small set, at most $2^{\left\lfloor \frac{d}{2} \right\rfloor}$ code words are considered and generally much less, is the code word of minimum analog weight. This algorithm can be described by the flow chart of Fig. 5.5, where $\underline{T}$ denotes a binary vector or test pattern, which contains some combination of 1's in the $\left\lfloor \frac{d}{2} \right\rfloor$ position of lowest confidence levels, and is added modulo-2 to the received binary vector $\underline{Y}$.

5.2.6 Channel Measurement Decoding of Multiple Rate Codes

An attractive alternative to interleaving block codes are multiple rate codes [5.9] which allow the correction of error bursts at later time intervals. Since these codes recognize when a burst occurs, the storage required for a given burst correction capability is generally less than that for interleavers. This is especially pronounced if channel measurement (soft decision) information is used in the decoding process since interleaving requires the storage of an entire frame of decision statistics before decoding, (which is composed of many code blocks) while multiple rate codes can be decoded after the storage of a set of decision statistics equal to that of only one code block.

---

*This number is the greatest integer less than or equal to one-half of the code's minimum distance d.

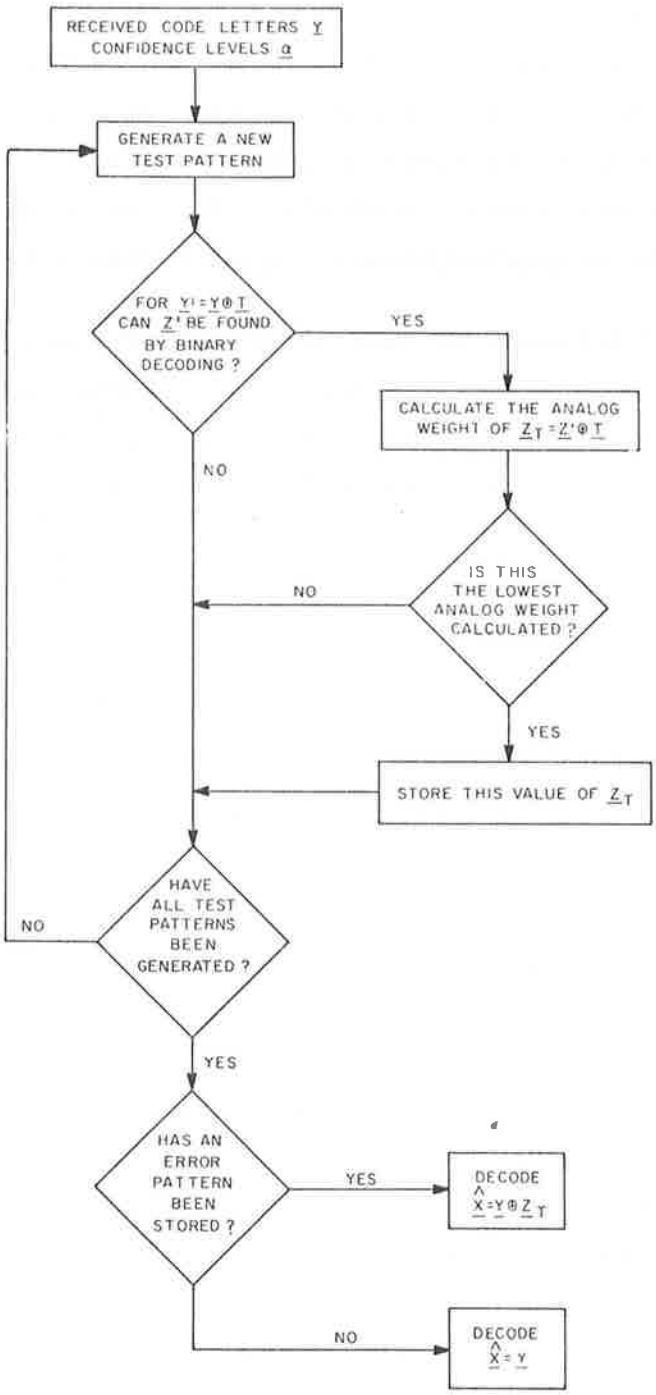

Figure 5.5 Flow Chart for Decoding With Channel Measurement Information

The encoding of a multiple rate code is illustrated on Fig. 5.6, and the decoding is shown on Fig. 5.7. A key property of these codes is that only the past binary data need be stored for decoding a new block of data with channel measurement information.

We have been able to show that error propagation will not exist if the criterion for declaring a burst is such that the analog weight of the selected error pattern is less than the weight of the lowest t channel measurement values, where t is less than or equal to the minimum distance of the high rate code [5.9]. To make this point more concrete consider a high rate code whose combined generating matrix* is given on Fig. 5.8. Figure 5.9 is the actual generating matrix for the optimum (24,12) to (24,18) code. Note that for that basic (24,12) code the number of syndromes is 2^{12}, which is less than the number of patterns of four errors. Thus, a minimum distance 9 code cannot exist, providing that d=8 is the maximum-minimum distance for this code. A similar argument holds for the high rate (24,18) code whose minimum distance is 4.

Using this multiple rate code, it is guaranteed [5.9] that we will not have error propagation if a burst is declared if the analog weight of the selected error pattern $\underline{Z}$ given by

$$W_\alpha(\underline{Z}) = \sum_{i=1}^{N} Z_i \alpha_i \tag{5.26}$$

is greater than a threshold given by the sum of the t lowest channel measurement values, i.e.,

$$\text{Threshold} = \sum_{i=1}^{t} \alpha_i \tag{5.27}$$

where $t \leq d = 4$ for the (24,12) to (24,18) multiple rate code.

*All the code words of an (N,K) linear code are linear combinations of row vectors of its generator matrix.

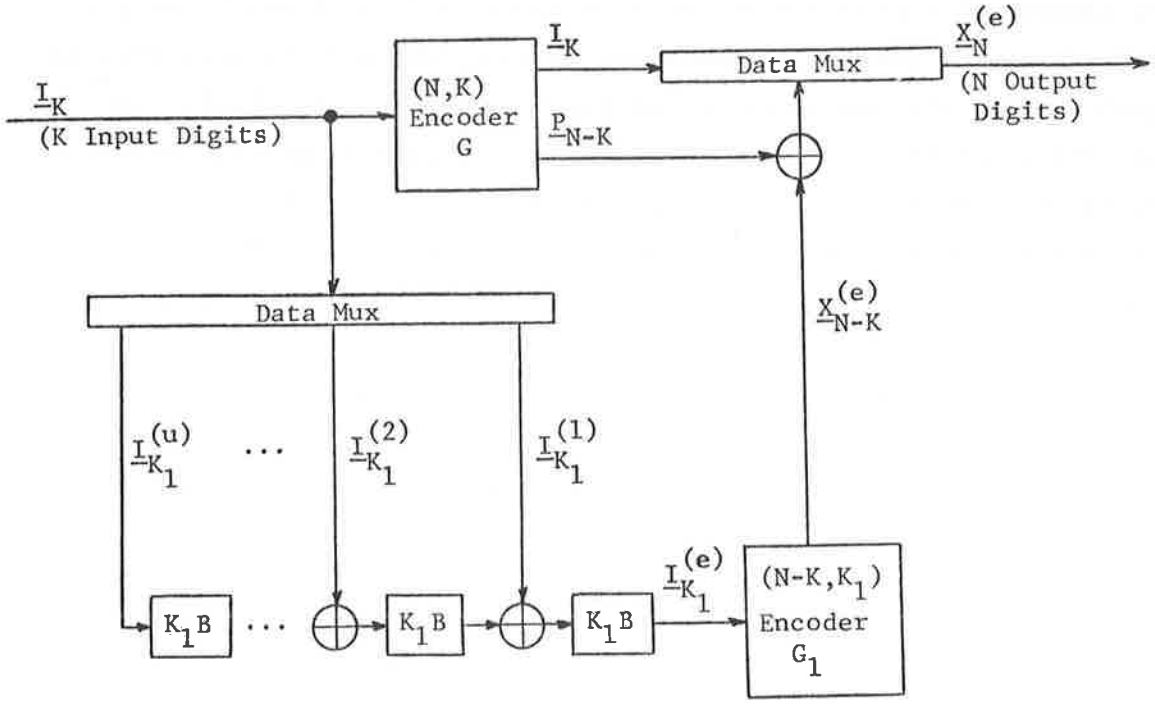

Basic Rate = $K/N = R$
$u = K/K_1$ - Folding Factor
High Rate = $(K+K_1)/N = R(1+u)$
B = Number of blocks of burst protection

Figure 5.6 Block Diagram of a Multiple Rate Encoder

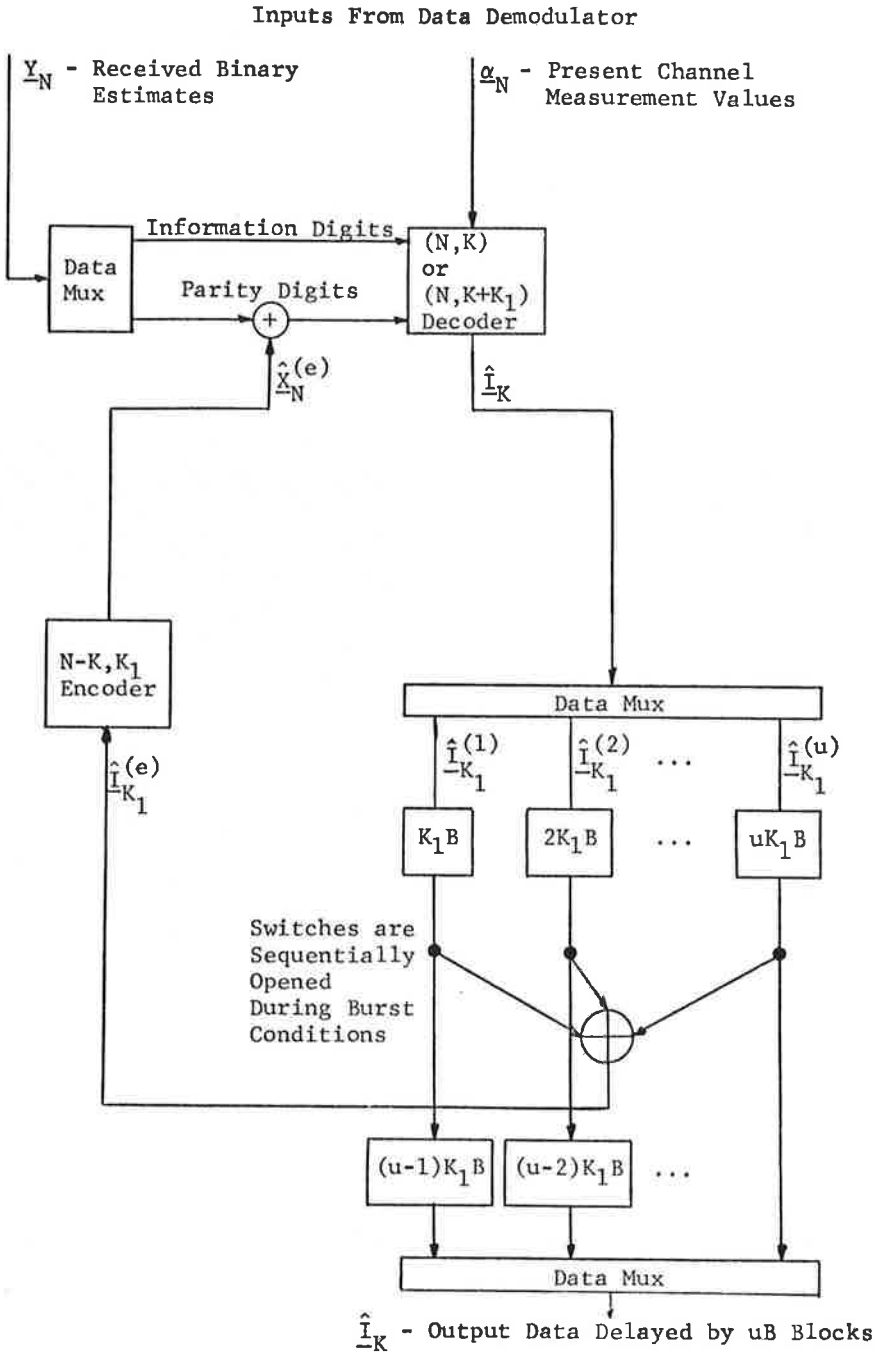

Figure 5.7 Block Diagram of a Multiple Rate Decoder

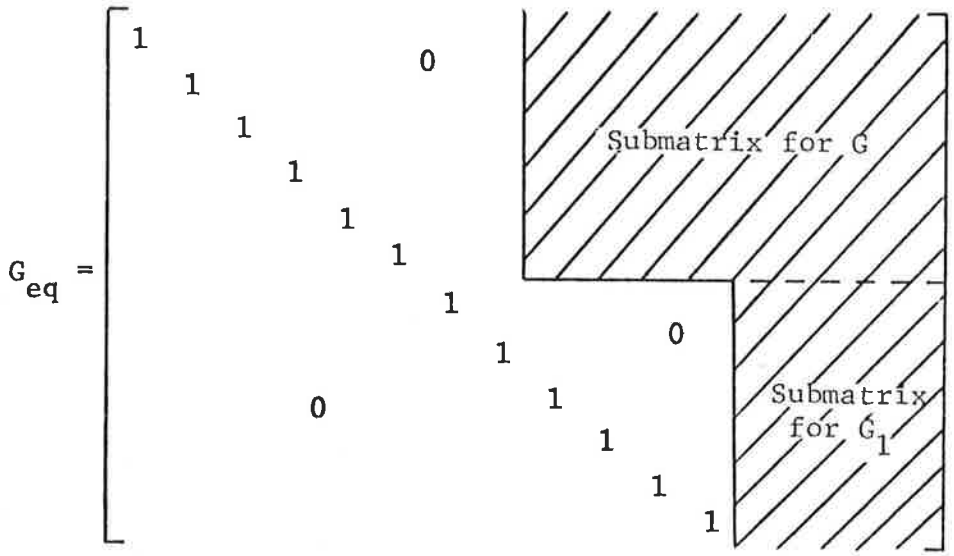

Figure 5.8 Generating Matrix for High Rate Code

$$G_{eq} = \left[\begin{array}{cccccccccccc|cccccccccccc}
1 & & & & & & & & & & & & 1 & 0 & 1 & 0 & 1 & 1 & 1 & 0 & 0 & 0 & 1 & 1 \\
 & 1 & & & & & & & & & & & 1 & 1 & 1 & 1 & 1 & 0 & 0 & 1 & 0 & 0 & 1 & 0 \\
 & & 1 & & & & & & & & & 0 & 1 & 1 & 0 & 1 & 0 & 0 & 1 & 0 & 1 & 0 & 1 & 1 \\
 & & & 1 & & & & & & & & & 1 & 1 & 0 & 0 & 0 & 1 & 1 & 1 & 0 & 1 & 1 & 0 \\
 & & & & 1 & & & & & & & & 1 & 1 & 0 & 0 & 1 & 1 & 0 & 1 & 1 & 0 & 0 & 1 \\
 & & & & & 1 & & & & & & & 0 & 1 & 1 & 0 & 0 & 1 & 1 & 0 & 1 & 1 & 0 & 1 \\
 & & & & & & 1 & & & & & & 0 & 0 & 1 & 1 & 0 & 0 & 1 & 1 & 0 & 1 & 1 & 1 \\
 & & & & & & & 1 & & & & & 1 & 0 & 1 & 1 & 0 & 1 & 1 & 1 & 1 & 0 & 0 & 0 \\
 & & & & & & & & 1 & & & & 0 & 1 & 0 & 1 & 1 & 0 & 1 & 1 & 1 & 1 & 0 & 0 \\
 & & & & & & & & & 1 & & 0 & 0 & 0 & 1 & 0 & 1 & 1 & 0 & 1 & 1 & 1 & 1 & 0 \\
 & & & & & & & & & & 1 & & 1 & 0 & 1 & 1 & 1 & 0 & 0 & 0 & 1 & 1 & 0 & 1 \\
 & & & & & & & & & & & 1 & 0 & 1 & 0 & 1 & 1 & 1 & 0 & 0 & 0 & 1 & 1 & 1 \\
\hline
 & & & & & & & & & & & & 1 & & & & & & 0 & 1 & 0 & 1 & 1 & 0 \\
 & & & & & & & & & & & & & 1 & & 0 & & & 1 & 1 & 1 & 0 & 1 & 1 \\
 & & & & & & & & & & & 0 & & & 1 & & & & 1 & 0 & 1 & 1 & 1 & 1 \\
 & & & & & & & & & & & & & & & 1 & & & 1 & 1 & 0 & 0 & 1 & 0 \\
 & & & & & & & & & & & & & 0 & & & 1 & & 1 & 1 & 1 & 0 & 0 & 0 \\
 & & & & & & & & & & & & & & & & & 1 & 1 & 0 & 1 & 0 & 1 & 0 \\
 & & & & & & & & & & & & & & & & & & 1 & 0 & 1 & 0 & 1 & 0 & 1
\end{array}\right]$$

$$\sum_{i=0}^{4} \binom{24}{i} > 2^{12} \Rightarrow \text{d=8 is the maximum minimum distance for a (24,12) code}$$

$$\sum_{i=0}^{2} \binom{24}{i} > 2^{6} \Rightarrow \text{d=4 is the maximum minimum distance for a (24,18) code}$$

Figure 5.9 Generating Matrix of a (24,18) Distance 4 Code With the (24,12) Golay Code as a Subset

Performance may be improved with higher thresholds, that is $t > 4$. However, we do not have analytical results at this time which guarantee no error propagation for higher thresholds.

5.3 GENERAL ANALYTICAL RESULTS

In this section expressions for straight modulation and for certain combined modulation and coding approaches will be presented. These expressions will be combined with the simulated results in the following section which contains error probability curves.

5.3.1 Error Probability for DPSK and FSK

For DPSK or FSK the expression for the slow fading Rician channel [5.4] with Mth order diversity can be modified to include the effects of coding and fast fading as indicated in Section 5.2 to yield:

$$p = \frac{1}{2+D}\exp\left(-\frac{S}{2+D}\right)\left[1 - \frac{D}{2}\sum_{j=1}^{M-1}\binom{2j}{j}\left(\frac{\sqrt{1+D}}{2+D}\right)^{2j}\right.$$

$$\left. + \sum_{m=1}^{M-1}\frac{S^m}{(1+D)^m(2+D)^m\, m!}\sum_{j=m}^{M-1}\binom{2j}{j+m}\left(\frac{\sqrt{1+D}}{2+D}\right)^{2j}\frac{2m-(j-m)D}{2j}\right], \tag{5.28}*$$

where

$$D = RE_b/(\gamma N_0) \text{ - FSK}, \qquad D = 2RE_b/(\gamma N_0 + (1-\rho)RE_b) \text{ - DPSK} \tag{5.29}$$

$$S = M\gamma D \text{ - FSK}, \qquad S = M\gamma D \text{ - DPSK} \tag{5.30}$$

and M is the order of diversity.

For an uncoded system with a single diversity signaling format the above can be evaluated at R=1 and M=1*. The diversity results will be shown useful in estimating the performance of a coded system when operating in a single diversity mode.

*For M=1, Eq. (5.28) becomes: $p = \frac{1}{2+D}\exp\left(-\frac{S}{2+D}\right)$.

5.3.2 Binary Decoding Error Probability With Interleaving

It is difficult to obtain useful expressions for decoding when we have dependent errors, and thus, only the case where error occurs independently will be analyzed.

Assume first that the minimum distance of the code is even. Thus d/2 raw bit errors in a block of N bits will be detected and all error patterns of less than d/2 errors will be corrected. Since the code can correct up to

$$e = \frac{d}{2} - 1 \tag{5.31}$$

errors at most e additional errors will be made if the decoder decodes incorrectly. Thus, an upper bound on the probability of bit error Pe is given by

$$Pe \leq \frac{1}{N}\left[\frac{d}{2}\Pr\left(\frac{d}{2}\text{ raw bit error}\right) + \sum_{i > \frac{d}{2}}^{N} (i+e)\Pr(i\text{ raw bit error})\right] \tag{5.32}$$

where

$$\Pr(i\text{ raw bit error}) = \binom{N}{i} p^i (1-p)^{N-i} \tag{5.33}$$

and p is the probability of a raw bit error such as given by (5.28).

Substituting (5.33) into (5.32) yields

$$Pe \leq \frac{d}{2N}\binom{N}{d/2} p^{d/2}\left[(1-p)^{N-\frac{d}{2}} + \sum_{i > \frac{d}{2}}^{N} \binom{N-\frac{d}{2}}{i-\frac{d}{2}} p^{i-\frac{d}{2}} (1-p)^{N-i} \beta_i\right] \tag{5.34}$$

where

$$\beta_i = \frac{(i+e)2}{d\binom{i}{d/2}} \tag{5.35}$$

and the identity

$$\binom{N}{i} = \binom{N-d/2}{i-d/2}\binom{N}{d/2}\frac{1}{\binom{i}{d/2}} \tag{5.36}$$

is used to obtain (5.34), which can be further upper bounded by bounding β_i by 1. Note that β_i is monotonically decreasing with

$$\beta_{\frac{d}{2}+1} = \frac{2}{\frac{d}{2}+1} \leq 1 \tag{5.37}$$

for all non-trivial codes with $d \geq 2$. Using the above bound and letting $j = i - d/2$ in (5.34) yields

$$Pe \leq \frac{d}{2N}\binom{N}{d/2}p^{d/2}\left[(1-p)^{N-d/2} + \sum_{j=1}^{N-d/2}\binom{N-d/2}{j}p^j(1-p)^{N-\frac{d}{2}-j}\right] \tag{5.38}$$

Since the term in brackets is equal to 1 we have

$$Pe \leq \frac{d}{2N}\binom{N}{d/2}p^{d/2} \tag{5.39}$$

A lower bound is given by

$$Pe \geq \frac{1}{N}\left[\frac{d}{2}\Pr\left(\frac{d}{2}\text{ raw errors}\right)\right] = \frac{d}{2N}\binom{N}{d/2}p^{d/2}(1-p)^{N-d/2} \tag{5.40}$$

which combined with (5.39) gives tight estimates as the value of p decreases.

For a code of odd minimum distance the error correcting capability of the code is given by

$$e = \frac{d-1}{2} \tag{5.41}$$

When there are e+1 errors in a code word there is a probability δ that the pattern will not be detected. When a pattern is detected no additional errors will be added, but e additional errors will be added if the pattern is not detected. An expression for δ is obtained by noting that for each code word of minimum distance d away from the transmitted code word $\binom{d}{e+1}$ patterns of e+1 errors will be undetected. Since there are a total of $\binom{N}{e+1}$ error patterns with e+1 errors, we have

$$\delta = \frac{(n_d)\binom{d}{e+1}}{\binom{N}{e+1}} \tag{5.42}$$

where n_d is the number of code words of minimum distance d. Following similar argument to those used for codes of even minimum distance we obtain

$$Pe \leq [\delta d + (1-\delta)(\tfrac{d+1}{2})] \binom{N}{\frac{d+1}{2}} p^{\frac{d+1}{2}} \tag{5.43}$$

and

$$Pe \geq [\delta d + (1-\delta)(\tfrac{d+1}{2})] \binom{N}{\frac{d+1}{2}} p^{\frac{d+1}{2}} (1-p)^{N - \frac{d+1}{2}} \tag{5.44}$$

which supply tight upper and lower bounds.

For correlation channel measurement decoding as well as the algorithm previously presented it can be shown that [5.6]

$$Pe < \binom{N}{d} Pe(\text{dth order diversity}) \tag{5.45}$$

A lower bound given by

$$Pe > \frac{d}{N} n_d p^d (1-p)^{N-d} \tag{5.46}$$

can readily be obtained by noting that with the appropriate d error patterns undetected errors must occur for all n_d code words of distance d away from the transmitted code word.

With the aid of union bound arguments, [5.10], we can upper bound Pe also by

$$Pe < 2^K Pe(\text{dth order diversity}) \tag{5.47}$$

and lower bound Pe by

$$Pe > \frac{d}{N} Pe(\text{dth order diversity}) \tag{5.48}$$

Note the probability of error between code words which differ in d places is exactly equal to the probability of error for dth order diversity.

In addition to the four bounds given above an approximate result given by

$$Pe \approx \frac{d}{N} n_d Pe(\text{dth order diversity}) \tag{5.49}$$

will be useful in estimating the performance of channel measurement decoding algorithms. This approximation is based on using only the largest n_d terms in the union bound which corresponds to the n_d code words of minimum distance d and neglecting the probability of an error for the other $(2^K - n_d)$ code words.

5.4 DISCUSSION OF PERFORMANCE RESULTS

In this section error probability curves as a function of E_b/N_0 will be presented with the ratio of direct-to-scatter energy γ as a parameter varying in the range from 0 dB to ∞. A fading bandwidth of 120 Hz and a data rate of 1200 bps will be assumed for all curves presented. This corresponds to a correlation coefficient between successive signaling pulses of $\rho = .9526$ for uncoded data at D = 1200 bps, and $\rho = .9878$ for coded data which is encoded with a rate 1/2 code to give a channel digit rate of 2400 digits/sec.

To illustrate the effectiveness of error correcting coding, when appropriately applied, a (24,12) Golay code of minimum distance d=8 is used. Performance improvements beyond those illustrated should be possible if more effectiveness, and more complex, error correcting codes are used. Also, the multiple rate coding approach has potential to offer significant performance gains, while minimizing decoding delay and storage requirements. Nevertheless, the results to be presented will illustrate clearly the enormous gains in performance which are possible if error correcting coding is used properly.

Figure 5.10 illustrates the error performance for a single diversity uncoded two-phase DPSK modulation format. The curves presented are obtained directly from Eq. (5.28) where $\rho = .9526$ and the parameter γ is chosen as 0 dB, 4 dB, 8 dB, and ∞. A similar set of curves for single diversity FSK is given by Fig. 5.11. For

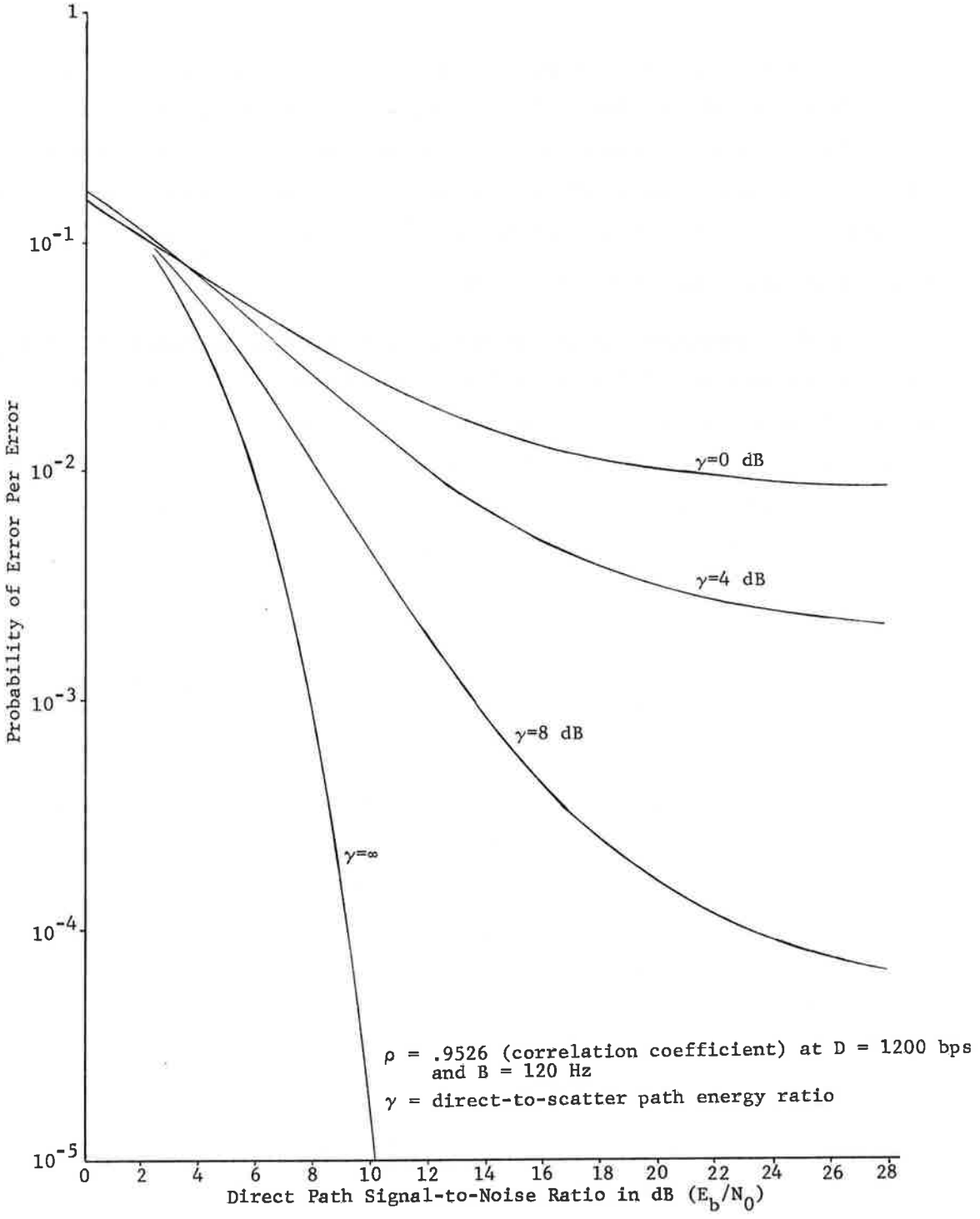

Figure 5.10 Performance Curve for Rician Channel Using DPSK Modulation and No Coding

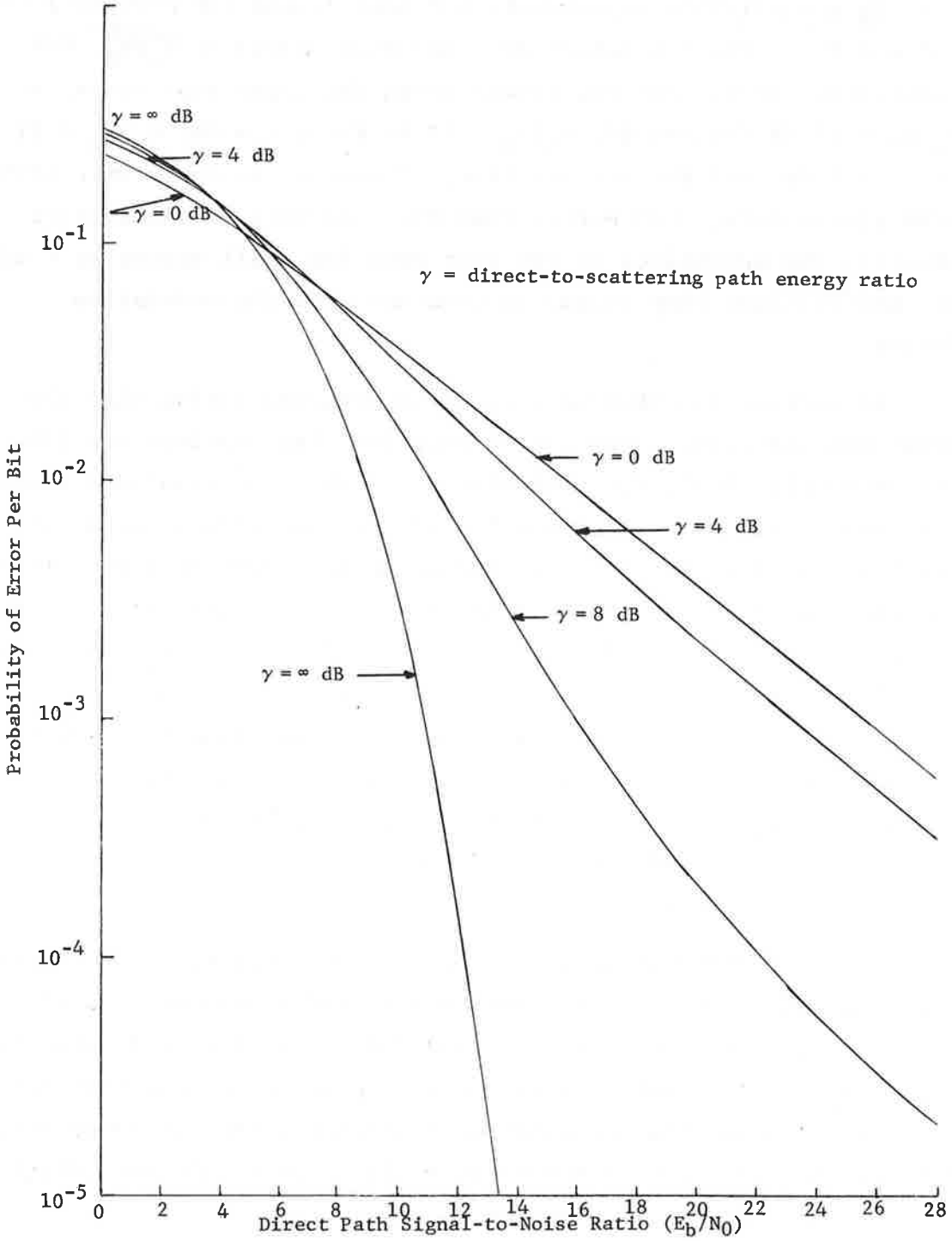

Figure 5.11 Performance Curves for Rician Channel Using FSK Modulation and No Coding

ρ = .9526 negligible adjustments for fast fading are necessary for FSK and thus, for low values of γ and high values of E_b/N_0, FSK outperforms DPSK. For the curves shown the cross over occurs at E_b/N_0 = 13 dB for γ=0 dB, E_b/N_0 = 17 dB for γ = 4 dB, E_b/N_0 = 21 dB for γ = 8 dB, and for γ = ∞we have, of course, no cross over with DPSK always doing 3 dB better than FSK. As will be illustrated shortly, the advantages of FSK over DPSK for small values of γ will be non-existent when coding is combined with the modulation format.

In Section 5.2 various ways of interfacing coding with the modem was discussed. The performance for these options are illustrated on Fig. 5.12, for DPSK with γ = 0 dB. The simulated results for binary decoding illustrate how ineffective coding can be if not interfaced properly. Even channel measurement decoding without interleaving offers only a slight gain over no coding at all. The effectiveness of channel measurement decoding with interleaving is clearly evident from this figure. Furthermore, for the minimum distance 8 Golay code, the channel measurement decoding algorithm presented in Section 5.3 is quite practical in that the $2^{(d/2)} = 16$ iterations required of the binary decoder can be done by serial processing at a complexity of less than a factor of 2 over a conventional binary decoder.*

When DPSK modulation is used with binary decoding and interleaving, the effects of fast fading are hardly evident even at a probability of bit error of 10^{-5} and for γ = 0 dB as indicated on Fig. 5.13. These coding results are obtained by noting that for the (24,12) Golay code an exact expression for the bit error probability can readily be obtained from the codes weight distribution [5.11]. The first few terms are given by

*Based on present CNR hardware designs.

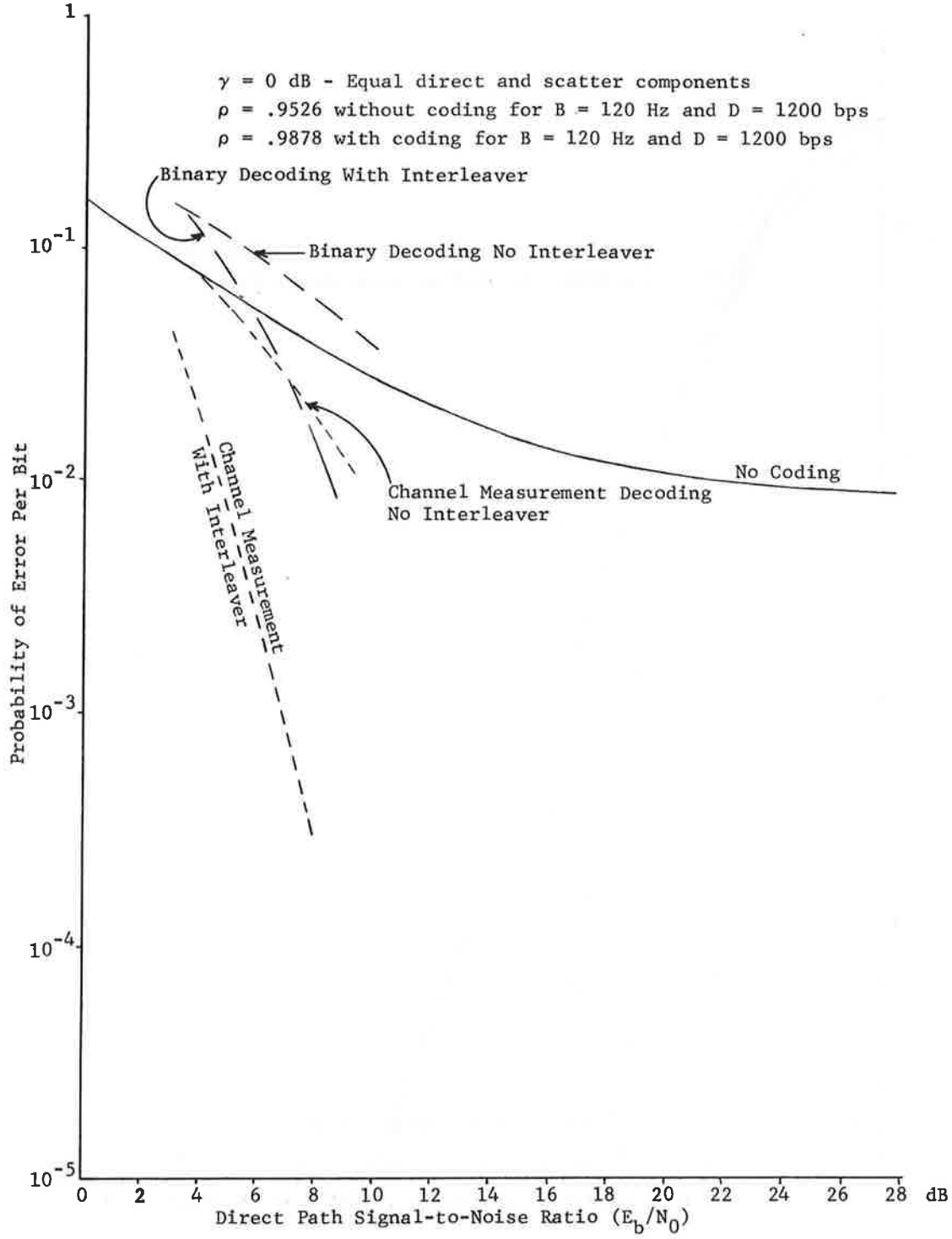

Figure 5.12 Performance for Rician Channel Using DPSK Modulation and (24, 12) Golay Code with and without Interleaving

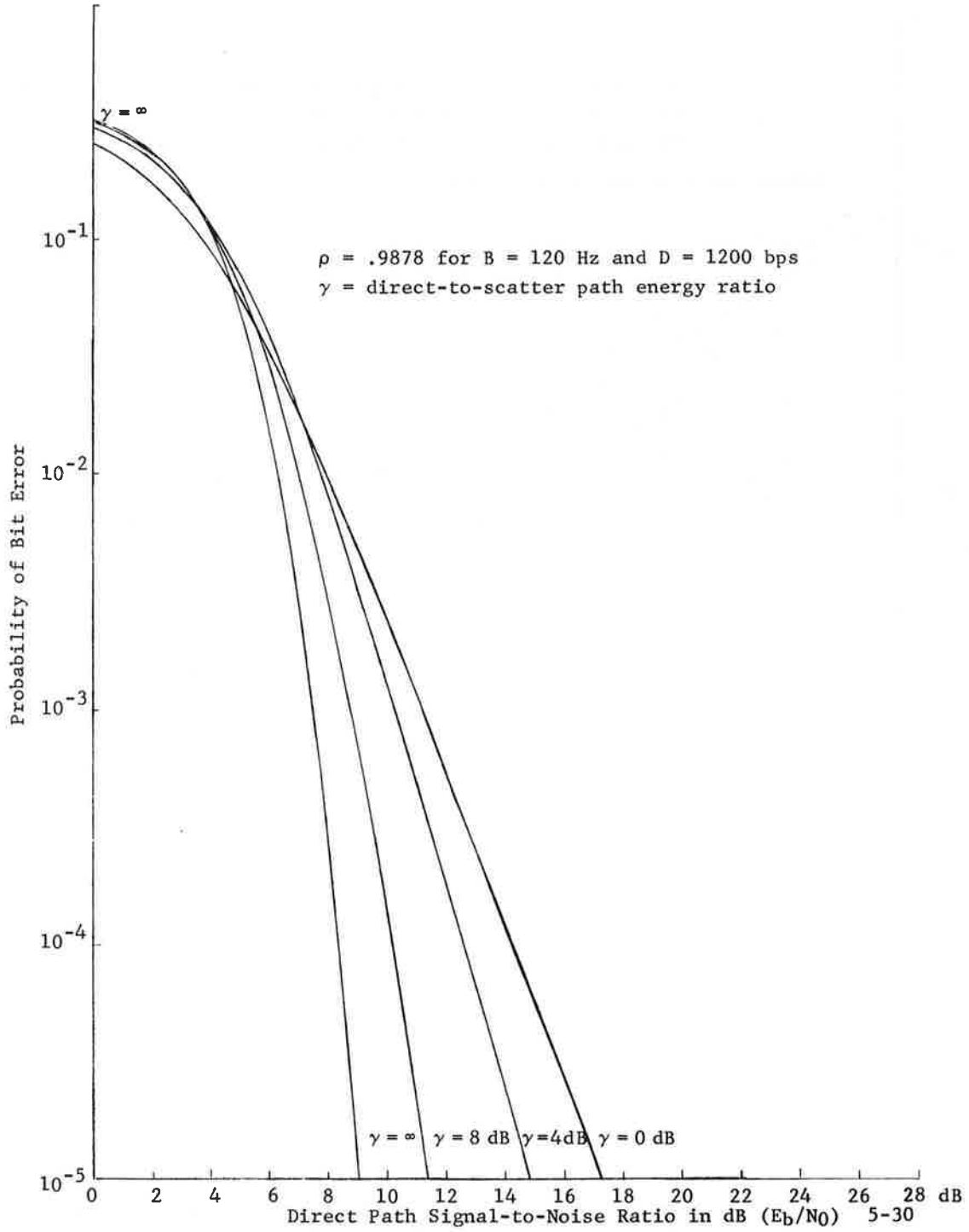

Figure 5.13 Performance Curve for Rician Channel Using DPSK Modulation and (24, 12) Golay Code. Interleaved Binary Decoding

$$Pe = \frac{4}{24}\binom{24}{4}p^4(1-p)^{20} + \frac{8}{24}\binom{25}{5}p^5(1-p)^{19}$$

$$+ \left\{\frac{6}{24}\left[\binom{24}{6} - 759\binom{8}{2}\right] + \frac{8}{24}(759)\binom{8}{2}\right\}p^6(1-p)^{18}$$

$$+ \frac{8}{24}\binom{24}{8}p^8(1-p)^{16} + \ldots \qquad (5.50)$$

The bounds presented in Section 5.3 are given by

$$\frac{4}{24}\binom{24}{4}p^4(1-p)^{20} < Pe < \frac{4}{24}\binom{24}{4}p^4 \qquad (5.51)$$

and actually are quite adequate for values of p below 10^{-2}. The value of p is obtained from Eq. (5.28), where R = 1/2, and ρ = .9878, M = 1 and γ is a selected parameter.

A similar set of curves are given by Fig. 5.14 for FSK with interleaver binary decoding.

While for the fast fading Rician channel, there exists a value of E_b/N_0 above which FSK with coding will be superior to DPSK with coding, the error probability associated at which this occurs is considerably below 10^{-5}. In fact, the results presented in Sections 5.2 and 5.3 can be used to obtain this minimum value of Pe. Note that as $E_b/N_0 \to \infty$, the equivalent SNR for DPSK given by (5.22) is limited to

$$\left(\frac{E_b}{N_0}\right)_{eq} \to \frac{\gamma}{1-\rho} \qquad (5.52)$$

which for γ=1 (0 dB) and ρ = .9878 is 19.1 dB. Using Eq. (5.28) we have p limited to 2.24×10^{-3}. However, for the binary Golay decoder from Eq. (5.51) we have

$$Pe \leq 1771\ p^4 = 4.46 \times 10^{-8} \qquad (5.53)$$

and thus the irreducible error for interleaving binary decoding and DPSK modulation is at a quite acceptable value.

The picture is even better when channel measurement decoding is combined with DPSK modulation and interleaving. Figure 5.15 presents actual computer simulated results for the algorithm presented

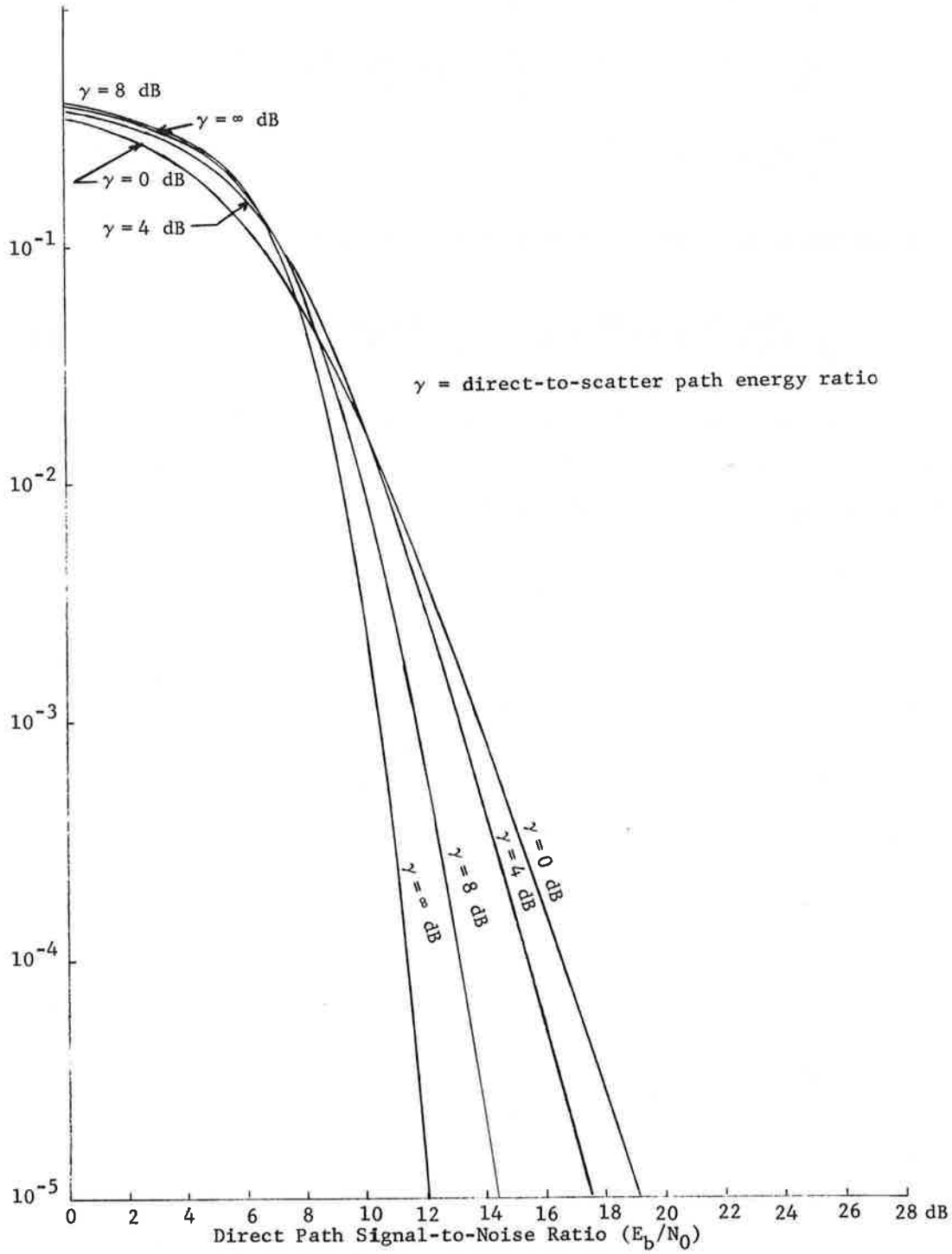

Figure 5.14 Performance Curve for Rician Channel Using FSK Modulation and (24, 12) Golay Code. Interleaved Binary Decoding

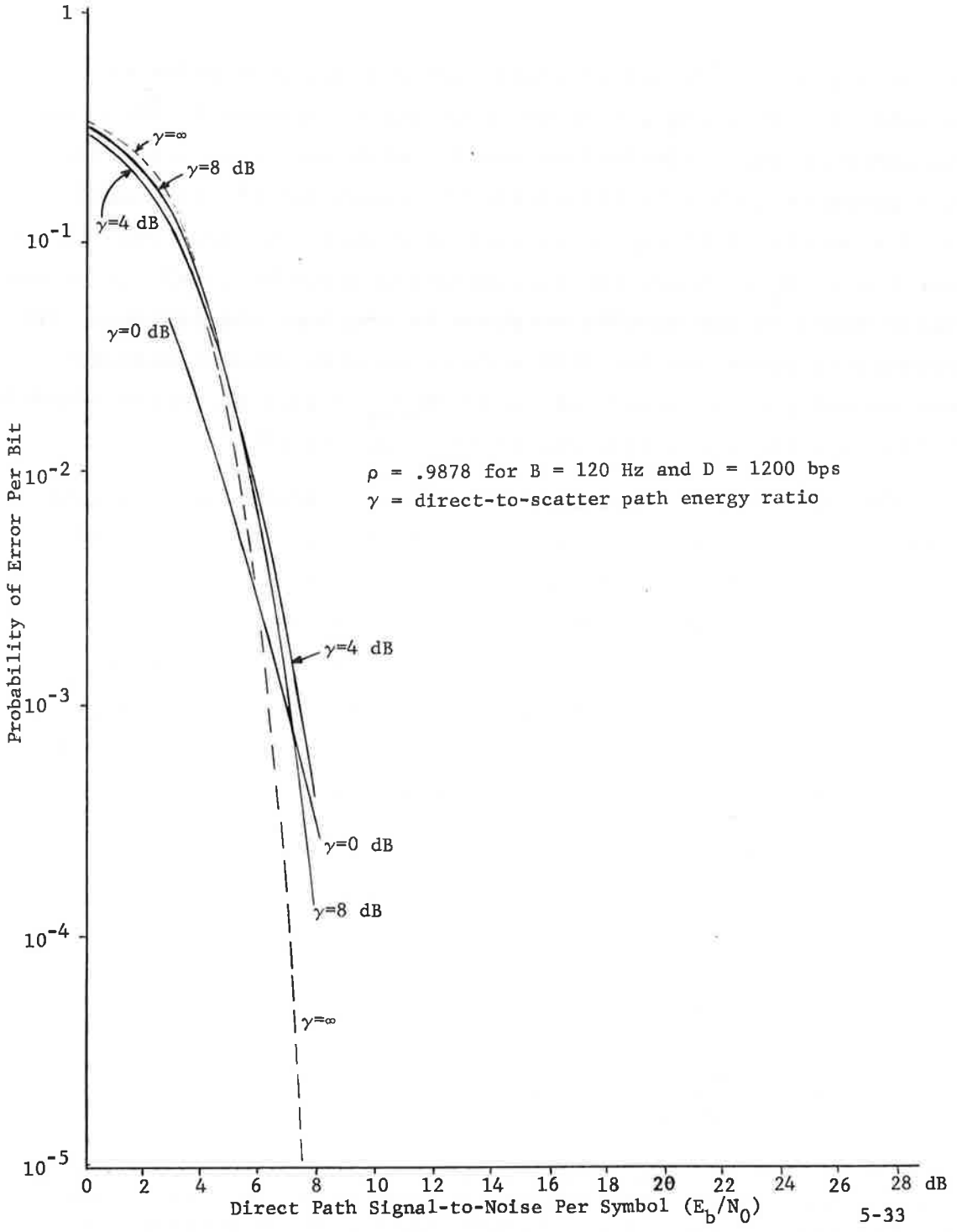

Figure 5.15 Simulated Performance Curves for Rician Channel Using DPSK Modulation and (24, 12) Golay Code. Interleaved Channel Measurement Decoding

in Section 5.2. A complete binary decoder was used which was capable of correcting 1/6 of the four error patterns.* The close agreement of these simulations results with the error approximation given by (5.49) is illustrated by comparing the simulated results on Fig. 5.15 to the analytical results on Fig. 5.16. Note that for $E_b/N_0 >$ 4 dB, the approximation given by (5.49) is essentially equal to the results obtained by computer simulations. The irreducible error now for DPSK modulation with channel measurement decoding still occurs at an $(E_b/N_0)_{eq}$ = 19.1 dB for γ=0, which by (5.49) is quite negligible and in the range of 10^{-14}.

The estimated error performance for FSK modulation and interleaved channel measurement decoding obtained by Eq. (5.49) and Eq. (5.28), is illustrated on Fig. 5.14. Clearly, upon comparing Fig. 5.16 to 5.17 any advantage that FSK modulation may have over DPSK modulation when no coding is used, is non-existent when interleaved channel measurement decoding is utilized. In fact, a clear 3 dB advantage is gained by using interleaver channel measurement decoding, with DPSK rather than FSK modulation.

---

*For a straight binary decoded, since only

$$\left[\frac{2^{12} - \sum_{i=0}^{3} \binom{24}{i}}{\binom{24}{4}} = \frac{1}{6}\right]$$

of the four errors can be corrected 5/6 of the time, four errors will be added rather than corrected. While a complete decoder is not the best strategy for a binary decoder it is desirable for a channel measurement decoder which ideally will not select incorrect error patterns because of their relative high analog weight.

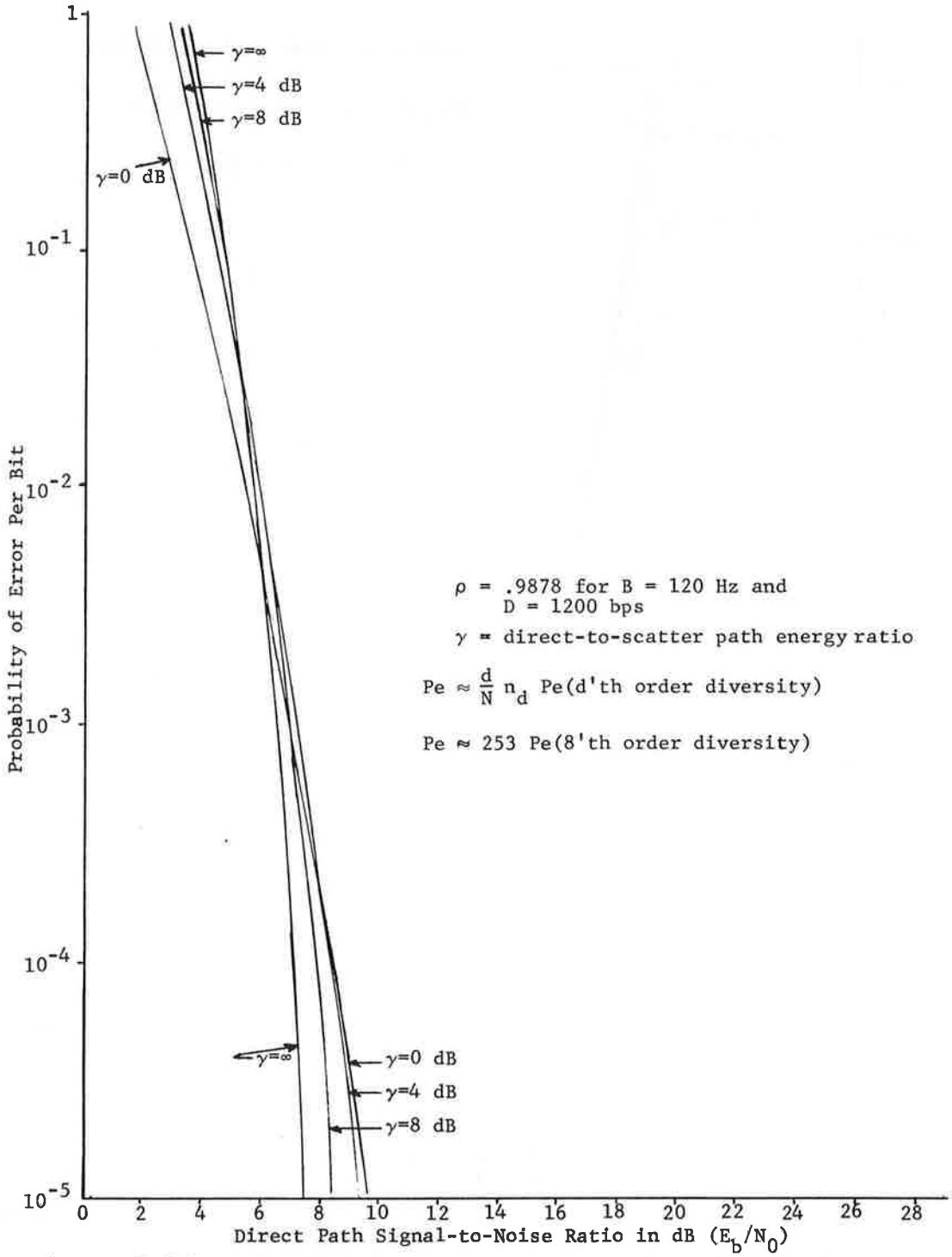

Figure 5.16 Estimated Performance Curve for Rician Channel Using DPSK Modulation and (24, 12) Golay Code. Interleaved Channel Measurement Decoding

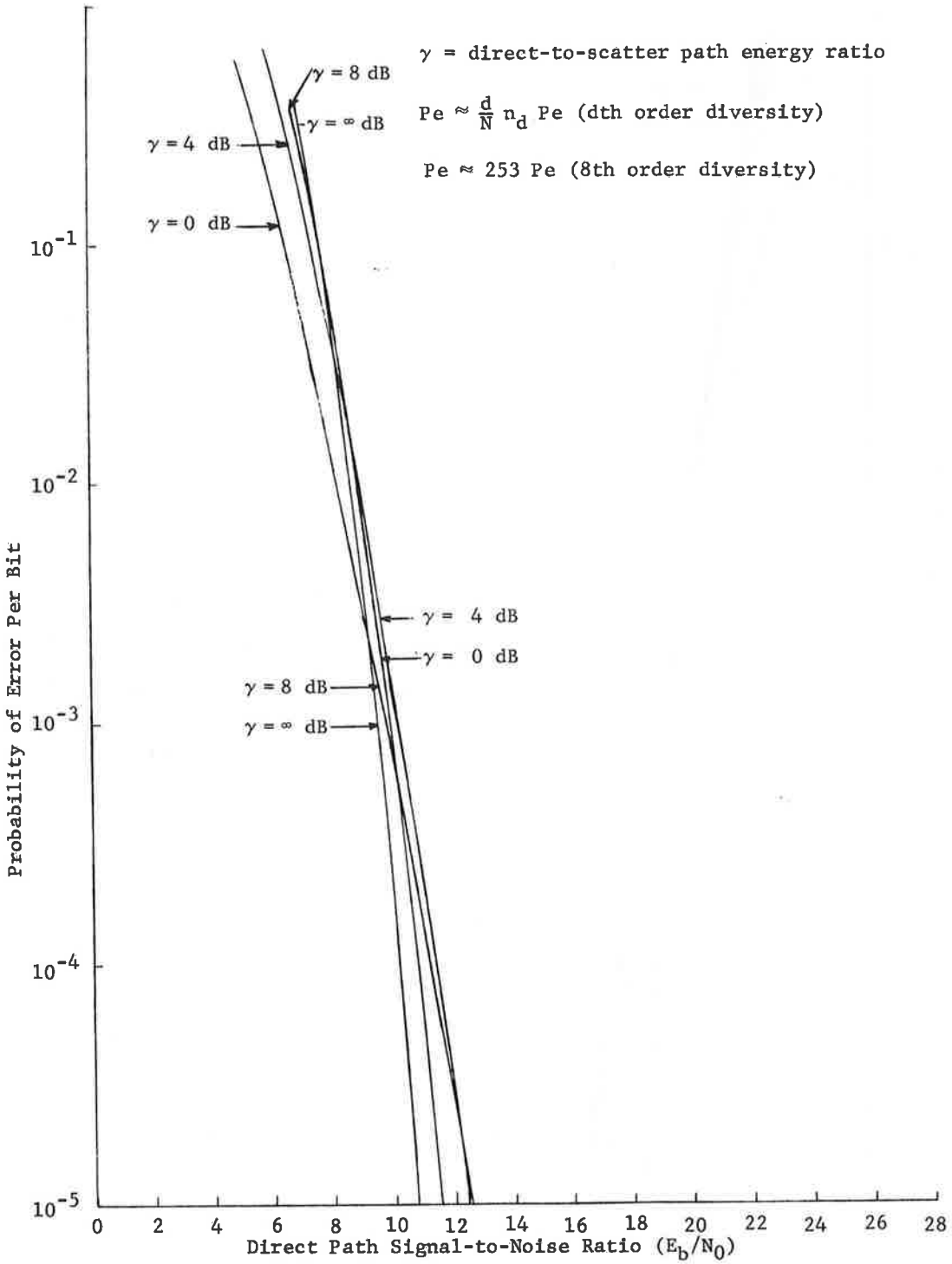

Figure 5.17 Estimated Performance Curves for Rician Channel Using FSK Modulation and (24, 12) Golay Code. Interleaved Channel Measurement Decoding

One of the most attractive features of channel measurement decoding is illustrated on Fig. 5.16 where an error probability of 10^{-5} can be obtained for

$$7.5 \text{ dB} \leq \frac{E_b}{N_0} \leq 9.5 \text{ dB} \tag{5.54}$$

with the channel's direct-to-scatter ratio varying over the range

$$0 \text{ dB} \leq \gamma \leq \infty \tag{5.55}$$

This small 2 dB variation in E_b/N_0 is quite remarkable, considering that for DPSK with interleaved binary decoding a 9 dB variation is required, and an error rate of 10^{-5} can not be achieved over this range of γ regardless of E_b/N_0 when coding is not used.

While the (24,12) Golay code may not necessarily be the code selected for the aeronautical channel, one can conclude from these results that for a direct-to-scatter energy ratio $\gamma \geq 0$ dB, a bit error probability of 10^{-5} or less can be achieved when $E_b/N_0 \geq 9.5$ dB, which corresponds to a $C/KT = Pr/N_0 \geq 40.3$ dB at a data rate of 1200 bps. Even though these results were obtained for a fading bandwidth of 120 Hz, it should be clear that fast fading effects have negligible effect on the performance of this robust signaling approach. In fact, the results on Figs. 5.15 through 5.17 are only weakly dependent on the value of γ, which contrasts sharply with the uncoded FSK and DPSK results on Figs. 5.10 and 5.11.

REFERENCES

5.1 P. A. Bello, "Characterization of Randomly Time-Variant Linear Channels," IEEE Trans. Commun. Syst., Vol. CS-11, pp. 360-393, December 1963.

5.2 R. W. Sutton, E. H. Schroeder, A. D. Thompson, and S. G. Wilson, "Satellite-Aircraft Multipath and Ranging Experiment Results at L-Band," IEEE Trans. on Comm., Vol. Com-21, No. 5, May 1973.

5.3 L. A. Frasco and H. D. Goldfein, "Signal Design for Aeronautical Channels," IEEE Trans. on Comm., Vol. Com-21, No. 5, May 1973.

5.4 J. J. Jones, "Multichannel FSK and DPSK Reception With Three-Component Multipath," IEEE Trans Comm. Tech., Vol. Com-16, pp. 808-821, December 1968.

5.5 G. D. Forney, "Burst-Correcting Codes for the Classic Bursty Channel," IEEE Trans. on Comm. Tech., Vol. Com-19, No. 5, October 1971.

5.6 D. Chase, "A Class of Algorithms for Decoding Block Codes With Channel Measurement Information," IEEE Trans. on Info. Theory, Vol. IT-18, January 1972.

5.7 D. Chase, "The Applications of Codem Concepts for Communications Over the Aeronautical Channel," presented at the International Telemetering Conference, October 1973, Washington, D.C.

5.8 D. Chase, "A Combined Coding and Modulation Approach for Communication Over Dispersive Channels," IEEE Trans. on Comm., March 1973, pp. 1591-74.

5.9 D. Chase, "Multiple Rate Codes and Adaptive Decoding," presented at the 1973 IEEE International Symposium on Info. Theory, Ashkelon, Israel.

5.10 J. M. Wozencraft and I. R. Jacobs, Principles of Communication Engineering, New York, Wiley, 1965.

5.11 W. W. Peterson and E. J. Weldon, Jr., Error-Correcting Codes, MIT Press, Cambridge, Mass., 1972.

Appendix A

CALCULATION OF THE SPECULAR POINT

This appendix determines the location of the specular point for a specified (specular point) grazing angle in an arbitrary communication link over the earth. Once the grazing angle is given, the central angle θ_s from one terminal to the specular point is computed using an interative algorithm. Then the central angle $\Delta\theta_A$ from the specular point to the second terminal is computed.

The specular point S lies along the plane through the terminals and the earth's center. This is designated by $\omega = \pi/2$ in Fig. 1. The ranges from the terminals to a point S on the surface at the angle θ are given by

$$r_1 = r_0 \sqrt{1 + p_1^2 - 2p_1 \cos \theta} \tag{1}$$

$$r_2 = r_0 \sqrt{1 + p_2^2 - 2p_2 \cos (\theta_A - \theta)} \tag{2}$$

where

$$p_1 = 1 + h_1/r_0 \tag{3}$$

$$p_2 = 1 + h_2/r_0 \tag{4}$$

and where r_0 is the radius of the earth, h_1 and h_2 are the heights of the terminals above the earth, and θ_A is the central (elevation)

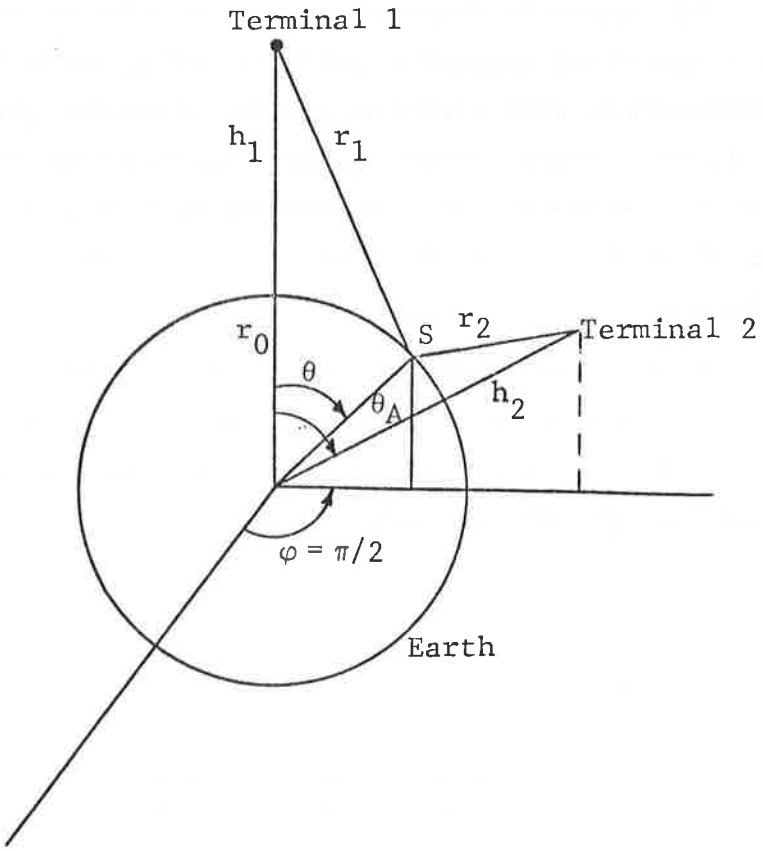

Figure A-1 Geometry of Specular Point

angle from one terminal to the other. The normalized parameters R_1, R_2, H_1, H_2 are defined by

$$R_1 = r_1/r_0 \tag{5}$$

$$R_2 = r_2/r_0 \tag{6}$$

$$H_1 = h_1/r_0 \tag{7}$$

$$H_2 = h_2/r_0 \tag{8}$$

The specular point is defined as that point for which the incidence grazing angle γ_1 equals the scattering grazing angle γ_2, i.e.,

$$\gamma_1 = \gamma_2 = \gamma \tag{9}$$

These two grazing angles are defined by

$$\sin \gamma_1 = (p_1 \cos \theta_s - 1)/R_{1s} \tag{10}$$

$$\sin \gamma_2 = [p_2 \cos (\theta_A - \theta_s) - 1]/R_{2s} \tag{11}$$

where R_{1s} and R_{2s} are the values of R_1 and R_2 when $\theta = \theta_s$, $\varphi = \pi/2$. When γ is specified, Eq. (10) indicates that θ_s can be computed as the root of

$$f_1(\theta_s) = p_1 \cos \theta_s - (1 + R_{1s} \sin \gamma) \tag{12}$$

Once θ_s is known, Eq. (11) indicates that $\Delta\theta_A = \theta_A - \theta_s$ can be computed as the root of

$$f_2(\Delta\theta_A) = p_2 \cos (\Delta\theta_A) - (1 + R_{2s} \sin \gamma) \tag{13}$$

Numerical Evaluation

The Fortran scientific subroutine "RTMI" solves general non-linear equations of the form $f(\theta) = 0$ by means of Mueller's iteration method. The calling sequence is

```
CALL RTMI(T,F,FCT,TMIN,TMAX,ERROR,IEND,IER)
```

where the arguments are specified as

T - resultant root of FCT(T) = 0
F - resultant function value of FCT at the root T
FCT - name of the external function subprogram to evaluate $f(\theta)$
TMIN - input value of initial lower bound on root T
TMAX - input value of initial upper bound on root T
ERROR - input value of upper bound of error in root T
IEND - maximum number of iteration steps specified
IER - resultant error flag coded as follows:
IER=0 - no error
IER=1 - no convergence after IEND iterations
IER=2 - FCT(TMIN)*FCT(TMAX) > 0

The only restriction on using the subroutine is that the product of the values of the function at the end points (TMIN and TMAX) be less than or equal to zero. Violation of this condition is indicated by IER=2.

The end points chosen for $f_1(\theta_s)$ are $\theta_s=0, \pi/2$. It is easily shown that the product of the values of the function at these points is less than zero, i.e.,

$$f_1(0) = H_1(1 - \sin\gamma) > 0$$

$$f_1(\pi/2) = -(1 + \sqrt{1 + p_1^2}\sin\gamma) < 0$$

and their product is less than zero

$$f_1(0)f_2(\pi/2) < 0$$

The end points chosen for $f_2(\Delta\theta_A)$ are $\Delta\theta_A = 0, \pi/2$. In this case

$$f_2(0) = H_2(1 - \sin\gamma) > 0$$

$$f_2(\pi/2) = -(1 + \sqrt{1 + p_2^2}\sin\gamma) < 0$$

and again their product is less than zero,

$$f_2(0)f_2(\pi/2) < 0$$

```
      SUBROUTINE SPECULAR(GRAZ)
      COMMON R0,SP,P1,P2
      COMMON/SPEC/TS,DTA,DS,R1S,R2S,R1S2,R2S2,SG
      EXTERNAL FCT1,FCT2
      SG=SIND(GRAZ)
C     COMPUTE TS WITH ERROR=1.E-6 (OUT OF ABOUT 1 RAD)
      ERROR=1.E-6
      CALL RTMI(TS,F1,FCT1,0.0,1.5707,ERROR,2000,IER)
      IF(IER.NE.0)TYPE 10,IER
10    FORMAT(1X,'IER=',I1,'   1=NO CNVRGNCE, 2=NO ROOT (TS)')
C
C     COMPUTE DTA WITH ERROR=1.E-8 (OUT OF ABOUT 1.E-3 RAD)
      ERROR=1.E-8
      CALL RTMI(DTA,F2,FCT2,0.0,1.5707,ERROR,3000,IER)
      IF(IER.NE.0)TYPE 12,IER
12    FORMAT(1X,'IER=',I1,'   1=NO CNVRGNCE, 2=NO ROOT (DTA)')
C
C     COMPUTE SPEC DELAY DS (W/R DIRECT PATH)
      RSA=SQRT(P1*P1+P2*P2-2.*P1*P2*COS(TS+DTA))
      DS=R0*(R1S+R2S-RSA)/SP
      END
C*****************************************************************
      FUNCTION FCT1(X)
      COMMON R0,SP,P1,P2
      COMMON/SPEC/TS,DTA,DS,R1S,R2S,R1S2,R2S2,SG
C
C     FCT1(X)=0 @ X FOR WHICH SIN(GRAZ)=SG
      CX=COS(X)
      R1S2=1.+P1*P1-2.*P1*CX
      R1S=SQRT(R1S2)
10    FCT1=P1*CX-(1.+R1S*SG)
      END
C*****************************************************************
      FUNCTION FCT2(Y)
      COMMON R0,SP,P1,P2
      COMMON/SPEC/TS,DTA,DS,R1S,R2S,R1S2,R2S2,SG
C
C     FCT2(Y)=0 @ Y FOR WHICH SIN(GRAZ)=SG
      CY=COS(Y)
      R2S2=1.+P2*P2-2.*P2*CY
      R2S=SQRT(R2S2)
10    FCT2=P2*CY-(1.+R2S*SG)
      END
```

Appendix B

CALCULATION OF THE θ-INTERVAL OF EACH DELAY CONTOUR

Along the $\varphi = \pi/2$ axis, the delay $\xi(\theta,\pi/2) \triangleq \xi(\theta)$ has a minimum at the specular point $\xi(\theta_s) = \xi_s$ as shown in Fig. 1. Let $\Delta\theta_1$ and $\Delta\theta_2$ be the θ-intervals at which $\xi - \xi_s = \Delta\xi$. Then $\Delta\theta_1$ and $\Delta\theta_2$ are the roots of $f(\Delta\theta) = 0$, where

$$f(\Delta\theta) = \xi(\theta_s + \Delta\theta) - \xi_s - \Delta\xi \tag{1}$$

An accurate evaluation of $f(\Delta\theta)$ can be made by considering the components of ξ and ξ_s, i.e.,

$$\xi = \frac{r_0}{c}\,[R_1(\Delta\theta) + R_2(\Delta\theta)] \tag{2}$$

$$\xi_s = \frac{r_0}{c}\,[R_1(0) + R_2(0)] = \frac{r_0}{c}\,[R_{1_s} + R_{2_s}] \tag{3}$$

where r_0 is the radius of the earth, c is the speed of light in vacuo, and the normalized slant ranges are given by

$$R_1 = \sqrt{1 + p_1^2 - 2p_2 \cos\,(\theta_s + \Delta\theta)} \tag{4}$$

$$R_2 = \sqrt{1 + p_2^2 - 2p_2 \cos\,(\Delta\theta_A + \Delta\theta)} \tag{5}$$

The central angle from specular point to the aircraft terminal is $\Delta\theta_A$ and p_1, p_2 are known in terms of the satellite, aircraft altitudes h_1, h_2, i.e.,

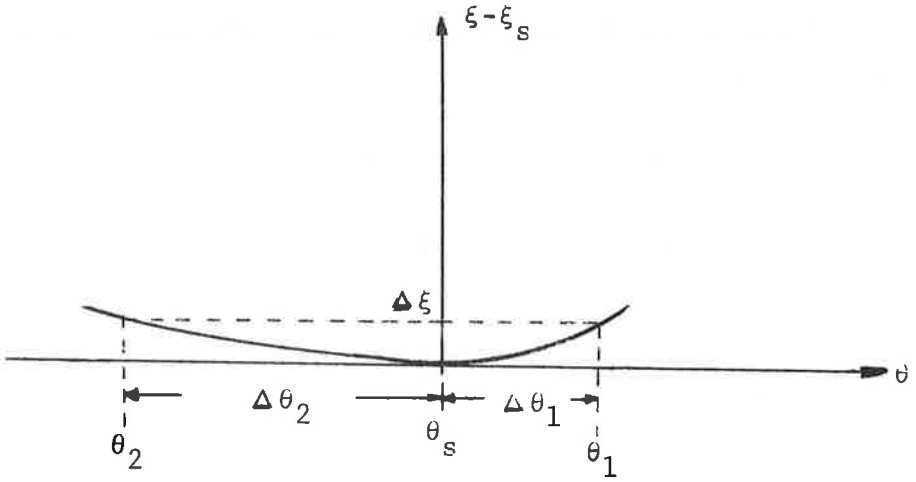

Figure B-1 Delay in the Vicinity of the Specular Point Along the $\varphi = \pi/2$ Plane

$$p_1 = 1 + h_1/r_0 \tag{6}$$

$$p_2 = 1 + h_2/r_0 \tag{7}$$

Substituting (2) - (7) into (1) gives

$$f(\Delta\theta) = \frac{R_0}{c} \left[R_{1_s} (\sqrt{1+x_1} - 1) + R_{2_s} (\sqrt{1+x_2} - 1)\right] \tag{8}$$

where

$$x_1 = 2p_1\delta/R_{1_s}^2 \tag{9}$$

$$\delta = \cos\theta_s - \cos(\theta_s + \Delta\theta) = 2\sin(\frac{\Delta\theta}{2})\sin(\theta_s + \frac{\Delta\theta}{2}) \tag{10}$$

$$x_2 = 2p_2\beta/R_{2_s}^2 \tag{11}$$

$$\beta = \cos\Delta\theta_A - \cos(\Delta\theta_A - \Delta\theta) = -2\sin(\frac{\Delta\theta}{2})\sin(\Delta\theta_A - \frac{\Delta\theta}{2}) \tag{12}$$

The evaluation of $\sqrt{1+x} - 1$ is made using the FUNCTION SUBPROGRAM EXPAND(X) (appended to this section), and the roots of $f(\Delta\theta)$ are found using the FORTRAN SCIENTIFIC SUBROUTINE RTMI (see Appendix A). The SUBROUTINE THETA which gives the values of $\Delta\theta_1$ and $\Delta\theta_2$ is appended to this section.

```
TYPE JTHETA
      SUBROUTINE THETA(DT1,DT2)
      COMMON P0,SP,P1,P2
      COMMON/CALC/DD
      COMMON/SPEC/TS,DTA,DS
      EXTERNAL DIFF
      ERROR=1.E-6
      CALL RTMI(DT1,D1,DIFF,0.,1.5707,ERROR,1000,IER)
      IF(IER.NE.0.0)TYPE 10,IER
10    FORMAT(1X,'IER=',I1,'   1=NO CNVERGNCE,2=NO ROOT(DT1)')
      TEND=-TS
      CALL RTMI(DT2,D2,DIFF,TEND,0.,ERROR,1000,IER)
      IF(IER.NE.0)TYPE 12,IER
12    FORMAT(1X,'IER=',I1,'   1=NO CNVRGNCE,2=NO ROOT(DT2)')
      END
C*****************************************************
      FUNCTION DIFF(DT)
      COMMON P0,SP,P1,P2
      COMMON/CALC/DD
      COMMON/SPEC/TS,DTA,DS,R1S,R2S,R1S2,R2S2,SG
      Y=0.5*DT
      SY=SIN(Y)
      DELTA=2.*SY*SIN(TS+Y)
      X=2.*P1*DELTA/R1S2
      R1DIFF=R1S*EXPAND(X)
      BETA=-2.*SY*SIN(DTA-Y)
      X=2.*P2*BETA/R2S2
      R2DIFF=R2S*EXPAND(X)
10    DIFF=(R1DIFF+R2DIFF)/SP-DD
      END
C*****************************************
      FUNCTION EXPAND(X)
C.....EXPAND(X)=SQRT(1+X)-1
      IF(ABS(X).GE.1.E-5) GO TO 300
      SUM=0.
      TERM=1.
      K=1
      P=X/2.
      DO 100 I=1,100
      TERM=-K*P*TERM/(I+1.)
      SUM=SUM+TERM
      RATIO=ABS(TERM/(1.+SUM))
      IF(RATIO.LT.1.E-12)GO TO 200
100   K=K+2
      TYPE 150
150   FORMAT(1X,'ACCURACY NOT REACHED IN EXPANSN')
200   EXPAND=P*(1.+SUM)
      RETURN
300   EXPAND=SQRT(1.+X)-1.
      END
```

Appendix C
EVALUATION OF THE POWER SPECTRAL DENSITY AT THE SPECULAR POINT

The area under the end regions is given by

$$I_1 = \frac{R_{TR}^2}{4\pi} \int_{\theta_1-\epsilon_1}^{\theta_1} \frac{G\sigma}{R_1^2 R_2^2} \sin\theta \frac{\partial\varphi}{\partial\xi} d\theta \tag{1}$$

and

$$I_2 = \frac{R_{TR}^2}{4\pi} \int_{\theta_2}^{\theta_2+\epsilon_2} \frac{G\sigma}{R_1^2 R_2^2} \sin\theta \frac{\partial\varphi}{\partial\xi} d\theta \tag{2}$$

where

$$\frac{\partial\varphi}{\partial\xi} = \frac{-c/r_0}{\frac{P_2}{R_2} \sin\theta_A \sin\theta \cos\omega} \tag{3}$$

Along the $\omega = \pi/2$ plane, the delay is given by

$$\xi_0 = \frac{r_0}{c} (R_{10} + R_{20}) \tag{4}$$

where

$$R_{10} = \sqrt{1 + p_1^2 - 2p_1 \cos\theta} \tag{5}$$

$$R_{20} = \sqrt{1 + p_2^2 - 2p_2 \cos(\theta_A-\theta)} \tag{6}$$

Moving away from the $\varphi = \pi/2$ plane along a contour of constant delay, such that

$$\theta = \theta_0 + \epsilon \tag{7}$$

and

$$\varphi = \pi/2 + \delta \tag{8}$$

then for $\epsilon, \delta \ll \pi/2$

$$R_1 = R_{10} + \left.\frac{\partial R_1}{\partial \theta}\right|_0 \epsilon \tag{9}$$

$$R_2 = R_{20} + \left.\frac{\partial R_2}{\partial \theta}\right|_0 \epsilon + \left.\frac{\partial^2 R_2}{\partial \varphi^2}\right|_0 \frac{\delta^2}{2} \tag{10}$$

(Note that $\partial R_1/\partial \varphi = \partial R_2/\partial \varphi = \partial^2 R_2/\partial\theta\partial\varphi = 0$).

Since we have moved in such a way that

$$\xi = \frac{r_0}{c}(R_1 + R_2) = \xi_0 \tag{11}$$

then by substituting (4), (9) and (10) into (11), we get

$$\delta = \sqrt{\frac{-2\left(\left.\frac{\partial R_1}{\partial \theta}\right|_0 + \left.\frac{\partial R_2}{\partial \theta}\right|_0\right)\epsilon}{\left.\frac{\partial^2 R_2}{\partial \theta^2}\right|_0}} \tag{12}$$

The derivatives in (12) are easily evaluated along the $\varphi = \pi/2$ plane as

$$\frac{\partial R_1}{\partial \theta} = \frac{P_1}{R_1} \sin \theta \tag{13}$$

$$\frac{\partial R_2}{\partial \theta} = \frac{-P_2}{R_2} \sin (\theta_A - \theta) \tag{14}$$

$$\frac{\partial^2 R_2}{\partial \varphi^2} = \frac{P_2}{R_2} \sin \theta_A \sin \theta_2 \tag{15}$$

Substituting (13) - (15) into (12) gives the φ increments ($\delta = \delta_1, \delta_2$) at each of the end points ($\theta = \theta_1, \theta_2$) in terms of the respective θ increments ($\epsilon = -\epsilon_1, \epsilon_2$) as

$$\delta_1 = \sqrt{2 \frac{\frac{P_1}{R_1} \sin \theta_1 - \frac{P_2}{R_2} \sin (\theta_A - \theta_1)}{\frac{P_2}{R_2} \sin \theta_A \sin \theta_1} \epsilon_1} \tag{16}$$

$$\delta_2 = \sqrt{2 \frac{\frac{P_2}{R_2} \sin (\theta_A - \theta_2) - \frac{P_2}{R_2} \sin \theta_1}{\frac{P_2}{R_2} \sin \theta_A \sin \theta_2} \epsilon_2} \tag{17}$$

Substituting (3) and (16) into (1) gives*

$$I_1 = \frac{R_{TR}^2}{4\pi} \frac{c}{r_0} \frac{G\sigma}{R_1^2 R_2^2} \frac{1}{\frac{P_2}{R_2} \sin\theta_A} \sqrt{\frac{\frac{P_2}{R_2} \sin\theta_A \sin\theta_1}{2[\frac{P_1}{R_1} \sin\theta_1 - \frac{P_2}{R_2} \sin(\theta_A - \theta_1)]}} \int_{\theta_1 - \epsilon_1}^{\theta_1} \frac{d\theta}{\sqrt{\epsilon}} \tag{18}$$

The change of variable $\theta = \theta_1 - \epsilon$, yields the final result

$$I_1 = \frac{R_{TR}^2}{4\pi} \frac{c}{r_0} \frac{G\sigma}{R_1^2 R_2^2} \sqrt{\frac{2\epsilon_1 \sin\theta_1}{[\frac{P_2}{R_2} \sin\theta_A][\frac{P_1}{R_1} \sin\theta_1 - \frac{P_2}{R_2} \sin(\theta_A - \theta_1)]}} \tag{19}$$

In a similar manner, the integration over the end interval at θ_2 yields

$$I_2 = \frac{R_{TR}^2}{4\pi} \frac{c}{r_0} \frac{G\sigma}{R_1^2 R_2^2} \sqrt{\frac{2\epsilon_2 \sin\theta_2}{[\frac{P_2}{R_2} \sin\theta_A][\frac{P_2}{R_2} \sin(\theta_A - \theta_2) - \frac{P_1}{R_1} \sin\theta_1]}} \tag{20}$$

*Note that ϵ is assumed to be chosen small enough such that the factor in front of the integral is essentially constant over the range of integration.

The evaluation of $Q_\xi(\xi)$ at the specular point can be accomplished by letting the end points approach the specular point, i.e.,

$$Q(\xi_S) = \lim_{\epsilon_1 \to 0} I_1 \Big|_{\theta_1=\theta_S+\epsilon_1} \lim_{\epsilon_2 \to 0} I_2 \Big|_{\theta_2=\theta_S-\epsilon_2} \tag{21}$$

Let

$$\theta_1 = \theta_S + \epsilon_1 \tag{22}$$

and substitute (22) into (C.19) giving

$$I_1 = \frac{R_{TR}^2}{4\pi} \frac{c}{r_0} \frac{G\sigma}{R_1^2 R_2^2} \sqrt{\frac{2\epsilon_1 \sin(\theta_S+\epsilon_1)}{(\frac{P_2}{R_2} \sin\theta_A)[\frac{P_1}{R_1} \sin(\theta_S+\epsilon_1) - \frac{P_2}{R_2} \sin(\theta_A-\theta_S-\epsilon_1)]}} \tag{23}$$

Expanding the sin's of the multiple angles, under the assumption that $\epsilon \ll \pi/2$, gives

$$I_1 = \frac{R_{TR}^2}{4\pi} \frac{c}{r_0} \frac{G\sigma}{R_1^2 R_2^2}$$

$$\sqrt{\frac{2\epsilon_1 \sin\theta_S \cos\epsilon_1}{(\frac{P_2}{R_2}\sin\theta_A)\{[\frac{P_1}{R_1}\sin\theta_S - \frac{P_2}{R_2}\sin(\theta_A-\theta_S)]\cos\epsilon_1 + [\frac{P_1}{R_1}\cos\theta_S + \frac{P_2}{R_2}\cos(\theta_A-\theta_S)]\sin\epsilon_1\}}} \tag{24}$$

The factors $\frac{1}{R_1}$ and $\frac{1}{R_2}$ can be expanded about the specular point to give

$$\frac{1}{R_1} = \frac{1}{R_{1_S}} - (\frac{P_1}{R_{1_S}^3}\sin\theta_S)\epsilon_1 \tag{25}$$

$$\frac{1}{R_2}' = \frac{1}{R_{2_S}} + [\frac{P_2}{R_{2_S}^3}\sin(\theta_A-\theta_S)]\epsilon_1 \tag{26}$$

Substituting (25) and (26) into (24) gives

$$I_1 = \frac{R_{TR}^2}{4\pi} \frac{c}{r_0} \frac{G\sigma}{R_1^2 R_2^2} \sqrt{\frac{2\epsilon_1 \sin\theta_S \cos\epsilon_1}{A_1(A_2 \sin\epsilon_1 - A_3 \sin\epsilon_1 \cos\epsilon_1)}} \tag{27}$$

where

$$A_1 = \frac{P_2}{R_2}\sin\theta_A \tag{28}$$

$$A_2 = \frac{P_1}{R_1}\cos\theta_S + \frac{P_2}{R_2}\cos(\theta_A-\theta_S) \tag{29}$$

$$A_3 = \frac{P_1^2}{R_1^3} \sin^2\theta_S + \frac{P_2^2}{R_2^3} \sin^2(\theta_A - \theta_S) \tag{30}$$

Note that in the evaluation of (27), use has been made of the fact that at the specular point

$$\frac{\partial R_1}{\partial \theta} + \frac{\partial R_2}{\partial \theta} = 0 = \frac{P_1}{R_{1_S}} \sin\theta_S - \frac{P_2}{R_{2_S}} \sin(\theta_A - \theta_S) \tag{31}$$

The limit of (27) as $\epsilon_1 \to 0$ can then be determined as

$$\lim_{\epsilon_1 \to 0} I_1 \Big|_{\theta_1 = \theta_S + \epsilon} = \frac{R_{TR}^2}{4\pi} \frac{c}{r_0} \frac{G\sigma}{R_{1_S}^2 R_{2_S}^2} \sqrt{\frac{2 \sin\theta_S}{A_1(A_2 - A_3)}} \tag{32}$$

In a similar manner, the limiting value of I_2 can be shown to be the same value, i.e.,

$$\lim_{\epsilon_2 \to 0} I_2 \Big|_{\theta_2 = \theta_S - \epsilon_2} = \lim_{\epsilon_1 \to 0} I_1 \Big|_{\theta_1 = \theta_S + \epsilon_1} \tag{33}$$

Therefore the value of the delay psd at $\xi = \xi_S$ is

$$P(\xi_S) = \frac{R_{TR}^2}{4\pi} \frac{c}{r_0} \frac{2G\sigma}{R_{1_S}^2 R_{2_S}^2} \sqrt{\frac{2 \sin\theta_S}{A_1(A_2 - A_3)}} \tag{34}$$

Appendix D

PROJECTION OF AN OCEAN SURFACE POINT ONTO A UNIT SPHERE AT THE AIRCRAFT

The unit vectors at the aircraft in the spherical coordinate directions are $\hat{u}_r^A$, $\hat{u}_\theta^A$, $\hat{u}_\varphi^A$. The aircraft is assumed to be heading in the x'-direction at an angle α to the $\hat{u}_\varphi$ direction* as shown in Fig. 1. Note the aircraft is assumed to be in level flight in the x'y'-plane (or equivalently the plane formed by $\hat{u}_\theta$ and $\hat{u}_\varphi$). The unit vectors in the x' and y' directions can then be written as

$$\hat{u}_{x'} = \cos\alpha\,\hat{u}_\varphi^A + \sin\alpha\,\hat{u}_\theta^A \tag{1}$$

$$\hat{u}_{y'} = \sin\alpha\,\hat{u}_\varphi^A - \cos\alpha\,\hat{u}_\theta^A \tag{2}$$

The unit vector $\hat{\beta}$ is directed from the scattering point to the aircraft. The angles θ_B and φ_B measure the elevation and azimuth angles of $-\hat{\beta}$ in the primed (i.e., aircraft) coordinate system. From basic considerations

$$\cos\theta_B = -\hat{\beta}\cdot\hat{u}_r^A = -\beta_r^A \tag{3}$$

$$\cos\varphi_\beta = \hat{u}_{x'}\cdot[-\hat{\beta} + (\hat{\beta}\cdot\hat{u}_r^A)\hat{u}_r^A]/\sin\theta_B \tag{4}$$

*$\hat{u}_\varphi$ is perpendicular to the specular point plane of incidence.

Using the relationships [2.1], [2.2]

$$\beta_r^A = [(1+H_2) - (\sin\theta_A \sin\theta \sin\varphi - \sin\theta_A \cos\theta)]/R_2 \tag{5}$$

$$\beta_\theta^A = -(\cos\theta_A \sin\theta \sin\varphi - \sin\theta_A \cos\theta)/R_2 \tag{6}$$

$$\beta_\varphi^A = \sin\theta \cos\varphi/R_2 \tag{7}$$

and Eqs. (1) and (2), gives

$$\cos\theta_B = -[(1+H_2) - \sin\theta_A \sin\theta \sin\varphi - \sin\theta_A \cos\theta)]/R_2 \tag{8}$$

$$\cos\varphi_B = [\sin\alpha (\cos\theta_A \sin\theta \sin\varphi - \sin\theta_A \cos\theta) - \cos\alpha \sin\theta \cos\varphi]/R_2 \sin\theta_B \tag{9}$$

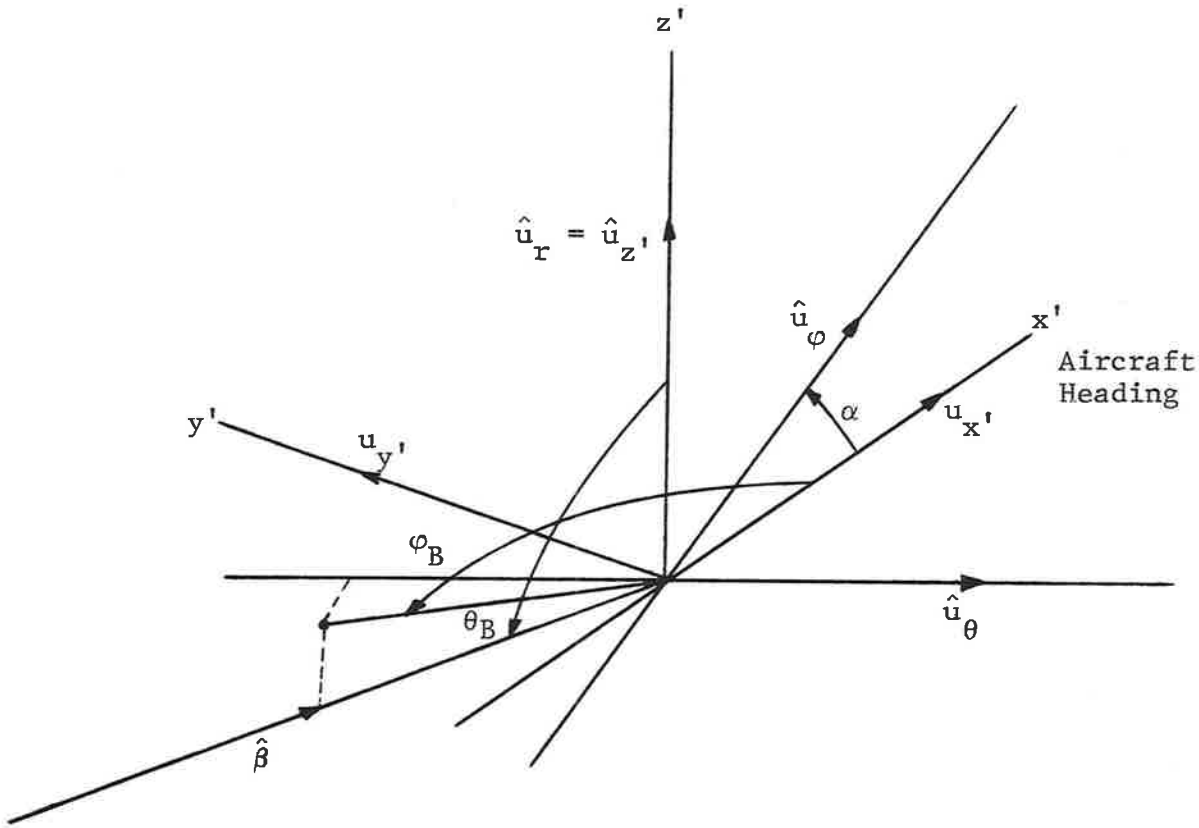

Figure D-1 Aircraft Coordinate System

Appendix E
RADIUS OF CURVATURE OF A SPECTRAL COMPONENT

This appendix computes the radius of curvature of a sinusoidal component of a wave train. This component is specified by

$$z(k,x) = H \sin kx \tag{1}$$

where H is the wave amplitude, k is the wavenumber, and x is a spatial coordinate. A differential element $d\sigma$ along the surface of the wave has a tangent t, as shown in Fig. 1, which is given by

$$\hat{t} = \cos\theta\ \hat{a}_x + \sin\theta\ \hat{a}_z \tag{2}$$

where θ is the angle $\hat{t}$ makes with the x-axis. Note that

$$\tan\theta = \frac{\partial z}{\partial x} = kH \cos kx \tag{3}$$

The radius of curvature ρ is specified by

$$\frac{1}{\rho} = \left|\frac{d\hat{t}}{d\sigma}\right| \tag{4}$$

However,

$$\left|\frac{d\hat{t}}{d\sigma}\right| = \left|\frac{\partial\hat{t}}{\partial\theta}\right| \frac{\partial\theta}{\partial x}\frac{\partial x}{\partial\sigma} \tag{5}$$

From (2)

$$\left|\frac{d\hat{t}}{\partial\theta}\right| = 1\ , \tag{6}$$

From (3)

$$\frac{\partial\theta}{\partial x} = k^2 H \sin kx \cos^2\theta\ , \tag{7}$$

and from inspection of Fig. 1 and Eq. (3)

$$\frac{\partial x}{\partial \sigma} = \cos\,\theta = 1/\sqrt{1 + (kH\,\cos\,kx)^2} \tag{8}$$

Substituting (5) through (8) into (4) gives the radius of curvature as

$$\rho = \frac{(1 + k^2H^2\,\cos^2 kx)^{3/2}}{k^2H\,\sin\,kx} \tag{9}$$

Note that the minimum value of this local radius of curvature occurs at $x = \pi/2k + n\pi/k$, $n = 0,1, \ldots$

$$\rho_{min} = \frac{1}{k^2H} \tag{10}$$

The wavenumber k is known in terms of the wavelength L

$$k = 2\pi/L, \tag{11}$$

and the rms height of the wave is given by

$$\sigma = \frac{H}{\sqrt{2}} \tag{12}$$

Thus, ρ_{min} can alternatively be expressed as

$$\rho_{min} = \frac{L^2}{(2\pi)^2H} = \frac{1}{k^2\sigma\sqrt{2}} \tag{13}$$

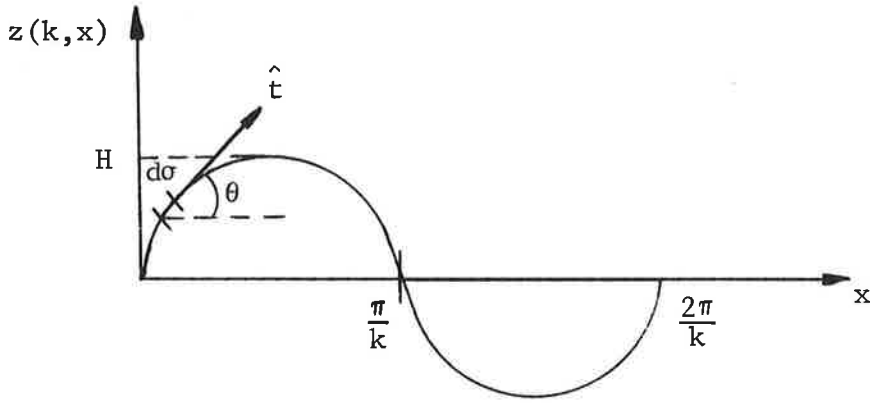

Figure E-1 Wave Component

Appendix F

CROSS-PLANE DOPPLER POWER SPECTRAL DENSITIES

Table F-1

DOPPLER POWER SPECTRAL DENSITY

GRAZING ANGLE = 10^{o}, AIRCRAFT HEIGHT = 10 Km, RMS SEA SLOPE = .2

Normalized Doppler ν/ν_{max}	Normalized Doppler Power Spectral Density $P(\nu)/P(0)$			
	Horizontal	Vertical	Same-Sense Circular	Opposite-Sense Circular
0.0000	1.00	1.00	1.00	1.00
0.0205	.943	.961	.964	.938
0.0409	.796	.855	.863	.770
0.0614	.613	.707	.724	.558
0.0818	.443	.570	.579	.371
0.1023	.311	.444	.448	.236
0.1227	.217	.340	.340	.152
0.1432	.152	.257	.256	.101
0.1636	.107	.192	.192	.0729
0.1841	.0750	.139	.142	.0553
0.2095	.0521	.0987	.104	.0439
0.2250	.0358	.0689	.0754	.0354
0.2455	.0241	.0468	.0537	.0289
0.2659	.0159	.0309	.0375	.0234
0.2864	.0102	.0196	.0256	.0189
0.3068	.00645	.0123	.0173	.0251
0.3273		.00722	.0113	.0118
0.3477		.00414	.00729	.00894
0.3682		.00223		
0.3886				
0.4091				
$P(0)/P_{direct}$	4.9 dB	-1.5 dB	1.9 dB	-4.6 dB
P_{total}/P_{direct}	-2.7 dB	-8.3 dB	-4.7 dB	-12.5 dB

Table F-2

DOPPLER POWER SPECTRAL DENSITY

GRAZING ANGLE = 20^{o}, AIRCRAFT HEIGHT = 10 Km, RMS SEA SLOPE = .2

Normalized Doppler ν/ν_{max}	Normalized Doppler Power Spectral Density $P(\nu)/P(0)$			
	Horizontal	Vertical	Same-Sense Circular	Opposite-Sense Circular
0.0000	1.00	1.00	1.00	1.00
0.0208	.979	.981	.986	1.00
0.0417	.919	.924	.942	.995
0.0625	.827	.831	.869	.895
0.0833	.717	.278	.782	.823
0.1042	.600	.615	.684	.720
0.1250	.488	.506	.583	.638
0.1458	.386	.407	.486	.551
0.1667	.300	.322	.397	.476
0.1875	.229	.250	.318	.415
0.2083	.173	.192	.252	.363
0.2292	.128	.145	.196	.327
0.2500	.0946	.108	.151	.289
0.2708	.0688	.0787	.115	.254
0.2917	.0494	.0566	.0865	.225
0.3125	.0347	.0392	.0639	.195
0.3333	.0240	.0270	.0468	.169
0.3542	.0163	.0180	.0337	.144
0.3750	.0107	.0115	.0238	.120
0.3958	.00684	.00711	.0165	.975
0.4167	.00422	.00421	.0112	.0780
0.4375	.00251	.00238	.00748	.0606
0.4583	.00143	.00126	.00486	.0457
0.4792	.000774	.000617	.00310	.0337
$P(0)/P_{direct}$	4.8 dB	1.3 dB	3.2 dB	-9.5 dB
P_{total}/P_{direct}	-0.8 dB	-4.2 dB	-2.5 dB	-13.6 dB

Table F-3

DOPPLER POWER SPECTRAL DENSITY

GRAZING ANGLE = 30^{o}, AIRCRAFT HEIGHT = 10 Km, RMS SEA SLOPE = .2

Normalized Doppler ν/ν_{max}	$P(\nu)/P(0)$	
	Horizontal	Vertical
0.00	1.0	1.00
0.02	.990	.992
0.04	.961	.963
0.06	.915	.883
0.08	.855	.834
0.10	.784	.763
0.12	.706	.668
0.14	.624	.583
0.16	.544	.509
0.18	.466	.434
0.20	.393	.364
0.22	.327	.301
0.24	.268	.247
0.26	.217	.199
0.28	.173	.158
0.30	.136	.123
0.32	.106	.0952
0.34	.0812	.0715
0.36	.0612	.0535
0.38	.0454	.0390
0.40	.0330	.0279
0.42	.0236	.0195
0.44	.0164	.0133
0.46	.0112	.00873
0.48	.00740	.00555
$P(0)/P_{direct}$	4.3 dB	2.5 dB
P_{total}/P_{direct}	-0.1 dB	-2.0 dB

Normalized Doppler ν/ν_{max}	Same-Sense Circular
0.0000	1.00
0.0206	.994
0.0412	.975
0.0618	.928
0.0824	.885
0.1029	.832
0.1235	.743
0.1441	.668
0.1647	.594
0.1853	.521
0.2059	.450
0.2265	.383
0.2471	.323
0.2676	.268
0.2882	.220
0.3088	.178
0.3294	.143
0.3500	.113
0.3706	.0878
0.3912	.0676
0.4118	.0513
0.4324	.0385
0.4529	.0285
0.4735	.0210
0.4941	.0148
0.5147	.0104
0.5353	.00722
0.5559	.00490
$P(0)/P_{direct}$	3.4 dB
P_{total}/P_{direct}	-1.8 dB

APPENDIX G
REPORT OF INVENTIONS

A diligent review of the work performed under this contract has revealed no new innovation, discovery, improvement, or invention.